Ultrashort and Ultrahigh-Repetition-Rate Pulses from Passively Mode-Locked Semiconductor Lasers

Thesis by
Randal A. Salvatore

In Partial Fulfillment of the Requirements
for the Degree of
Doctor of Philosophy

California Institute of Technology
Pasadena, California

1996

(Defended Sept. 7, 1995)

Acknowledgments

First and foremost, I would like to acknowledge Professor Amnon Yariv for giving me the opportunity to study in his group. Not only will I thank him for the freedom to pursue directions which I've personally found exciting and for the chance to be "turned loose" in an extremely well-equipped laboratory but also for the opportunity of discussions with and guidance from him. I still recall that first day I began my project as Dr. Yariv said, "...they're two sharp fellows. You'll have to work hard to keep up with them." I soon found this to be undeniably true as I came to know Thomas Schrans and Steve Sanders. I'd like to thank Steve for his help in the early days and for his inspiring thesis. Of course, Thomas deserves a huge amount of thanks for the training, the in-depth discussions, the long days in the lab, and all the indispensable information which he has provided me with.

I'd like to thank most of the current and previous members of the group who I have had valuable interactions with, namely, Dr. Danny Eliyahu, Dr. John Kitching, Yuanjian Xu, John O'Brien, Dr. Tony Kewitsch, Dr. Ali Shakouri, Dr. John Iannelli, Dr. Gilad Almogy, Dr. Joseph Rosen, Bill Marshall, Dr. Lars Eng, Sergei Orlov, Doruk Engin, Jing Feng, Richard Boyd, Matt McAdams, Dan Provenzano, Dr. Bin Zhao, Boaz Salik, and Xiao-lin Tong. Additionally, I'd like to thank the Caltech staff members who have made things run much more smoothly: Jana Mercado, Ali Ghaffari, and Kevin Cooper. I owe thanks to Dr. T. R. Chen and his wife for providing me with some of the best regrown lasers one could ask for. Also, I'd like to thank Professor Axel Scherer for discussions and dielectric coatings. I remain grateful to Caltech for providing me with financial assistance.

Certainly, I will thank Mike DeLisio for discussions and for being the ideal roomate for most of my years at Caltech. Special thanks go to my parents, my brother, and my sister for encouragement and always being there in times of need. Finally, I'd like to thank Linda Wang for her unwavering support and for the fun times we have shared in the past, in the present, and likely in the future.

Abstract

This thesis is an investigation into both the fundamental and experimental aspects of using semiconductor lasers to generate extremely short (100's of fs) and very high repetition frequency (> 50 GHz) optical pulses. The pulses are produced through modelocking, a technique of forcing a laser to operate in a number of optical modes simultaneously and to hold a constant phase relationship between these modes. Both the shortest and highest repetition rate pulses have been obtained from passive mode-locking, an inherently nonlinear technique which does not use any active external timing source. Two structures, ridge-waveguide stripe lasers and liquid phase epitaxy (LPE) regrown lasers, were used to directly generate picosecond width pulses. Using cross-correlation techniques, pulse shape and phase measurements are made. Linear dispersion compensation is shown to achieve nearly a factor of 20 in pulse compression. Stable pulses down to 260 fs are generated.

Showing that exitonic effects are not essential in these devices, wavelength tunability was combined with dispersion compensation to create the first broadly tunable subpicosecond semiconductor source. The device is found to give tunability ranges and mode-locked spectral widths that are comparable to the best results achieved in dye lasers in terms of fractions of the operating gain spectral width. Results for different regimes in the tuning range are examined, and pulses directly from the laser are found to have about a 2 to 1 fall-time to rise-time ratio. A significant nonlinear chirp is found only when the laser is tuned to the short wavelength side of its tuning range and was determined to cause long tails in the autocorrelations of compressed pulses. Additionally, spread-resistant pulses are described and experimentally analyzed.

The case of high-repetition-rate modelocking, which more likely involves about 5 modes instead of 5000 modes, is examined. Approximations in the leading theory of passive modelocking are shown to be inadequate in this case. A steady-state model for high-repetition-rate modelocking is developed including phase effects and is tailored to parameters of semiconductor lasers. Self-consistent solutions show that a lower threshold gain can exist for a supermode than for single mode operation. Predictions of the laser's behavior upon modifying key material, geometric, and bias parameters are made. Experimental results show that through adjustment of the gain current, "chirp-controlled" modelocking is obtained with operation in any of the three chirp regimes (up-chirped, chirp-free, or down-chirped). This pulse chirp and resulting broadening are due to the algebraic addition of opposite-signed chirps from saturation of the absorber and gain sections. Theoretical modelling from the supermode analysis also traverses the same chirp regimes when the photon intensity is increased.

Contents

List of Figures

List of Tables

Chapter 1

Introduction

1.1 Short optical pulse generation

Not only is light typically the predominant means through which man has gathered information throughout his existence, but it is also becoming the preferred means of transmitting information in society today. The heart of this thesis is concerned with practical sources of ultrashort optical pulses and in extending our understanding of these. Over the past 35 years, huge strides of progress have been made in the vital components of optical communications: lasers and optical fiber. Lasers have made it possible to obtain intense beams of coherent light which are easily focused, while optical fibers have provided an effective means of guiding light over long distances with minimal loss. As coherent light sources, lasers have been able to produce extremely narrow fractional spectral widths. To impress information onto a signal, however, one must allow some finite bandwidth to exist. In terms of efficient return-to-zero

(RZ) transmission, the best one can do is to generate time-bandwidth-limited signals such that the time-bandwidth limit, $\tau_w \Delta\nu$, is satisfied. Most optical sources such as common light bulbs or light emitting diodes cannot attain this limit since they produce a broad, incoherent spectrum.

Perhaps the most amazing demonstration of coherence in lasers occurs in the mode-locked laser. A mode-locked laser is one in which a number of modes ($\geq$ 3) oscillate simultaneously and keep a fixed phase relationship between themselves. Thus, if all modes are equally spaced (Δf) in frequency and all have the same phase at some moment, one can easily see from Fourier series concepts that the net electric field of the separate oscillating modes will nearly cancel over the full period ($\tau = 1/\Delta f$) except near the moment when they all add up in phase to produce a large peak in electric field strength. Through this coherent interference between simultaneously operating modes of a single laser cavity is exactly how the shortest stable optical pulses have been obtained [1]. Furthermore, the beauty of a mode-locked source is that it is fully coherent over its whole spectrum and can therefore be used to generate ultrashort time-bandwidth-limited pulses.

Not only are sources of ultrashort pulses useful in optical communications but in a number of other applications as well. Mode-locked dye lasers have been used to generate pulses so short that they contain only three optical cycles (6 fs). Although capable of generating high powers ($>$ 1 kW), these lasers are large, expensive, complicated, and inefficient. They require many components (e.g. a dye circulation system, a high power pump laser, cooling systems, a number of mirrors, etc.) More compact systems involving Ti:sapphire, Nd:YAG, Nd:glass, etc. [2] lasers have been developed to produce ultrashort pulses, however they still maintain some of these disadvantages. To date, the most compact, efficient, and affordable lasers are the semiconductor lasers. Not surprisingly, of all types of lasers in use, semiconductor lasers are also the most numerous. The first ultrashort pulses produced by semiconductor lasers and compressed to subpicosecond widths were generated through passive modelocking by Yaron Silberberg at Bellcore in 1985 [3].

Today, clean pulses of < 300 fs are commonly generated by mode-locked semiconductor lasers [4]-[8]. These optical pulses are shorter than any pulses that have been produced with electronics to date. An external cavity allows relatively large energy pulses to be obtained along with lower pulse repetition rates and produces up to a 2 THz spectral bandwidth. These may likely be useful someday as broad coherent spectrum sources for wavelength division multiplexing (WDM).

Just last year, 1994, the first commercial mode-locked semiconductor laser product was announced. The laser generates subpicosecond pulses of up to 200 W peak power at an optical wavelength of 840 nm. Similar products at 1.3 μm and 1.55 μm are planned for the near future [9]. Although the laser may be useful as a source or as a development tool in communications, marketing of the laser so far has been mainly directed toward replacement of more complex sources currently used in spectroscopy.

1.2 Ultrahigh-repetition-rate modelocking

Because the mode separation and thus the pulse repetition rate is determined by the laser cavity length, shorter cavities can be used to generate mode-locked pulse trains at higher repetition rates. Due to its large material gain, short absorber and gain recovery times, and ability to be made into short cavities, the semiconductor laser is likely to be superior to all other lasers in producing stable trains of ultrahigh repetition rate mode-locked pulses. In fact, in 1989 it was demonstrated that modelocking could be achieved without the use of any external cavity, and repetition rates near 100 GHz were obtained [10]. This was independently discovered at Caltech by Steve Sanders et al. and published in 1990 [11].

From records gathered from the literature, a graph of reports of the highest repetition rate laser pulses is plotted in Fig. 1.1. Modelocking was first achieved by Hargrove at AT&T Bell Labs in 1964 [12]. This was demonstrated through active modelocking of a Helium Neon laser at 56 MHz and is displayed as the leftmost point in the figure. Most recently, a record modelocking repetition rate at 1.54 THz was reported by Arahira in 1994 with an InGaAsP (at 1.55 μm) laser and Bragg reflector structure used to reduce the likelihood of low harmonics of the repetition rate to modelock [13]. The fact that no external cavity is necessary at high repetition rates makes the source more compact. The graph shows that, nowadays, practically any desired repetition rate can be achieved with mode-locked semiconductor lasers.

Currently, there is much interest in using these monolithic semiconductor lasers

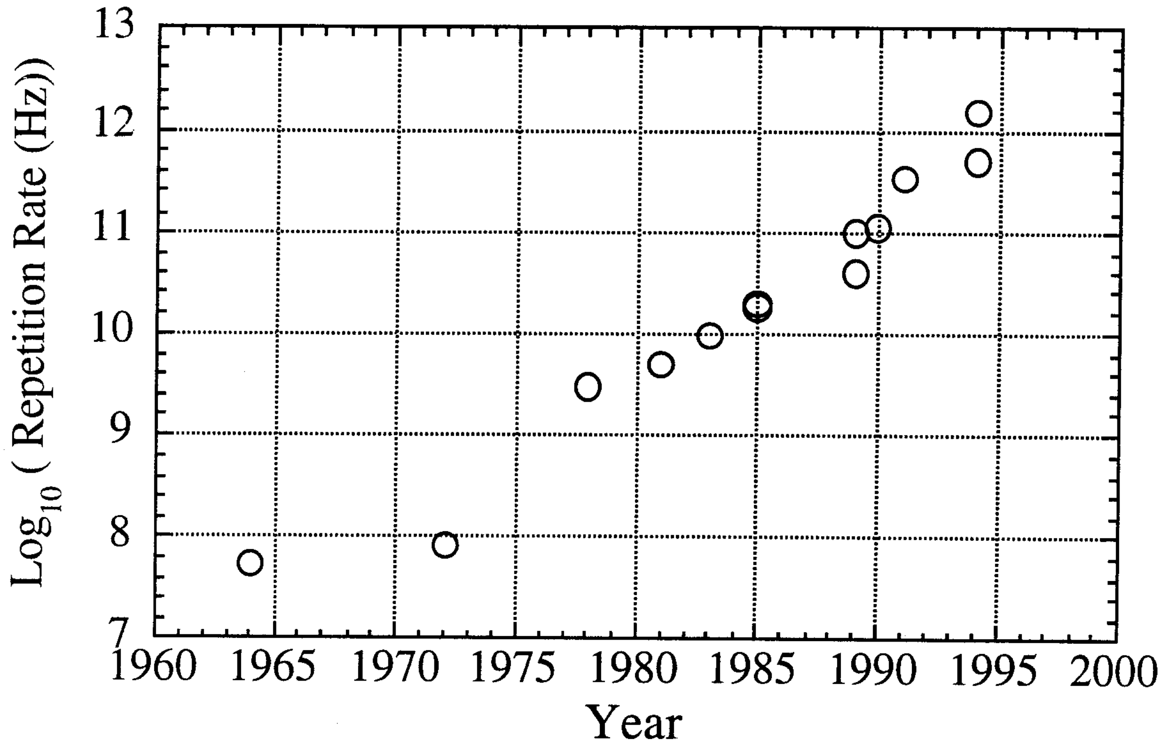

Figure 1.1: Reports of the highest repetition rates from modelocking throughout its history. Progress has proceeded at essentially an exponential rate with a doubling time of about two years.

as sources in optical communications. Relatively long monolithic lasers ($\sim$ 5 mm) are being developed as sources of return-to-zero (RZ) optical pulses which can subsequently be modulated with an external modulator or with an integrated electro-optic modulator [14,15] to obtain modulated pulse trains suitable for soliton transmission. Higher repetition rate mode-locked lasers are also under investigation as sources in very high bit rate time division multiplexing (TDM) systems at 40-100 GHz [16,17] and as stable sources of equally spaced phase locked channels of carriers for WDM systems [18,19] as an alternative to arrays of lasers or frequency modulation (FM) locked laser diodes, respectively. The mode-locked spectrum can serve as an extremely stable source of an equally spaced set of modes and may possess a stronger bistability and thus operate as a more stable source, with better wavelength stability than Fabry-Perot lasers used in some applications today [19]. It is likely that the world will see more from the mode-locked semiconductor laser in the near future.

1.3 Thesis outline

Since two vastly different regimes of operation are discussed, the subject matter divides rather naturally into two separate areas. The first covers external cavity mode-locked lasers, which produce relatively low-repetition-rate pulse trains having relatively large pulse energies, while the second applies mainly to short cavity, high-repetition-rate mode-locked semiconductor lasers. Each of these separate areas can be divided slightly less distinctly into experimental work and theoretical work. The unfolding accomplishments have progressed somewhat unequally in these four areas. Extensive development of a model of passive modelocking has previously led to a closed-form theoretical description of passive modelocking in the case of relatively low repetition rate lasers. Also experimental work in high-repetition rate lasers has had the predominantly unexpected success of modelocking at rates even beyond 1.5 THz. In contrast, experimental results from external cavity modelocking have not yet reached expectations. Arguments have been made that passively mode-locked semiconductor lasers should be able to generate pulse widths of 50 fs. This has not yet been attained. Likewise, no comparably complete theoretical model of high-repetition-rate passive modelocking has existed. If one wants to discover the most possible in a field, one should "strike" into the areas of greatest "darkness." For this reason, most of the efforts in this thesis have been directed toward the experimental aspects of external cavity lasers and the theoretical explanation of high-repetition-rate lasers.

Chapter 1 gives an introduction to short optical pulse generation in its first half and high-repetition-rate pulse trains in the second half. Chapter 2 delves more deeply into the field of short optical pulse generation and eventually concentrates toward passive modelocking and the dominant theoretical view today. The experimental setups used for passively mode-locked lasers are first presented in chapter 3, and important information about ultrafast pulse measurement and dispersion concepts follow. This leads to the topic of pulse compression. Tunability of mode-locked devices is also discussed in chapter 3 along with the prospects and results of combining tunability and pulse compression to obtain broadly wavelength tunable subpicosecond pulses. Chapter 3 ends by analyzing the limits of the mode-locked spectral width and tunability range and comparing these results to those from the most extensively developed mode-locked laser, the dye laser.

Determining the width, shape, and chirp of the mode-locked semiconductor laser is of utmost importance for understanding its operation, and these methods and results are presented in chapter 4. The next chapter, chapter 5, uses a similar setup but with a mask placed in the Fourier plane of the pulse compression system and utilizes the measured pulses for an application of generating dispersion-resistant pulses. These pulses are shown to spread out less rapidly than common pulses as they propagate through dispersive media.

Chapter 6 begins with a distinctly different regime of passively mode-locked laser operation. It concentrates on developing a complete self-consistent model for high-repetition-rate passively mode-locked lasers. Solutions for an approximate 3-mode model and a many-mode model of high-repetition-rate passively modelocking, which may even be extended to external cavity passive modelocking, are presented. The majority of the theory is given in this chapter. Chapter 7 begins with the experimental aspect of high-repetition-rate passive modelocking and describes agreement with the theoretical results of the previous chapter.

References

[1] R. L. Fork, C. H. B. Cruz, P. C. Becker, and C. V. Shank, *Opt. Lett.*, **12**, 483 (1987).

[2] E. P. Ippen, *Appl. Phys. B*, **58**, 159 (1994).

[3] Y. Silberberg and P. W. Smith, *IEEE J. Quantum Electron.*, **22**, 759 (1986).

[4] P. J. Delfyett, L. Florez, N. Stoffel, T. Gmitter, N. Andreadakis, G. Alphonse, and W. Ceislik, *Opt. Lett.*, **17**, 670 (1992).

[5] N. Stelmakh and J. M. Lourtioz, *Electron. Lett.*, **29**, 160 (1993).

[6] W. B. Jiang, M. Shimizu, R. P. Mirin, T. E. Reynolds, and J. E. Bowers, *Opt. Lett.*, **18**, 1937 (1993).

[7] J. Yu, M. Schell, M. Schulze, and D. Bimberg, *Appl. Phys. Lett.*, **65**, 2395 (1994).

[8] R. A. Salvatore, T. Schrans, and A. Yariv, *IEEE Photon. Technol. Lett.*, **5**, 756 (1993).

[9] D. Nelson at Laser Ionics, personal communication.

[10] P. P. Vasil'ev and A. B. Sergeev, *Electron. Lett.*, **25**, 1049 (1989).

[11] S. Sanders, L. Eng, J. Paslaski, and A. Yariv, *Appl. Phys. Lett.*, **56**, 310 (1990).

[12] L. W. Hargrove, R. L. Fork, and M. A. Pollack, *Appl. Phys. Lett.*, **5**, 4 (1964).

[13] S. Arahira, S. Oshiba, Y. Matsui, T. Kunii, and Y. Ogawa, *Opt. Lett.*, **19**, 834 (1994).

[14] P. B. Hanson, G. Raybon, U. Koren, B. I. Miller, and M. G. Young, *J. Lightwave Technol.*, **13**, 297 (1995).

[15] R. J. Helkey, W. X. Zou, A. Mar, D. B. Young, and J. E. Bowers, *Microwave Opt.*, **9**, 115 (1995).

[16] P. Blixt and J. E. Bowers, *IEEE Photon. Technol. Lett.*, **7**, 123 (1995).

[17] E. A. Swanson, S. R. Chinn, K. Hall, K. A. Rauschenbach, R. S. Bondurant, and J. W. Miller, *IEEE Photon. Technol. Lett.*, **6**, 1194 (1994).

[18] Y. K. Chen, M. C. Wu, T. Tanbun-Ek, R. A. Logan, and M. A. Chin, *IEEE Photon. Technol. Lett.*, **3**, 971 (1991).

[19] S. B. Alexander, R. S. Bondurant, D. Byrne, V. W. S. Chan, S. G. Finn, R. Gallager, B. S. Glance, H. A. Haus, P. Humblet, et al., *J. Lightwave Technol.*, **11**, 714 (1993).

Chapter 2

Review of methods of modelocking and other forms of short pulse generation

There are a number of methods which have been used to generate short optical pulses. The main techniques include gain switching, Q-switching, and mode-locking. Each of these is realizable in semiconductor lasers.

2.1 Gain switching

Gain switching is a technique by which one suddenly increases the pumping of a laser to increase its gain. Through this method, the number of photons generated by a laser can be rapidly increased. The photon intensity of a laser is coupled to the population difference through the photon rate equation [1,2],

$$\frac{dS(t)}{dt} = -\frac{S(t)}{\tau_p} + \Gamma G(n(t) - n_{tr})S(t) + \frac{\Gamma \beta n}{\tau_g}, \tag{2.1}$$

where $S(t)$ is the photon intensity, τ_p is the photon lifetime, G is the differential gain, $n(t)$ is the instantaneous upper level or band population density, n_{tr} is the population difference required to achieve transparency, Γ is the confinement factor, β is the spontaneous emission coefficient representing how much of the total spontaneous emission enters into a single longitudinal mode, and τ_g is the spontaneous excited state lifetime. The change in photon intensity is calculated from this equation, and the three terms of the right-hand side represent photons lost due to cavity losses, photons entering into a lasing mode due to stimulated emission, and photons entering a lasing mode due to spontaneous emission.

The upper state population density is in turn connected to the photon intensity by the equation,

$$\frac{dn(t)}{dt} = R_{pg} - \frac{n(t)}{\tau_g} - G(n(t) - n_{tr})S(t), \tag{2.2}$$

which gives the rate of change of the population difference. R_{pg} is the pumping rate. The second term on the right hand side represents a decay of the upper state population due to spontaneous emission, and the last term is the change in the population difference due to stimulated emission. The approximations involved in deriving these equations remain valid for sufficiently large reflectivities ($\geq 20\%$), above threshold operation, $\beta > 10^{-12}$, and for pump modulation below the cavity round-trip period, about 60 GHz [2] for semiconductor lasers.

Thus from Eqs. (2.1) and (2.2) one can see that if R_{pg} can be suddenly increased, a sudden overshoot in the population difference will force an abrupt increase in light and a subsequent sudden drop in carrier density (assuming the laser is, as is usually the case, not strongly damped). Typically, such a sudden pumping impulse will produce not a single impulse in photon intensity but a series of sharp optical spikes (or ringing) as the laser settles back to equilibrium. This is referred to as a relaxation oscillation and can be studied through a small signal analysis of the coupled rate equations and found to give a frequency of

$$f_r = \frac{1}{2\pi}\sqrt{\frac{1}{\tau_g \tau_p}(\frac{J}{J_{th}} - 1)}, \tag{2.3}$$

where J is the laser's current density, and J_{th} is the required current density to reach threshold. Methods have been investigated to reduce the ripples beyond the first peak by using bi-directional pulses with some improvement [2], but still parasitics play a strong role in determining the limits of how short the pulse can be. The shortest gain switched pulses have been 24 ps and were achieved in semiconductor lasers [3,4].

2.2 Q-switching

Not only is it possible to generate a short optical pulse by abruptly changing the laser's gain, but short pulses can be generated by changing the laser's cavity loss or equivalently its "Q" (quality factor). This was originally proposed by Hellwarth in 1961 [5] and was the first technique for generation of large optical bursts from a laser. Q-switching is accomplished by keeping the laser cavity loss very high while pumping it. Through this, a large carrier density can be generated in the gain medium. If, next, the cavity loss is reduced (Q is increased) the laser can then suddenly deplete the gain medium, generating an amount of stimulated emission equivalent to this stored excess gain pumping. When the Q-switching is caused by some external active source, we refer to this as active Q-switching. The laser may also be constructed in such a way that it will operate in this manner on its own. A laser with a saturable absorber or even a laser with a nonuniformly degraded gain region will demonstrate Q-switched behavior.

When the population difference reaches a level high enough, light in the laser cavity may begin saturating the absorption. This leads to an increase in the Q of the cavity which further saturates the absorber and suddenly generates an enormous amount of light until the upper state population of the gain medium is well-depleted (Eqn. 2.2) and lasing stops. After some time, the gain section will become strongly inverted and the cycle then begins again. The intensity oscillations are thus a result of the coupling between the population rate equation and the photon rate equation, meaning that the self Q-switching is essentially an undamped relaxation oscillation. However, the oscillation is typically of lower frequency than the relaxation oscillation and does not have the same square root dependence as the relaxation frequency given in the equation (2.3) for the small-signal relaxation frequency [2].

Note, the two methods, gain switching and Q-switching, both result from a physical process where the energy present in the lasing modes of the cavity decays toward zero and rebuilds once in every cycle. The widths of coherent pulses generated through these two methods are therefore limited by the photon lifetime, τ_p. This is contrary to the physical process occurring in the remaining short pulse generation method, modelocking. The decay and rebuilding of the energy in the laser cavity results in not only inherently slower, but also "noisier" trains of pulses. This has been confirmed experimentally with Q-switched lasers giving peak pulse powers of up to 10 W and timing jitter noise of 4-6 ps RMS [6]-[8] (similar to that of gain switching [4]) but has been reduced to 0.8 ps through opto-electronic feedback [8]. Mode-locked lasers have been shown to give peak pulse powers of up to 200 W and 0.22 ps (through hybrid modelocking) timing jitter noise [9]-[11] and to produce pulse trains with coherence lengths of over thousands of pulses [12].

2.3 Modelocking

Modelocking, as opposed to the previous two methods discussed, maintains essentially a constant energy in each mode during the full repetition period. Consider a laser with a number of modes oscillating at once. An ideal homogeneously broadened laser [13], would not be expected to oscillate this way [14], but in realistic cases, it may oscillate in multiple modes. Typically, however, multimode operation will produce oscillations such that no two modes keep a constant phase relationship. Special effort must be made to keep a consistent phase relationship between the modes to achieve coherence throughout the spectrum. As discussed previously, active modelocking was the first method used to force this fixed phase relationship upon the modes.

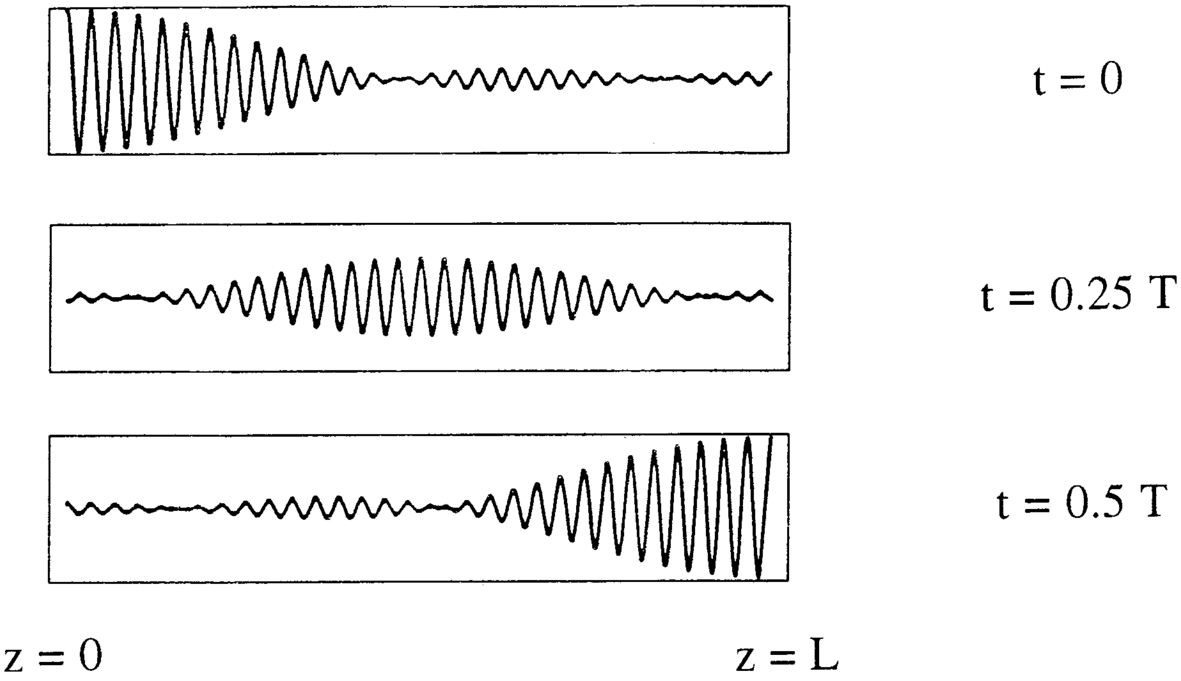

Figure 2.1: Net field distribution plotted for various times within one modelocking cycle. A pulse is seen moving back and forth through the cavity for this simplified plot depicting a result from only 5 modes.

When light exists in a resonator, the energy exists essentially in equally spaced modes [15]. These modes each produce a characteristic standing wave pattern within the resonant cavity and are defined by the requirement of boundary conditions at the ends of the cavity. The net electric field is made up of the sum of these standing waves and would produce different interference patterns and therefore a different net field distribution at various times during a cycle. For a resonator with five modes present, the field distribution is plotted at three different moments in time (Fig. 2.1). Essentially, the resulting field distribution looks like that of energy "sloshing" back and forth in a cavity – or a pulse in the cavity. A loss modulator can be placed at one end of the cavity and be used to change the cavity's loss at the mode-spacing frequency. Using an external source at this frequency one can maintain a high loss in this section of the laser until one expects that the pulse will be passing through. The laser, now, will not operate in continuous wave (CW) operation, since the loss may be held high for a majority of the time, and CW lasing will experience too much loss. In fact, it is most favorable for the laser to operate in such a way that all modes will be in phase at the position of the loss modulation (z=0) when the loss modulator is in its low-loss state (t=0) as shown in Fig. 2.1. In this case one forces the modes to maintain a fixed phase relationship by using some external active source and, therefore, this is referred to as active modelocking. A very elegant analytical theory has been developed to describe this type of modelocking in the time domain, and it is found that the modes are coupled together in a Hermite-Gaussian distributed supermode as the laser is modulated at its cavity round-trip frequency [16]. In fact, this external active source is not always necessary to achieve mode-locked pulses. The laser may be designed in such a way that it will modelock on its own.

2.3.1 Passive modelocking

Unlike in active modelocking, an external timing source is not required for the passively mode-locked laser's operation. Also, contrary to active modelocking, passive modelocking is an inherently nonlinear phenomena which requires material saturation to produce a coupling between the cavity modes. In some ways, passive modelocking has more in common with passive Q-switching than with the linear problem of active modelocking. Physical modelling of passively mode-locked lasers has led to relatively good agreement with some experimental results for mode-locked lasers using an external cavity [17,18]. Assumptions in these time domain models break down as higher repetition rate modelocking is considered especially in monolithic passively mode-locked lasers, to be discussed in chapters 6 and 7. Passive modelocking has led to shorter pulses than each of the other short-pulse techniques discussed so far.

Modelling of passive modelocking has involved time domain analyses and frequency domain analyses. A frequency domain analysis becomes cumbersome when one analyzes a laser oscillating in a large number of (>20) modes [19,20]. The time domain analysis, which has been more thoroughly pursued [17,18,21,22], is more suitable for low duty cycle mode-locked lasers. As it is the dominant model today, the time domain view will be briefly summarized here.

Time domain model

The typical model of a passively mode-locked laser includes a gain section and a saturable absorption section, as shown in Fig. 2.2. The presence of an inverted medium in the laser cavity leads to spontaneous emission and also to a modal gain which amplifies this, leading to amplified optical fluctuations in the laser cavity. Some have chosen to study how these fluctuations eventually lead to modelocking, assuming the right conditions within the laser cavity [23]-[26]. The study of this evolution as the laser settles to a steady state is referred to as the transient problem for passive modelocking and generally shows a stable pulse train can build up in approximately a

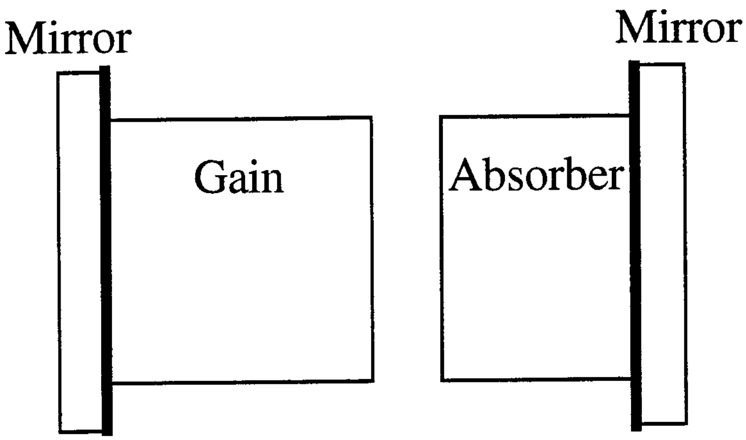

Figure 2.2: Model of two-section passively mode-locked laser. In the semiconductor laser, the right section is contacted and grounded to extract carriers from the saturable absorber. The contact on the left would be forward biased to inject carriers into the gain section.

hundred cavity round-trips. The transient problem is interesting and also worthy of study, but is not a major subject of this thesis. Further discussion of this approach will appear at the end of this chapter.

From experimental work with lasers [27,28], one gathers that through whatever evolutionary path, the passively mode-locked laser may develop stable intensity pulses after some finite start-up time. When an intensity pulse exists in the cavity and travels through the absorber, it will saturate the absorber; it drives the carrier density toward the point of transparency. After the pulse passes, the absorber section carrier density will exponentially recover. The gain will also begin to saturate if it is hit with enough energy; it will be driven toward transparency, and after some time it will recover. A

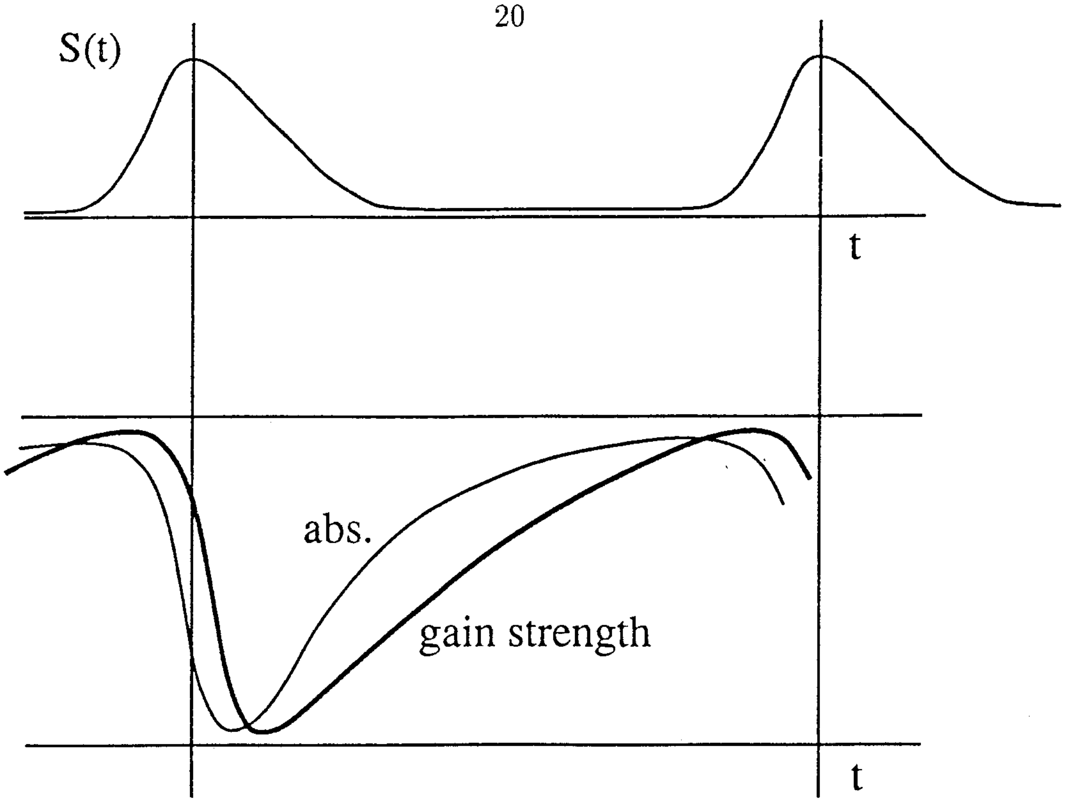

Figure 2.3: A plot of the temporal change of photon intensity (upper plot) along with strength of gain section (thicker line) and strength of absorber section (thinner line) during one mode-locking cycle.

temporal plot of the physics of the pulse intensity envelope, the absorber saturation, and the gain saturation are displayed during one repetition cycle in Fig. 2.3 [17,21]. For a stable pulse train to exist one requires a net gain to exist during the pulse and a net loss on the wings and elsewhere between pulses. This implies that:

(1.) The absorber must saturate more quickly during the pulse than the gain section (have a lower saturation energy), and

(2.) the absorber must recover more quickly, and along with the cavity losses, reach a stronger net absorption than the gain section during this recovery interval.

In semiconductor physics we are incredibly lucky that this generally happens automatically [29,30]. This occurs since the differential absorption of the gain section is smaller than the differential absorption of the absorber section. Physically, this results since a certain length of semiconductor material can only offer a finite gain, and the increase in gain eventually broadens and saturates with increased pumping.

The common time domain model assumes a steady state pulse electric field envelope, $E(t)$, where the net electric field is given by $\mathcal{E}(t) = Re[E(t)e^{i\omega_0 t}]$, and ω_0 is the center optical frequency. The corresponding Fourier transform of the envelope is $E(\Omega)$ such that $\Omega = \omega - \omega_0$. As initially described by Haus, one may take into account the bandwidth filtering inside the cavity, the saturation of the gain section and the saturation of the absorber section. By the definition of steady-state operation, the pulse envelope must return to its original shape after an integral number of round trips. Near the peak gain for the laser cavity, one may consider the net cavity loss transfer function to be nearly parabolic, having some width $\Delta\omega$. This effect alone would modify the spectrum after one round trip to create,

$$E_1(\Omega) = e^{\frac{-(\omega-\omega_0)^2}{\Delta\omega^2}} E_0(\Omega). \tag{2.4}$$

When the modes are relatively close together inside this mode-locked spectral envelope (more exact discussion of this approximation will be undertaken in chapter 6) and the deviation from and width of the spectrum are small compared to the gain bandwidth, the Fourier transform of $E_1(\Omega)$ may be taken to find the output pulse envelope in terms of the original,

$$E_1(t) = e^{(\frac{1}{\Delta\omega^2}\frac{d^2}{dt^2})}E_0(t) \approx (1 + \frac{1}{\Delta\omega^2}\frac{d^2}{dt^2})E_0(t). \tag{2.5}$$

Likewise, a group velocity dispersion (GVD) will achieve the same effect except that a quadratic phase rather than a quadratic amplitude is placed upon the original spectrum,

$$E_2(\Omega) = e^{-iD(\omega-\omega_0)^2}E_1(\Omega) \approx (1 - iD(\omega-\omega_0)^2)E_1(\Omega) \tag{2.6}$$

which correspondingly becomes

$$E_2(t) = (1 + iD\frac{d^2}{dt^2})E_1(t) \tag{2.7}$$

after a round trip through the cavity.

Other physical effects on the pulse are due to the gain and saturation of the gain section which are most easily described in the time domain,

$$E_3(t) = e^{g(t)}E_2(t), \tag{2.8}$$

where $g(t) = g_i e^{-\sigma_g \int_{-\infty}^{t} |E_2(t)|^2 dt}$ includes the nonlinear gain effects. Here, $g(t)$ is the instantaneous gain of the gain section, g_i is the unsaturated gain, and σ_g is the cross section of the gain material involved. Similarly, the saturation of the absorber results in

$$E_4(t) = e^{-a(t)}E_3(t), \qquad (2.8)$$

where $a(t) = a_i e^{-\sigma_a \int_{-\infty}^{t} |E_3(t)|^2 dt}$. Haus assumes all single pass effects are small from each element and thus the order of operations is unimportant since all these exponentials are expanded to first order. Thus, since one requires $E_4(t) = E_0(t)$, for steady-state operation one finds,

$$(g(t) - 1 - a(t) + l\frac{1}{\Delta\omega^2}\frac{d^2}{dt^2} + iD\frac{d^2}{dt^2})E_0(t) = E_0(t). \tag{2.9}$$

From the population rate equation, one finds essentially exponential decays towards transparency for absorber and gain. Absorption saturation is approximated by a second order Taylor series dependence on time and gain saturation, which is slower, is approximated by a first order (in time) saturation. Haus proved that for these approximations, the function *sech* is a consistent solution. Martinez [18] extended the analysis to that including phase effects from a fast saturable absorber and arrived at

$$E(t) = V_0 sech(t/\tau)e^{i\beta \ln(sech(t/\tau))}, \tag{2.10}$$

where

$$\tau = (\frac{4}{\sigma_a \Delta\omega W})(\frac{l_0}{l_i})^{1/2}, \tag{2.11}$$

with

$$W = \int_{-\infty}^{\infty} |E(t)|^2 dt \tag{2.12}$$

being the normalized pulse energy. Here l_0/l_i is the ratio of DC loss to saturable absorber loss, and β is the chirp parameter. The results in some cases compare well to full numerical calculations [31]-[33].

Martinez et al. include phase effects from fast saturable absorption, but the phase effects which result from changes in carrier population in semiconductor lasers are due to slow saturable effects (i.e., they are due to population state changes and not nonresonant Kerr nonlinearities), thus, in the case of the semiconductor laser, the chirp effects are proportional to energy and not to intensity as Martinez et al. derive them for a distinct case [18].

The resulting analysis gives pulse shapes and pulse widths for the specially chirped pulses. It also gives some direction on how to modify laser parameters including unsaturated absorption strength, relative saturation energy, and gives reasonably good agreement with lasers showing negligible self phase modulation (SPM). Another extension of Haus' work by J. Chen has been published recently but considers only the fast SPM case also [22]. To date, no steady state analysis including SPM from slow saturable material has been published.

Models for studying transient effects in passive modelocking

Simulations which model the mode-locked lasers from transient all the way to steady-state oscillations have been undertaken [24,25]. Assumptions involved in making this problem tractable are different than those of the other approaches, therefore, results will complement and/or confirm those from other theoretical work. All results published to date have followed one of two distinct approaches: travelling wave calculations for modelocking build-up to the steady state [25] or the supermode competition model [34]. In general, these models have not done well in taking into account the expected physical phemomena in semiconductor lasers [27]. In all transient modelling of passive modelocking so far, no SPM has been successfully incorporated, as this is a stumbling block when one does not consider the phase coherence effects from $E(t)$ and only considers the intensity. Surprisingly some agreement, at least in the form of comparable width pulses, has been obtained without incorporating SPM. Even without considering SPM, the calculations are highly computational since they require one to proceed through a huge sequential evolution of the light and material in many discrete modelled sections within the cavity. Due to the computational aspect of this problem, there is more difficulty in arriving at an intuitive understanding or relationships between parameters, than from the steady-state analyses. Although the transient calculation has not contributed much yet, perhaps as modelling techniques and computing equipment continue to improve, this method will offer valuable insight.

References

[1] D. A. Kleinman, *Bell Sys. Tech. Jour.*, **43**, 1505 (1964).

[2] K. Y. Lau, *Ph.D. Thesis*, California Institute of Technology (1981).

[3] I. H. White, P. S. Griffin, M. J. Fice, and J. E. W. Whiteaway, *Electron. Lett.*, **28**, 1257 (1992).

[4] J. M. Wiesenfeld, G. Hasnain, J. S. Perino, J. D. Wynn, R. E. Leibenguth, Y. H. Wang, and A. Y. Cho, *J. Quantum Electron.*, **29**, 1996 (1993).

[5] R. W. Hellwarth, **Advances in Quantum Electronics**, edited by J. R. Singer, p. 334, Columbia University Press, New York (1961).

[6] P. P. Vasil'ev, *J. Quantum Electron.*, **24**, 2386 (1988).

[7] S. Bouchoule, N. Stelmakh, M. Cavelier, and J. M. Lourtioz, *IEEE J. Quantum Electron.*, **29**, 1693 (1993).

[8] K. A. Williams, I. H. White, D. Burns, and W. Sibbet, *Electron. Lett.*, **30**, 1687 (1994).

[9] P. J. Delfyett, L. Florez, N. Stoffel, T. Gmitter, N. Andreadkis, G. Alphonse, and W. Ceislik, *Opt. Lett.*, **17**, 670 (1992).

[10] R. J. Helkey, W. X. Zou, A. Mar, D. B. Young, and J. E. Bowers, *Microwave and Opt.*, **9**, 115 (1995).

[11] S. Arahira and Y. Ogawa, *Electron. Lett.*, **31**, 808 (1995).

[12] D. W. Rush, P. T. Ho, and G. L. Burdge, *Opt. Commun.*, **52**, 41 (1984).

[13] A. Yariv, **Quantum Electronics**, 3rd ed., Wiley, New York (1989).

[14] K. Petermann, **Laser Diode Modulation and Noise**, ch. 1-3, Kluwer Academic Publishers, Boston (1991).

[15] A. E. Siegman, **Lasers**, ch. 1, University Science Books, Mill Valley, CA (1986).

[16] H. A. Haus, *IEEE J. Quantum Electron.*, **11**, 323 (1975).

[17] H. A. Haus, *IEEE J. Quantum Electron.*, **11**, 736 (1975).

[18] O. E. Martinez, R. L. Fork, and J. P. Gordon, *J. Opt. Soc. Am. B*, **2**, 753 (1985).

[19] K. Y. Lau, *IEEE J. Quantum Electron.*, **26**, 250 (1990).

[20] R. A. Salvatore, S. Sanders, T. Schrans, and A. Yariv, "Supermodes of high-repetition-rate passively mode-locked semiconductor lasers," submitted to *IEEE J. Quantum Electron.*

[21] G. H. C. New, *IEEE J. Quantum Electron.*, **10**, 115 (1974).

[22] J. C. Chen, H. A. Haus, and E. P. Ippen, *IEEE J. Quantum Electron.*, **29**, 1228 (1993).

[23] A. J. Lowery, *Electron. Lett.*, **26**, 939 (1990).

[24] A. J. Lowery, *Electron. Lett.*, **28**, 545 (1992).

[25] W. Yang and A. Gopinath, *Appl. Phys. Lett.*, **63**, 2717 (1993).

[26] D. J. Jones, L. M. Zhang, J. E. Carroll, and D. D. Marcenac, *IEEE J. Quantum Electron.*, **31**, 1051 (1995).

[27] D. J. Derickson, R. J. Helkey, A. Mar, J. R. Karin, J. G. Wasserbauer, and J. E. Bowers, *IEEE J. Quantum Electron.*, **28**, 2186 (1992).

[28] S. Sanders, T. Schrans, A. Yariv, J. Paslaski, J. E. Ungar, and H. A. Zarem, *Appl. Phys. Lett.*, **59**, 1275 (1991).

[29] P. W. Smith, Y. Silberberg, and D. A. B. Miller, *J. Opt. Soc. Am. B*, **2**, 1228 (1985).

[30] R. A. Salvatore, T. Schrans, and A. Yariv, *Opt. Lett.*, **20**, 737 (1994).

[31] M. S. Stix and E. P. Ippen, *IEEE J. Quantum Electron.*, **19**, 520 (1983).

[32] J. Hermann, F. Weidner, and B. Wilhelmi, *Appl. Phys. B*, **26**, 197 (1981).

[33] J. Hermann and F. Weidner, *Appl. Phys. B*, **27**, 105 (1982).

[34] O. Solgaard, M. H. Kiang, and K. Y. Lau, *Appl. Phys. Lett.*, **63**, 2021 (1993).

Chapter 3

Experiments with passively mode-locked external cavity semiconductor lasers

3.1 Setup and operation of ultrashort pulse semiconductor lasers

There are two categories which all passively mode-locked semiconductor lasers can be classified into: those that involve an external cavity and those that do not. In this chapter we will be solely concerned with the first type which are also chronologically the first type that had been demonstrated [1].

The lasers used in each of these experiments are one of two types: ridge-waveguide lasers processed directly from molecular beam epitaxy (MBE) material or buried heterostructures from MBE material and liquid phase epitaxy (LPE) regrowth [2]. In either case, along the direction of growth, there is an MBE-grown graded index region with between one and four quantum wells (reasons for number of wells will be discussed in the section on modal bandwidths). The two semiconductor laser structures are shown in Fig. 3.1 and Fig. 3.2.

The lasers are processed photolithographically so that contacts on the top (p-side) are divided into at least two sections. A thin layer of Silicon dioxide (SiO_2) first is placed over the full p-side and removed over the 2-3 μm stripe region. Metal contacts of Cr and Au or ZnAu and Au are evaporated over each region on the top side, and a single metal contact of AuGe and Au is evaporated onto the bottom side (n-side) of the diode. These contacts are then annealed to produce low resistance ohmic contacts. For more detailed processing information see [3]. To achieve the necessary gain reduction for stable modelocking, it is required that one section be kept at a carrier density below its transparency (n_{tr}). Also, to achieve oscillation, one section must be forward biased to a point that provides at least enough gain to meet the threshold requirement for the full laser cavity. All successful configurations for passive modelocking presented here used the longer section of the laser as the gain section and the shorter section as the saturable absorber section. The external cavity is provided by a beam splitter with between 30% and 80% power reflectivity or in some cases a 600 line/mm grating. Typically a 40 power microscope objective is used to couple the semiconductor laser to an external cavity of between 10 and 50 cm in

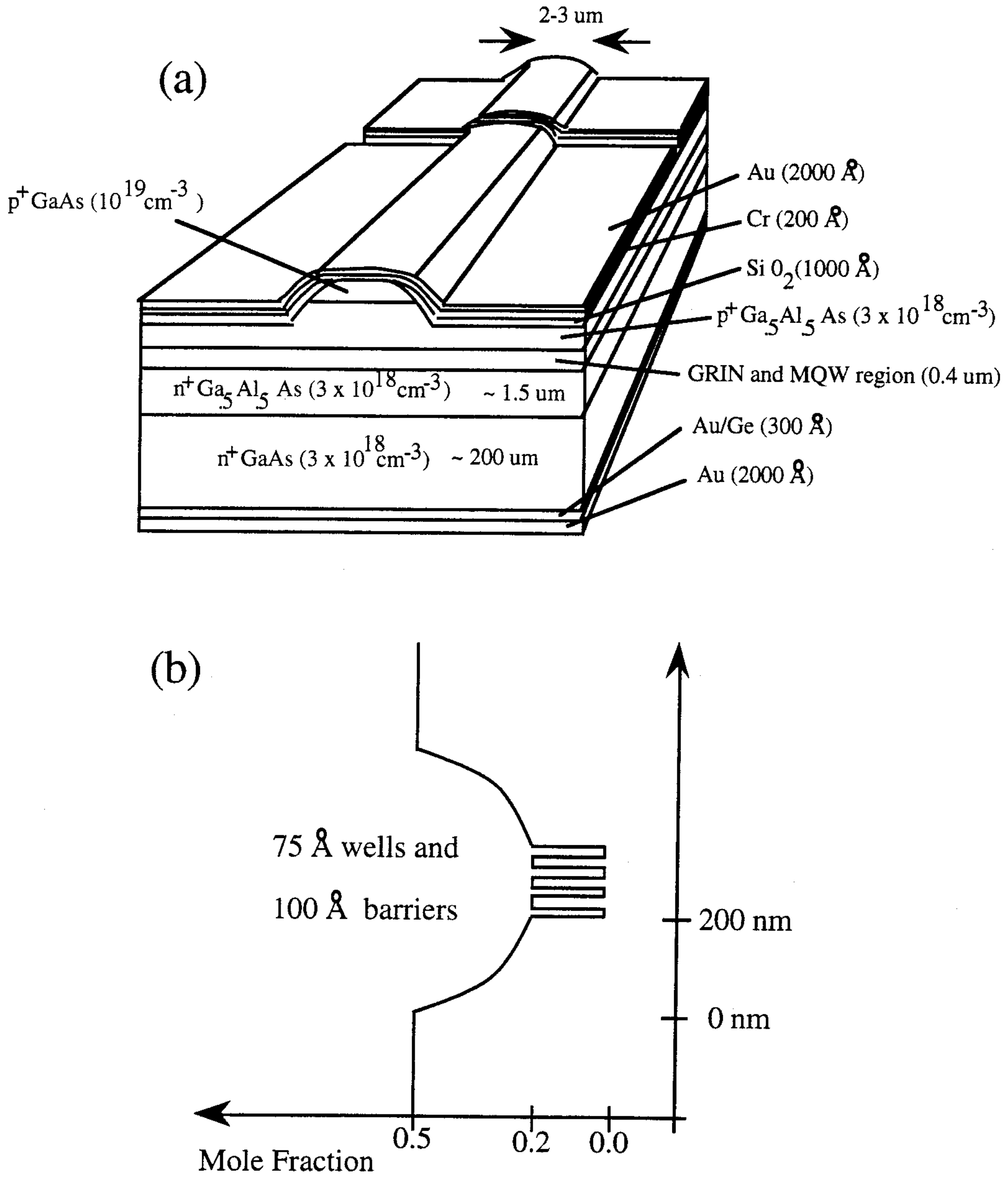

Figure 3.1: Structure of stripe laser (a) along with expanded image of the laser's active region (b).

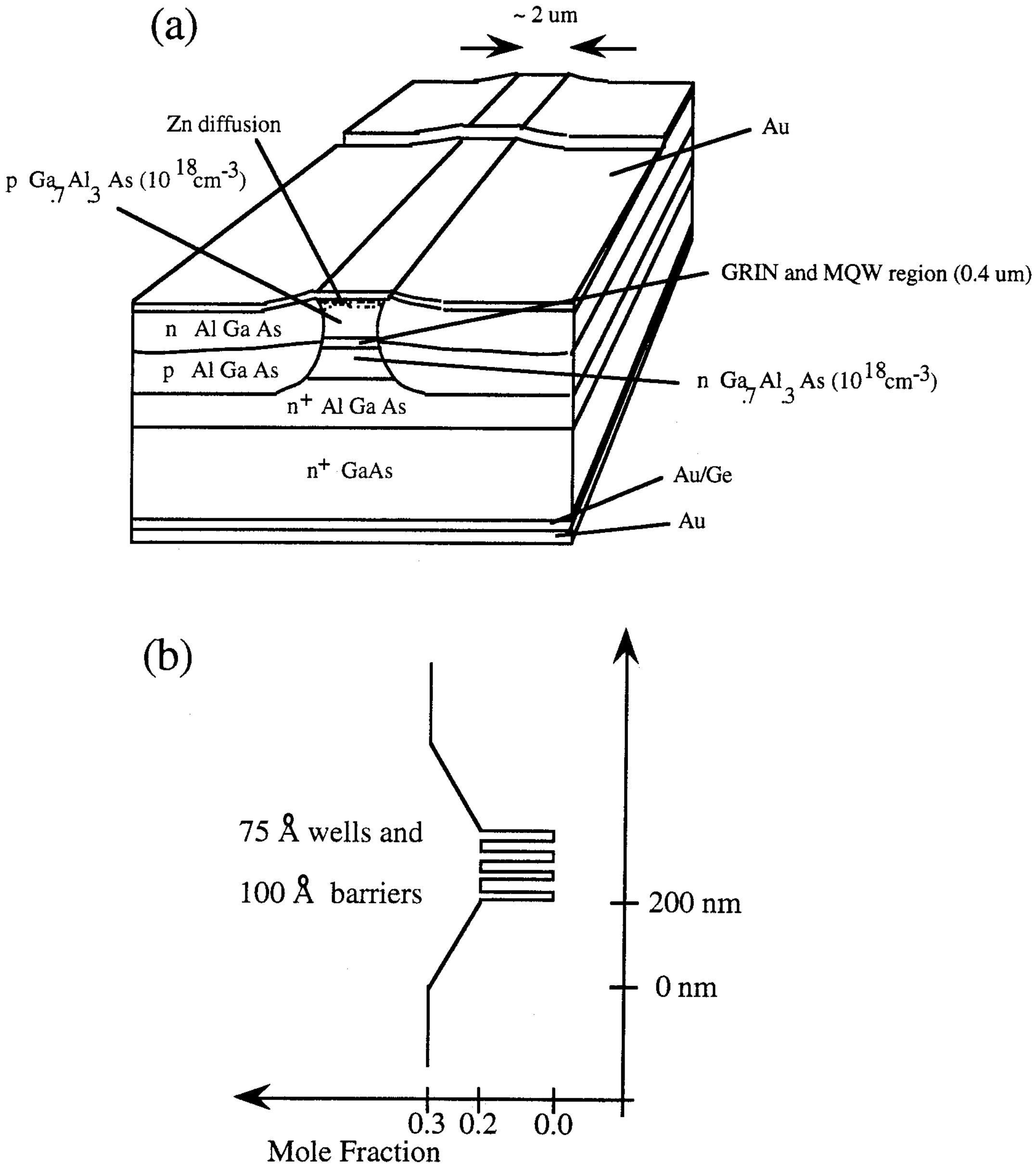

Figure 3.2: Structure of LPE regrown laser (a) along with expanded image of the laser's active region (b).

length.

One sees a peak in light output due to increased feedback in a couple of main cases. These correspond to two positions for the intracavity lens: the lens may be placed at a distance of one focal length from the semiconductor laser to produce a collimated beam at the planar feedback mirror, or the lens may be placed slightly beyond one focal length from the laser such that the laser's field distribution from the end of the waveguide is imaged on the mirror. Although the first case is seen to give significant feedback into the laser, it is known to invert the transverse mode profile $a(x, y) \rightarrow a(-x, -y)$ and has also been shown to be inferior in achieving modelocking. All results in this thesis are for the second configuration where the laser output is focused to a spot on the external cavity mirror or grating. To enhance coupling and reduce satellite pulses, an antireflection (AR) coating (usually $\leq 5\%$ power reflectivity) is placed on the laser's gain section facet since it is within the compound cavity. A diagram of the external cavity setup is shown in Fig. 3.3.

Special steps are taken to isolate the separate laser contacts. A wet etch of Hydrofluoric acid (HF) is used to etch through the SiO_2 layer in the region between the contacts and a subsequent etch of the highly doped cap layer on the p-side of the graded index region is used to obtain at least 5 kΩ of isolation between the adjacent sections.

Once this laser with integrated saturable absorber is set up in the external cavity configuration and is biased as mentioned, it will produce pulses of about 3-5 ps, typically. Accurate measurement of the pulse widths requires resolution shorter than

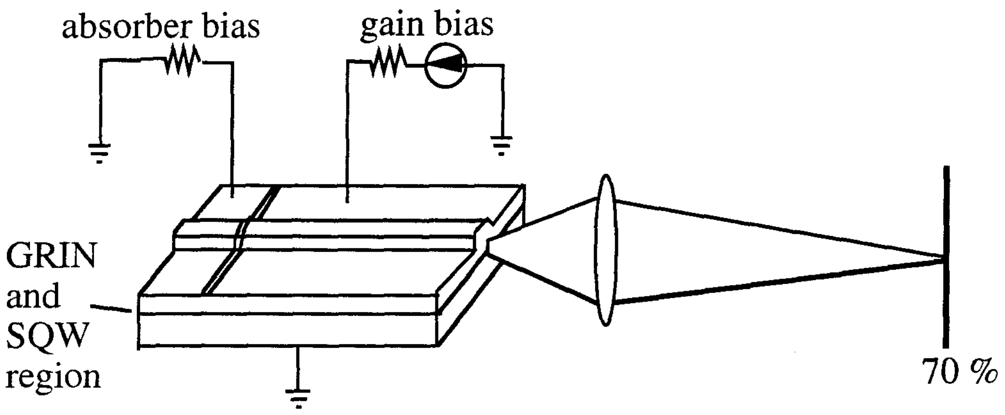

Figure 3.3: The two section passively mode-locked laser coupled to an external cavity is set up with AR coating on gain facet and device output focused to a point on the 70% mirror.

the response of any commercially available electronics, thus, special techniques must be used to measure the widths.

3.2 Standard autocorrelation pulse measurement techniques

The general theory of intensity autocorrelations is presented in [4]. In the simplest case, one beam splitter, two mirrors, one non-centrosymmetric crystal, and a detector are necessary for intensity autocorrelation measurements. The beam splitter is used to send the beam along two orthogonal arms of a Michelson interferometer, and to collinearly recombine the beams after they return from mirrors at the end of each arm. Next, they are sent into a nonlinear second harmonic generation (SHG) crystal (either Lithium Iodate, $LiIO_3$, or Beta Barium Borate, BBO, in our cases). Since one mirror is moveable, the temporal overlap of the pulses can be varied within the crystal. If the pulses do not overlap temporally, an average signal strength of one unit will be generated at the second harmonic of the optical frequency by the crystal. If overlap is perfect, an average intensity of three will now be produced by the crystal. Valid pulse measurements will possess this 3 to 1 ratio, whereas noise correlation spikes are expected to generate a 3 to 2 ratio. The resulting intensity generated by the crystal at the second harmonic is proportional to

$$I^{(2\omega)}(\tau) = \int_{-\infty}^{\infty} |E(t)|^4 dt + \int_{-\infty}^{\infty} |E(t-\tau)|^4 dt + 4\int_{-\infty}^{\infty} |E(t)|^2 |E(t-\tau)|^2 dt +$$

$$4\int_{-\infty}^{\infty} (|E(t)|^2 + |E(t-\tau)|^2) Re(E(t)E^*(t-\tau)e^{j\omega_0\tau}) dt +$$

$$2\int_{-\infty}^{\infty} Re((E(t)E^*(t-\tau)e^{j\omega_0\tau})^2) dt. \tag{3.1}$$

In the above case, it is assumed that a measurement is taken while the mirror position is being scanned and the averaging time used is long enough to eliminate the interferometric fringes (the last two of the five terms) caused by resolution comparable to the individual optical cycles.

Measurements including the interferometric autocorrelation fringes have been used to gather more information about pulse shape and pulse chirp. These, however, have only been demonstrated for pulses of 1 ps or less since otherwise they involve a large number of oscillations and pose an extremely strict requirement for the translation and linearity of the translational equipment. They have also not been demonstrated to give decent experimental results for average powers below 100 mW. Additionally, pulses with nonlinear chirp and pulses outside of the common expected pulse shapes (especially asymmetrically shaped pulses) pose a major problem for this technique [5]. New types of measurements have been made to determine the actual pulse shape and chirp of semiconductor laser pulses and these techniques will be presented in the sections on pulse shape and nonlinear chirp measurements, respectively.

From the laser setup in the previous figure, a standard autocorrelation is shown in Fig. 3.4. One can see the 3 to 1 ratio in the intensity autocorrelation. Two satellite pulses are seen in the autocorrelation and result from the imperfect antireflection coating. The full width at half maximum (FWHM) of this autocorrelation is about 6.2 ps and corresponds to a pulse width of about 4.0 ps assuming a $sech^2$ pulse shape. The corresponding spectrum plotted under the same conditions is shown in Fig. 3.5. It has a FWHM of 6.0 nm. Small ripples can be seen in the spectrum and correspond to the 14 ps spaced satellite pulses from the imperfect reflection coating and show up as small 70 GHz period ripples in the compound cavity spectrum.

Every pulse shape has a time-bandwidth limit. For example, if one wants to generate a 1 ps pulse, then one is required to generate an intensity spectrum, $|E(f)|^2$, that is about 0.4 THz (or at 850 nm, nearly 1.0 nm) FWHM. From the two figures, one can easily see that the time-bandwidth product which is 10 here is about 25 times in

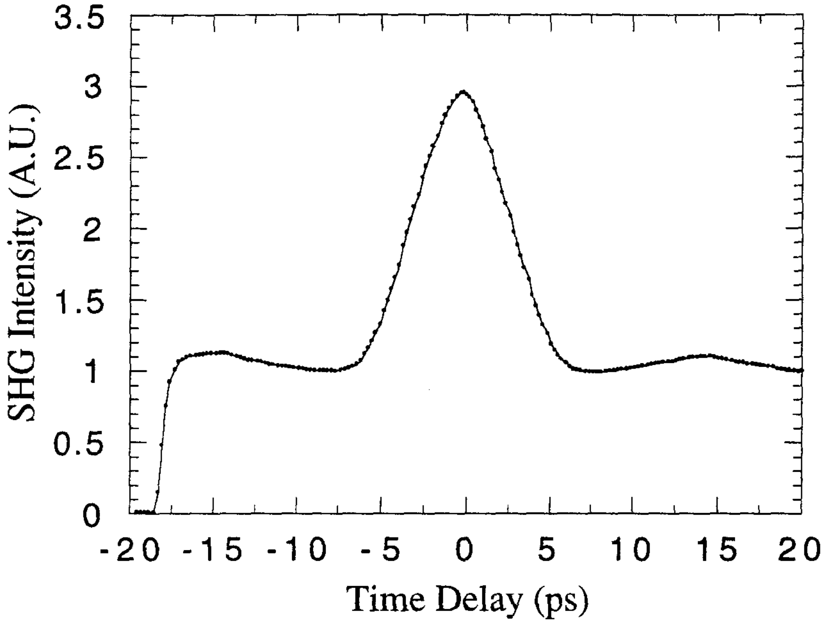

Figure 3.4: Example of a collinear intensity autocorrelation is measured by varying the relative delay, τ, of the pulses with the Michelson interferometer and sending output into a SHG crystal.

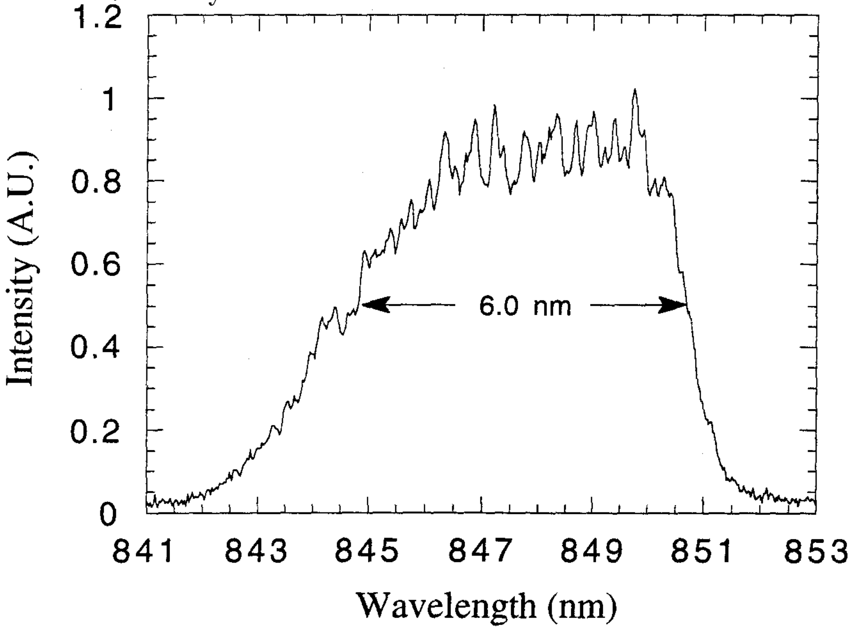

Figure 3.5: Optical spectrum of the passively mode-locked laser includes about 4000 external cavity modes within its FWHM.

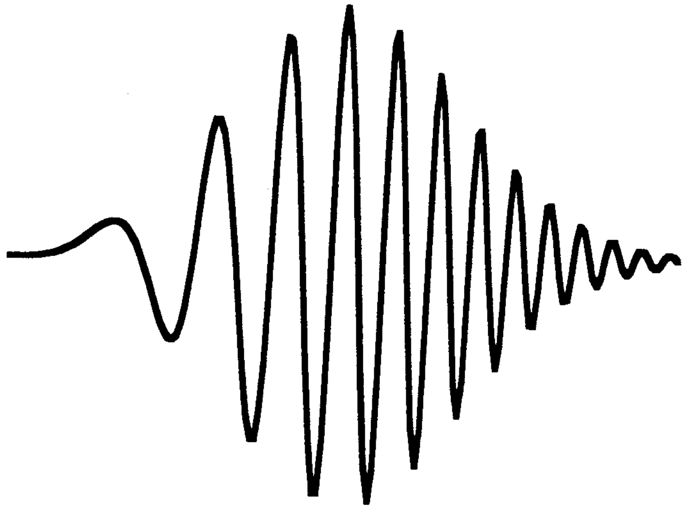

Figure 3.6: Representation of an up-chirped Gaussian pulse has a lower frequency at the beginning of the pulse and proceeds to higher frequency.

excess of the expected time-bandwidth product. A table of expected time-bandwidth products for common pulses and spectral shapes is shown in Table 3.1.

3.3 Dispersion compensation

The excess time-bandwidth product will be shown to be due to a chirp on the pulses. A chirped pulse is a pulse whose instantaneous frequency changes with time during the pulse. For example a Gaussian pulse with a linear upchirp is plotted in Fig. 3.6. This can be written as a Gaussian envelope having a quadratic phase upon the carrier,

$$E(t) = e^{-(a-ib)t^2} e^{i\omega_0 t} \tag{3.2}$$

Shape, $I(t)$	$\Delta\tau_w$	$\lvert E(f)\rvert^2$	Δf	$\Delta\tau_w\Delta f$
Gaussian				
$e^{-2\Gamma t^2}$	$\sqrt{\frac{2ln(2)}{\Gamma}}$	$e^{-2\pi^2 f^2/\Gamma}$	$\frac{\sqrt{2\Gamma ln(2)}}{\pi}$	0.441
Rect/Sinc				
$\mathrm{rect}(t/\tau)$	τ	$\mathrm{sinc}^2(\pi\tau f)$	0.886τ	0.886
Hyperbolic secant				
$\mathrm{sech}^2(t/\tau)$	1.763τ	$\mathrm{sech}^2(\pi^2\tau f)$	$\frac{1.763}{(\pi^2\tau)}$	0.315
Double-sided exp.				
$u(-t)e^{2\Gamma t} + u(t)e^{-2\Gamma t}$	$\frac{0.693}{\Gamma}$	$\frac{1}{\Gamma^2+(2\pi f)^2}$	Γ/π	0.221
Cosine				
$\cos^2(2\pi t/\tau)$	$\tau/4$	$\lvert\delta(f-\frac{1}{\tau})+\delta(f+\frac{1}{\tau})\rvert^2$	$2/\tau$	0.500
3-mode triangle spect.				
$(\frac{1}{2}+\frac{1}{\sqrt{2}}\cos(2\pi t/\tau))^2$	$\frac{2.095\tau}{2\pi}$	$\lvert\frac{1}{\sqrt{2}}\delta(f+\frac{1}{\tau})+\delta(f)+\frac{1}{\sqrt{2}}\delta(f-\frac{1}{\tau})\rvert^2$	$2/\tau$	0.667
3-mode rect spect.				
$(e^{it}+1+e^{-it})^2$	0.621π	$\lvert\delta(f+1)+\delta(f)+\delta(f-1)\rvert^2$	$1/\pi$	0.621

Table 3.1: Time-bandwidth products for common functions.

or equivalently in frequency domain, a Gaussian with a quadratic spectral phase,

$$E(\Omega) = e^{-[\frac{a+ib}{4(a^2+b^2)}]\Omega^2}. \tag{3.3}$$

There are a number of ways of removing quadratic phase: using gratings [6,7], prisms [8], chirped fiber gratings [9], phase conjugation half-way through the dispersive path [10], phase modulation from an external modulator [11], or using nonlinear phase effects [12].

When a pulse passes through a linear dispersive material or system, typically it spreads out. An optical spectrum of $F(\omega)$ will become

$$F(\omega)e^{i(\phi_0+\frac{d\beta}{d\omega}(\omega-\omega_0)L+\frac{1}{2}\frac{d^2\beta}{d\omega^2}(\omega-\omega_0)^2L+\frac{1}{6}\frac{d^3\beta}{d\omega^3}(\omega-\omega_0)^3L+\ldots)}, \tag{3.4}$$

where the phase terms have the following effects:

(1.) The constant phase, ϕ_0, only causes a shift in the phase of the carrier and therefore has no noticeable effect on the pulse shape.

(2.) The term linear in $(\omega - \omega_0)$ produces an advance or delay of the pulse envelope and is usually referred to as the group delay due to dispersion, $\tau = \frac{d\beta}{d\omega}L$.

(3.) The term quadratic in $(\omega - \omega_0)$ is the first one to affect the pulse shape. It is generally the term responsible for broadening pulses and is referred to as the group velocity dispersion (GVD).

(4.) The term cubic in $(\omega - \omega_0)$ is the first one to cause an asymmetric distortion in the pulse shape and is considered the first term to contribute to nonlinear chirp.

Since the dominant effect of dispersion from a grating pair or from a non-resonant material is the third effect listed, that is our first concern. A grating pair or non-resonant frequency region for a material will add a nonlinear chirp, however, this effect is on the order of $\Delta\omega/\omega_0$ or the fractional bandwidth of the signal which is down by a factor of more than 1/100 for the experiments done here, and therefore, can be considered negligible in these experiments. So, a pulse envelope

$$E(t) = e^{-\alpha t^2} \tag{3.5}$$

would be found to broaden into a chirped pulse of

$$E(t) = e^{-t^2(1/\alpha - i2\frac{d^2\beta}{d\omega^2}L)/((1/\alpha)^2+(2\frac{d^2\beta}{d\omega^2}L)^2)} \tag{3.6}$$

upon travelling a distance, L, through the dispersive system. However, the addition of dispersion from a grating pair is a linear operation therefore any broadening from linear chirp that has been placed on or already exists on a pulse, can be removed. For example the broadened Gaussian in (3.2) having a width of

$$\tau_p = 2\sqrt{\frac{\ln(2)}{a}} \tag{3.7}$$

can be compressed to a minimum width of

$$\tau_p = 2\sqrt{\frac{a\ln(2)}{a^2+b^2}} \tag{3.8}$$

by choice of an equal and opposite quadratic phase such that $(d^2\beta/d\omega^2)L = b/(a^2 + b^2)/2$. Through proper adjustment of the spacing in the dual grating system, either sign of dispersed pulses (up-chirped or down-chirped) can be compensated and this may compress a pulse well as long as the chirp is very linear.

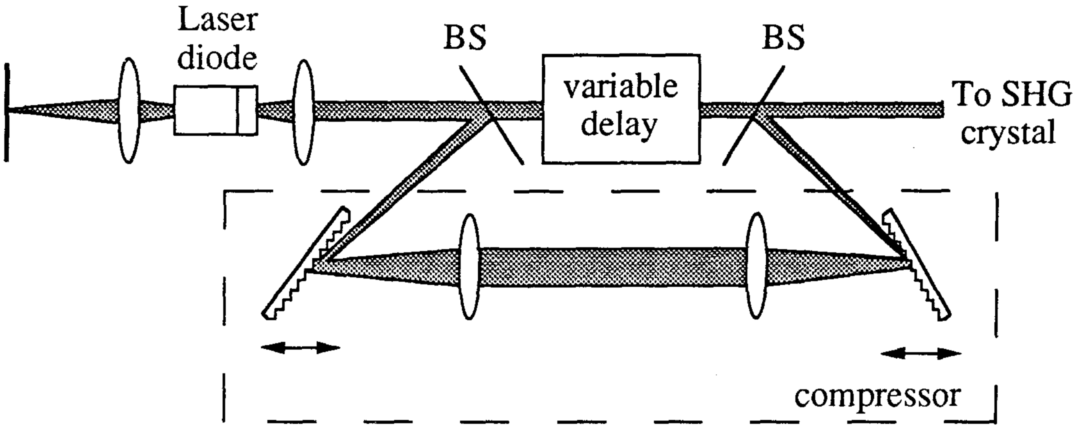

Figure 3.7: Telescoped dual-grating compressor adds negative GVD if gratings are outside of lens' focal lengths, or adds positive GVD if gratings are within the lens' focal lengths.

Compressed pulses have been obtained from the passively mode-locked semiconductor laser [13,14] and, thus, the chirp has been found to be quite linear. The setup for this experiment is shown in Fig. 3.7. Using the buried heterostructure variety of laser with a quadruple quantum well structure as described in section 3.1, pulses with time-bandwidth products between 3 and 10 were obtained with no dispersion added. The gain section was pumped with between 38 mA and 50 mA in forward bias, and the absorber section was grounded through a 100 Ω resistor. The output of the laser was taken from a 70% mirror and sent through a single-pass telescoped grating compressor. The light exiting the compressor was directed to the collinear second harmonic intensity autocorrelator or a monochromator for analysis.

These measurements were performed with the laser modelocked in the first harmonic of the external cavity (558 MHz) and compression ratios typically of 10 to 18 times were obtained [14]. Increased autocorrelation widths were obtained for increased gain section drive currents giving typically 2.5 to 4.5 ps pulses (for different cavity alignments) for 40 mA and typically 4.0 to 6.3 ps pulses for pumping at 48 mA. A slightly broader spectrum was also obtained at higher currents and led to narrower pulses after compression. Optimally compressed pulses resulted in deconvolved pulse widths of 600 fs and 320 fs at 40 mA and 48 mA, respectively. The uncompressed, and the compressed pulse autocorrelations for 46 mA are shown in Fig. 3.8 and Fig. 3.9. All compressed pulses were obtained with the dual grating compressor having the second grating positioned beyond one focal length from the lens, providing a negative GVD to cancel the laser's up-chirp. Typical pulse energies exiting the laser were 1.3 pJ for a gain current of 46 mA. Losses from the compressor system reduced this to 0.6 pJ per pulse which corresponds to a peak power of 2.0 W for a 0.32 ps pulse.

3.4 Tunability and excitonic peak requirements

Near the time when pulses from passively mode-locked lasers were first compressed to subpicosecond widths (1985-1990), much discussion centered around the necessity of exciton states for the fast saturation and recovery in multiple quantum well material [15]-[18]. The exciton is a bound electron-hole pair and may exist within the quantum well. Because it has a characteristic binding energy, the exciton transition leads to a

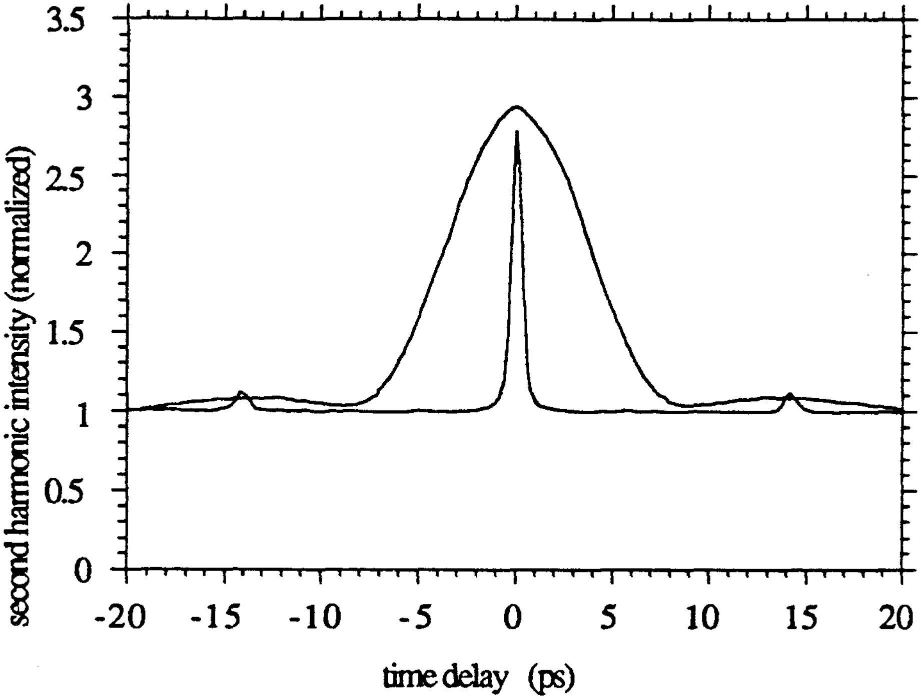

Figure 3.8: Autocorrelation for uncompressed pulse which comes directly from laser at 46 mA gain current. Compressed pulse shown for comparison after optimizing grating spacing to achieve minimum pulse width.

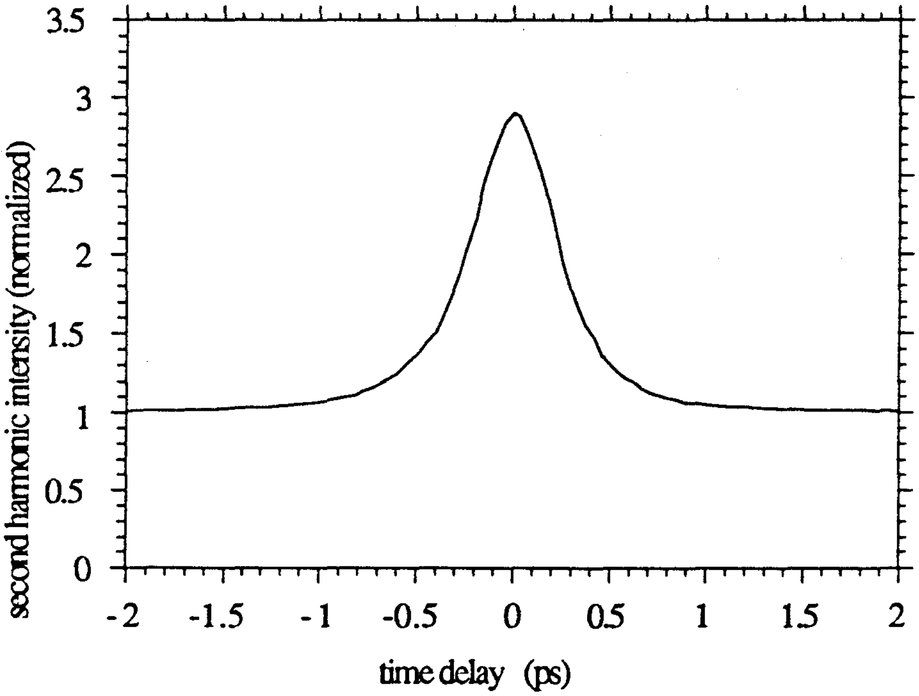

Figure 3.9: Same autocorrelation of compressed pulse on a more adequate scale.

narrow peak in absorption at energies slightly below the band edge for the absorber section. The gain section, on the other hand, is biased strongly enough to achieve inversion and this, as is well known experimentally, causes a bandgap shrinkage from the gain material and shifts its gain spectrum to overlap effectively with the excitonic peak from the absorber section. Since the excitonic state saturation takes place at intensities about one order of magnitude less than interband MQW saturation, it is able to saturate much earlier in the pulse than the gain section as passive mode-locking requires. Recovery is also, as required, a faster process for excitonic states since it results from free electron screening of the excitonic states and occurs typically on the order of 100 ps, as opposed to the slower interband recombination time of about 1 ns in GaAs or InGaAs material. Smith et al. [15], found evidence of the excitonic absorption in proton bombarded and unbombarded MQW material in their passively mode-locked lasers.

Having a different MQW structure and a multi-contact lasers structure rather than an uncontacted free-standing absorber, we have carried out measurements of the absorption spectrum for our devices. Electro-absorption measurements were made with a single-mode tunable Titanium sapphire (Ti:sapphire) laser over the wavelength range of 810 nm to 870 nm. The optical beam was attenuated to very low levels and focused onto the absorber facet of the laser. The gain section was left unbiased. Various biases, 0 to 2 V reverse bias, were maintained on the absorber section and the average current was measured as the Ti:sapphire laser was manually scanned across the relevant wavelength range for the GaAs material. In summary, the results show a clear band edge with essentially a monotonic increase in the current measured from the absorber section as the Ti:sapphire laser was scanned to shorter wavelengths. It was concluded that either due to the existence of nonuniform quantum wells of the quadruple well structure or the presence of the external circuit sweeping carriers generated from interband transitions out of the MQW absorbing structure and masking the small number of excitonic transitions, no prominent excitonic transition line was apparent in our devices.

The exciton peak from the absorber is narrow (typically < 3 nm) and places a strict frequency requirement on the operation of the laser. It was found that one could change the operating wavelength of actively mode-locked lasers. Thus, it seemed likely that there were other ways to see the excitonic effect. By changing the frequency of the feedback with a frequency selective element in the cavity, one may change the operation of the mode-locked laser. If the fast saturation of the excitonic peak in the absorber plays a role in the devices, one would be able to observe a change in the passively mode-locked laser's operation. Measurements were carried out, and these demonstrated that broad tunability was possible with a grating placed within the cavity. A tuning range of 26 nm was demonstrated [19]. The behavior of the laser changes somewhat over the tuning range but not significantly. Further experiments were done, combining the tunability with pulse compression. These conclusively showed that the excitonic peak was not playing a strong role in our passively mode-locked lasers [20].

3.5 The tunable subpicosecond semiconductor laser

The usefulness of a mode-locked laser is limited in many applications by its inability to produce an output centered at a desired wavelength. It has previously been demonstrated that a semiconductor laser coupled to an external cavity and followed by an external grating compressor can be used to generate stable pulse trains of subpicosecond pulse widths [21]-[24]. Before this experiment, wavelength tunable mode-locked semiconductor lasers had been limited to pulse widths longer than a picosecond [19]-[27]. By taking advantage of the strong nonlinear saturation effects in passively mode-locked semiconductor lasers, one can produce pulses in the femtosecond regime from a broadly tunable semiconductor source. In this section, we present results combining broad-band wavelength tunability and subpicosecond pulse generation to create a tunable subpicosecond passively mode-locked semiconductor source.

The laser device and setup are described in [19] and [20]. Here a grating (600 lines/mm) is used to form one end of the external cavity while the laser's high reflection coated (90%) absorber facet serves as the other end of the external cavity (Fig. 3.10). The gain section is biased with a DC current source, and the absorber section is grounded for passively mode-locked operation. The light exiting the absorber is then compressed to subpicosecond pulse widths using a dual grating compressor as shown in Fig. 3.10. A high speed detector and microwave spectrum analyzer are used to monitor that the laser remains in the first harmonic of the external cavity which

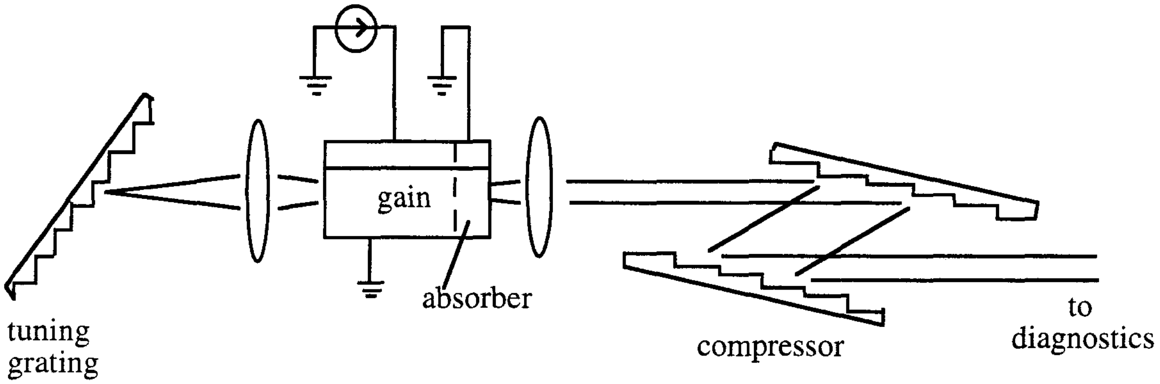

Figure 3.10: Wavelength tunable two-section laser passively mode-locked in external cavity with external grating pair compressor.

gives a repetition rate of 603 MHz [20]. Throughout the experiment, the laser mount is maintained at 21°C ± 0.5°C.

By rotating the grating to select the wavelength of maximum feedback into the laser, the center wavelength of the optical spectrum can be tuned from 838 nm to 854 nm, a range of 16 nm. The mode-locking threshold for first harmonic operation over this range is shown in Fig. 3.11. The operating points above this threshold, where measurements were performed, are shown as squares. For each of these wavelengths, the grating compressor is adjusted to minimize the compressed pulse width.

Using the second harmonic collinear intensity autocorrelator, pulse widths were measured at the indicated operating points (Fig. 3.11). The measured intensity autocorrelations are shown in Fig. 3.12, and the corresponding deconvolved pulse widths

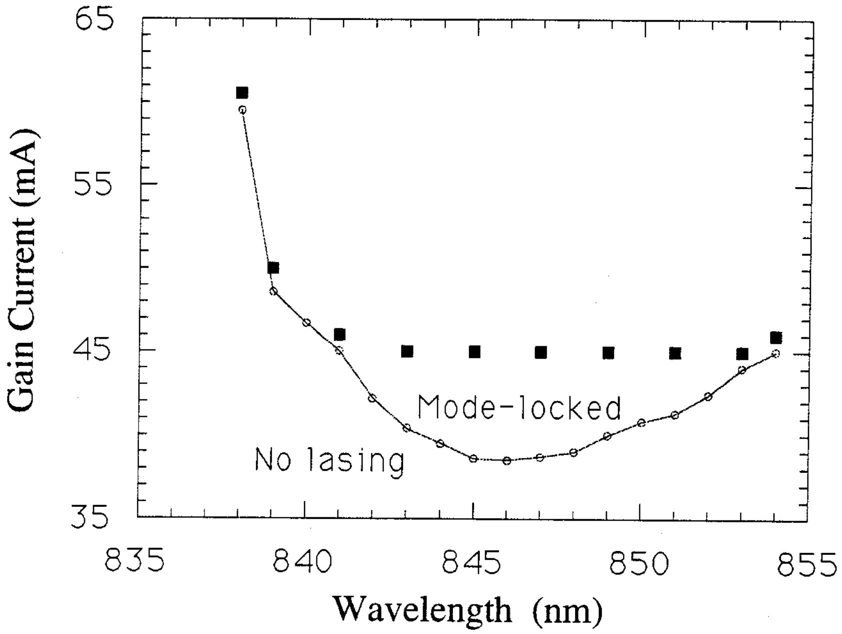

Figure 3.11: Mode-locking range (solid line) as a function of gain current and wavelength. Conditions at which autocorrelations and optical spectra are measured are indicated by squares.

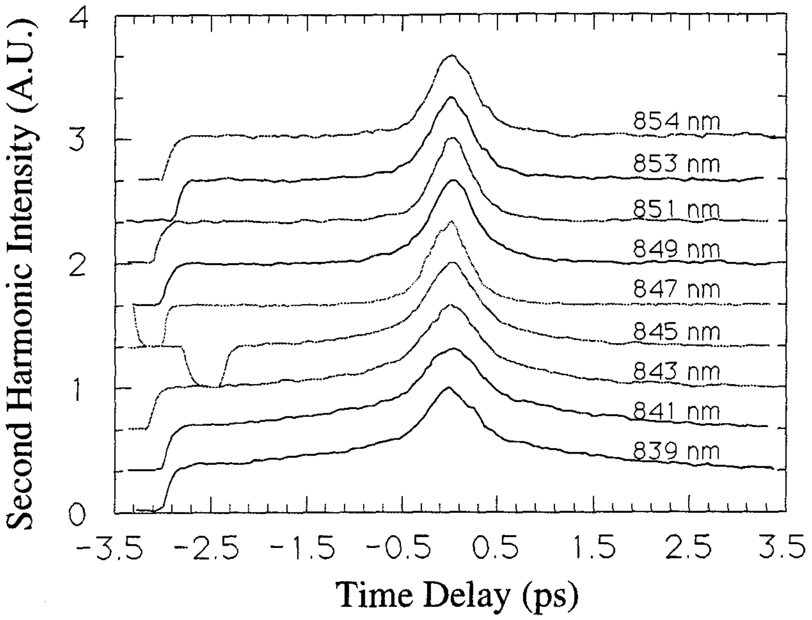

Figure 3.12: Intensity autocorrelations at indicated wavelengths.

(assuming a $sech^2$ profile) are shown in Fig. 3.13. The shortest pulses are obtained for wavelengths near the center and toward the longer wavelengths of the tuning range. Tuning toward the shorter wavelengths resulted in broader, yet still subpicosecond pulse widths with long tails. These long tails could not be eliminated by changing the compressor grating spacing, and the origin of these tails will be a topic of the following chapter. Generally, the chirp on the pulses exiting the cavity is extremely linear, allowing compression by a factor of ten or more, whereas the long tails are only visible after most of the linear chirp is removed. The pulses exiting the laser possess an up-chirp, meaning the frequency increases within each pulse, and the magnitude of chirp is typically on the order of 0.6 ps/nm. Measured pulse widths before compression are between 2 and 5 ps with the shorter uncompressed pulses occurring when

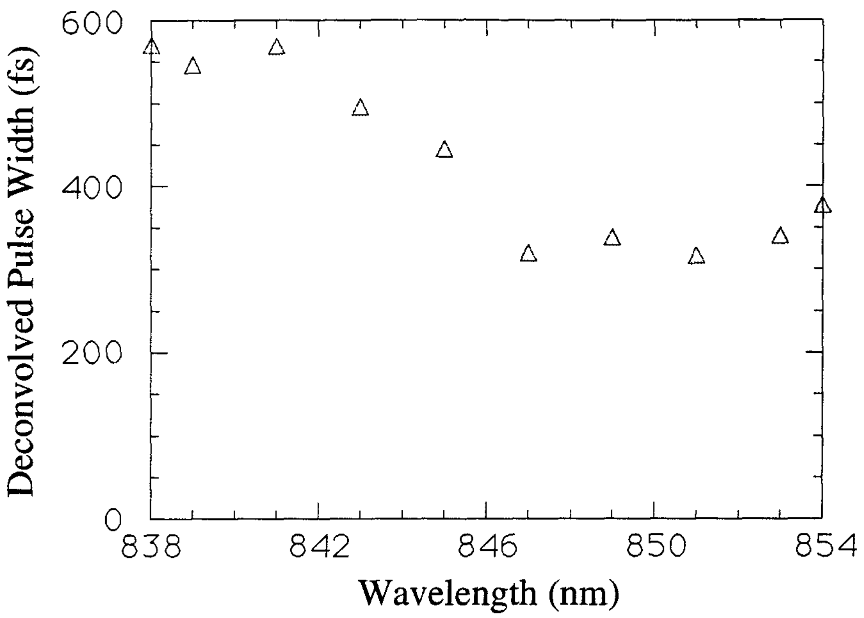

Figure 3.13: Deconvolved pulse FWHM versus wavelength.

tuning to shorter wavelengths. However, these shorter wavelength pulses possess the highest peak powers within the cavity, have the least linear chirp, and result in the longest pulses after compression. Increasing the current at shorter wavelengths does not reduce the pulse width considerably.

The shape of the optical spectrum under mode-locked operation is found to vary upon tuning. When tuning to shorter wavelengths, the spectrum is nearly symmetric, while for longer wavelengths it develops a much sharper drop on the long wavelength side (Fig. 3.14). A comparison of the measurements at three different operating points within the tuning range is shown in Table 3.2. Typical pulses are around 400 fs FWHM and have time bandwidth products between 1 and 2 times the transform limit. Measured peak powers were small (typically 50 mW) due to the 90% reflection

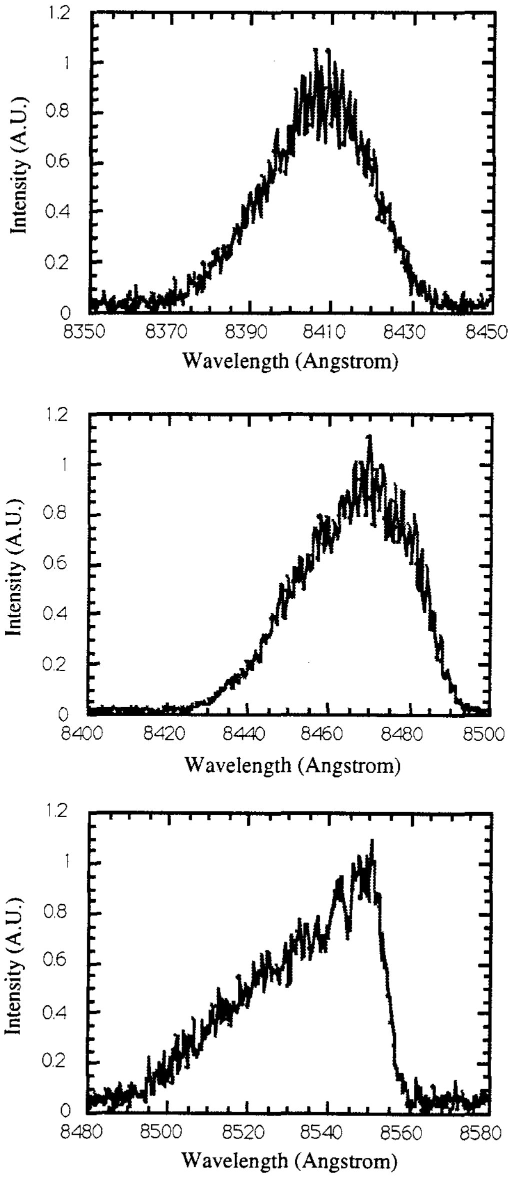

Figure 3.14: Mode-locked spectra shown for three different cavity tunings.

λ (nm)	I_{th} (mA)	I_{meas} (mA)	τ_w (fs)	$\Delta\lambda$ (nm)	$\tau_w \Delta\nu$	Average Power (μW)	Peak Power (mW)
839	48.8	50.0	550	3.0	0.69	36	38
847	38.5	45.0	320	3.3	0.44	37	67
853	43.4	45.0	370	3.6	0.50	24	38

Table 3.2: Comparison of measurements at three different wavelengths from the subpicosecond semiconductor laser.

at the output facet, and the 65% loss in the compressor.

A minimum pulse width, τ_w, of 260 fs is measured at a wavelength of 848 nm and a gain current of 53 mA with the laser modelocked in the first harmonic. The higher current and cavity tuning result in an optical spectrum FWHM of 6.0 nm, significantly broader than the spectra at lower currents (Table 3.2). The autocorrelation is shown in Fig. 3.15. The pulse peak power is found to be just over 100 mW. The calculated time-bandwidth product gives 0.65 (about 1.5 times transform limit). Due to the relatively high AR coating ($\sim$ 5%) on the gain facet, satellite pulses are measured with a combined energy of 9.6 ± 1%. Stronger gain pumping results in faster gain recovery times and can be sufficient to permit gain recovery to occur in less than 1/2 or 1/3 or even a smaller fraction of the round trip time. In this case, multiple equi-

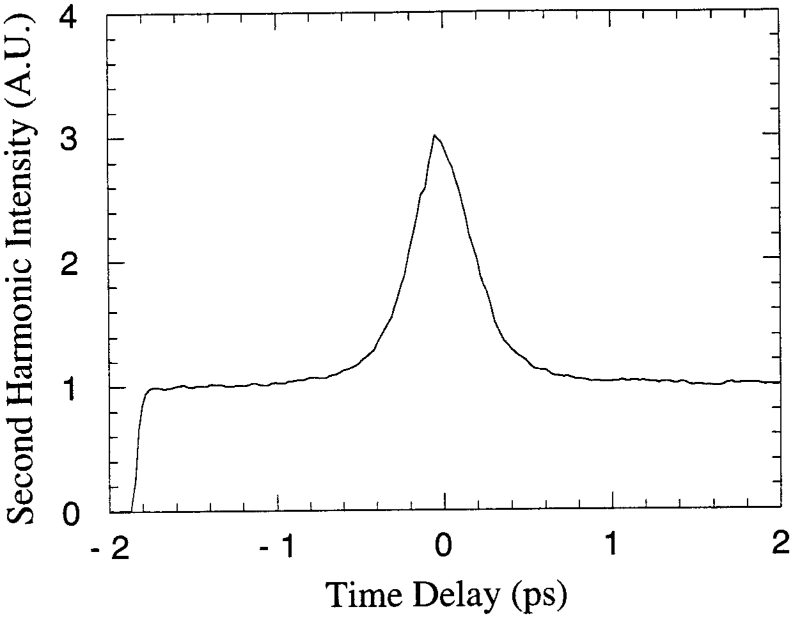

Figure 3.15: Minimum pulse width autocorrelation for gain current of 53 mA tuned to 848 nm.

spaced pulses can exist in the cavity, and the laser can modelock at higher harmonics of its fundamental round-trip frequency. Wavelength tuning of mode-locked second and third harmonic subpicosecond pulses in these lasers is observed, however, higher harmonic operation results in longer compressed pulses when achieved at similar current levels.

In conclusion, broad-band wavelength tunability (16 nm) with subpicosecond pulses was demonstrated for an external cavity mode-locked semiconductor laser. Pulse widths below 600 fs after external compression with a grating pair were generated giving a minimum pulse width of 260 fs ($\tau_w \Delta\nu = 0.65$) when the laser was operating at higher currents. Pulses were 1 to 2 times transform limited with long tails in the autocorrelations at the short wavelength side of the tuning range.

3.6 Spectral width calculation and experimental limits

There are limits on the expected minimum pulse width and the maximum tuning range of all existing lasers. These limits are due to the fact that the gain and loss of all the elements within the laser are not equally effective at all frequencies. Some spectral dependence exists and is usually characterized by a material or, in the case of confined laser modes, a modal bandwidth. First we will consider how this limited bandwidth restricts the minimum pulse width, and later we will briefly consider its effects on the tuning range.

3.6.1 Gain bandwidth limitations and minimum width pulses

As is intuitively expected from explanations in chapter 2 and as will be described in more detail in chapter 6, stable mode-locked operation requires a certain minimum mode coupling to exist so that modes off of the gain peak will oscillate and remain phase locked to the central mode(s). Simple active mode-locking experiments confirm our expectations here since larger AC modulations have been seen to permit broader mode-locked spectra to be generated [27]. In passive modelocking, this direct control of mode coupling is not available, instead, the mode coupling is indirectly related to the average intensity within the cavity. This relationship arises because the mode coupling is a result of nonlinear material gain and loss effects that are induced by the optical pulse in the laser. Therefore, a minimum average photon intensity must be generated to satisfy the requirement that, say, a mode fifty modes away from the gain bandwidth maximum will experience a mode coupling strong enough to make up the difference between its modal loss and its reduced modal gain. This means that for a given nonlinear saturation, only a finite number of modes within the gain bandwidth can be modelocked. Furthermore, for a finite number of locked modes, only a certain strength of mode coupling due to nonlinear saturation can be realized. One *key* figure for comparison of passively mode-locked lasers is a consideration of what fraction of the gain bandwidth FWHM can be modelocked. In dye lasers, arguably the most successful of the ultrashort pulse lasers, the widest reported mode-locked spectrum was 16 nm [28] from a corresponding gain bandwidth in Rhodamine 6G of 55 nm FWHM [29], giving a fraction of 0.291. In semiconductor lasers, mode-locked optical bandwidths of 6.0 nm FWHM from an optimistically estimated gain bandwidth of 20-40 nm FWHM or a fractional bandwidth of 0.15 - 0.3 has been modelocked (at Caltech). In ultrashort pulse generation, high power dye lasers possess an advantage since subsequent nonlinear fiber techniques followed by gratings are easily used to compress pulses almost one order of magnitude further, however, it can be seen from this comparison that roughly the same fraction of the gain bandwidth is modelocked in both cases.

There have been a number of techniques used to determine the gain bandwidth of semiconductor lasers, most notably is the Hakki-Paoli technique [30]. This determines the gain spectral bandwidth and its shift through a measurement of the ripples in the spectrum from the below threshold Fabry-Perot modes. Most techniques, including the one above are meant for single section lasers, however, the laser structures we used for modelocking are two or three section lasers and have a good AR coating on one facet. To determine the gain spectrum of the lasers that we have successfully used in mode-locking experiments, a method similar to that presented in Petermann was used [31]. This method allows one to estimate the gain bandwidth after measurements of the amplified spontaneous emission spectrum are made from the laser device without external cavity.

Using the same quadruple quantum well lasers, we measured the amplified spontaneous emission (ASE) spectrum. The experimental setup used to determine the laser gain spectrum is shown in Fig. 3.16. The laser device is set up without external cavity feedback, the absorber section is grounded so that it is absorbing, and various currents (all below threshold for this setup) are injected into the gain section. The center of the ASE spectrum shifts to shorter wavelength as currents are increased. Measurements are summarized in Table 3.3, below. A shift of 13 nm occurs along with the 30 mA (150%) increase in current.

As expected the measured widths of the ASE spectra vary only slightly. The shifts, however, are noticeable (as shown in Fig. 3.17) and give some clues to the carrier density inside the quantum wells. The expected ASE spectrum for this structure can be calculated and through comparison to the measured ASE spectra, one can estimate the modal gain spectra for these different pumping levels.

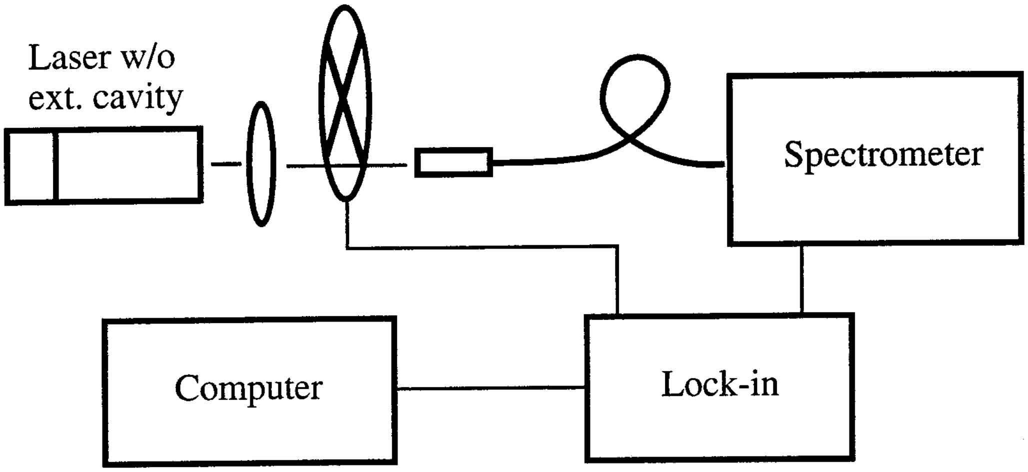

Figure 3.16: Experimental setup for ASE spectra measurements of devices. Setup uses chopper and lock-in amplifier for phase sensitive measurements with monochrometor.

Current	λ of peak	Half power points	FWHM
20 mA	832.0 nm	818.4, 844.4 nm	26.0 nm
30 mA	826.6 nm	813.3, 840.9 nm	27.6 nm
40 mA	823.5 nm	809.8, 838.8 nm	29.0 nm
50 mA	819.0 nm	807.5, 836.1 nm	28.6 nm

Table 3.3: ASE spectra measurements.

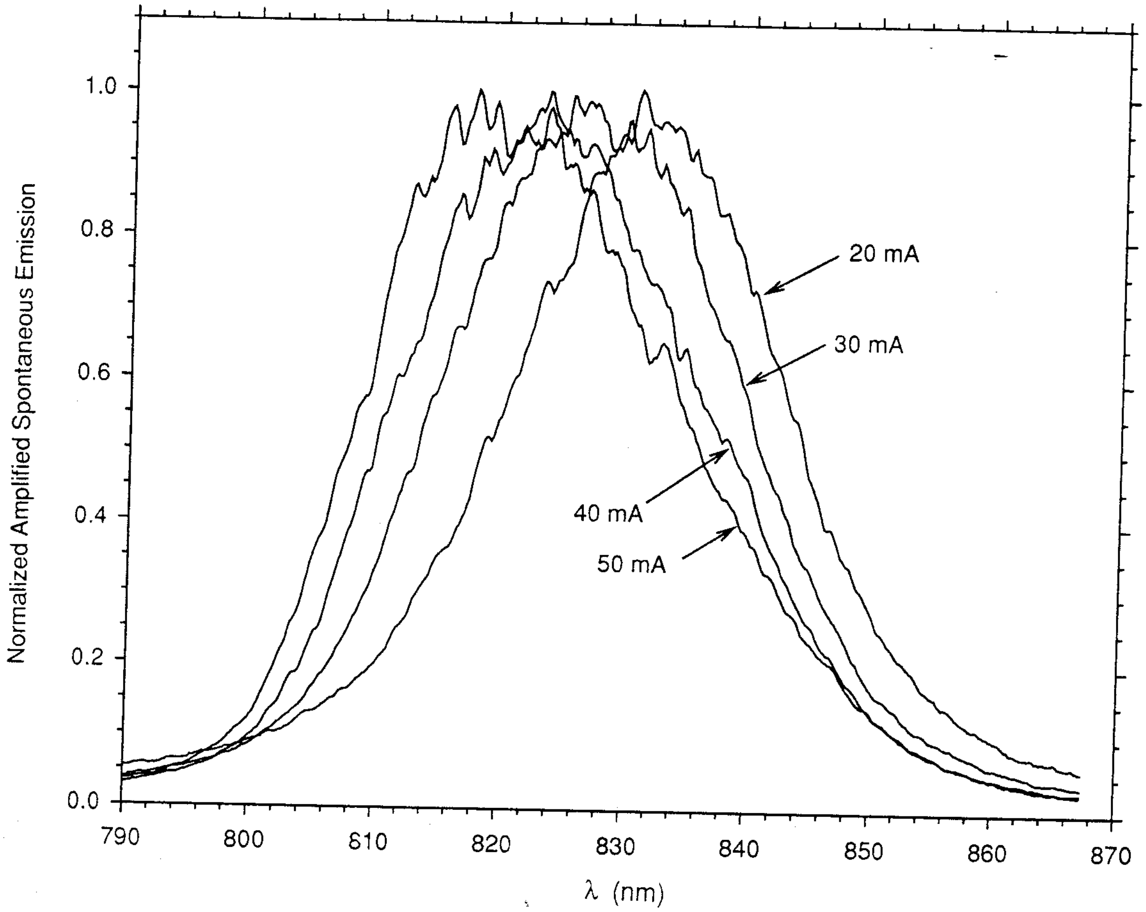

Figure 3.17: Measurement of ASE spectra for the LPE regrown quadruple well device.

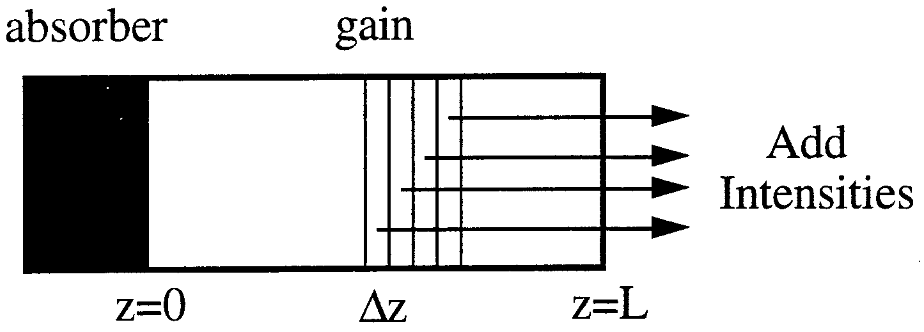

Figure 3.18: Model of device producing ASE while using no external cavity.

Theoretical model for ASE

Consider a device having a gain section of length, L, and an absorber at the left end which remains unsaturated (providing no reflected light). We assume reflection from the AR coated gain facet may be ignored. The propagation of the detected ASE light is as shown in Fig. 3.18. The gain spectrum can be determined,

$$g(\omega) = \frac{\pi\omega|\chi_{cv}|^2}{\epsilon_0 c n_{eff}} \int_{E_g}^{\infty} [f_c(n,E) - f_v(n,E)] \frac{\rho_{r,4QW}(E)\Gamma}{L_z} [\frac{\hbar/\pi T_2}{(E-\hbar\omega)^2 + (\hbar/T_2)^2}] dE. \quad (3.9)$$

Here, the quantities correspond to those defined in Yariv [32]. The spontaneous emission from each slice is proportional to,

$$R_{sp}(\omega) = \int_{E_g}^{\infty} f_c(n,E)[1 - f_v(n,E)]\rho_{r,4QW}(E)[\frac{1}{(E-\hbar\omega)^2 + (\hbar/T_2)^2}] dE. \quad (3.10)$$

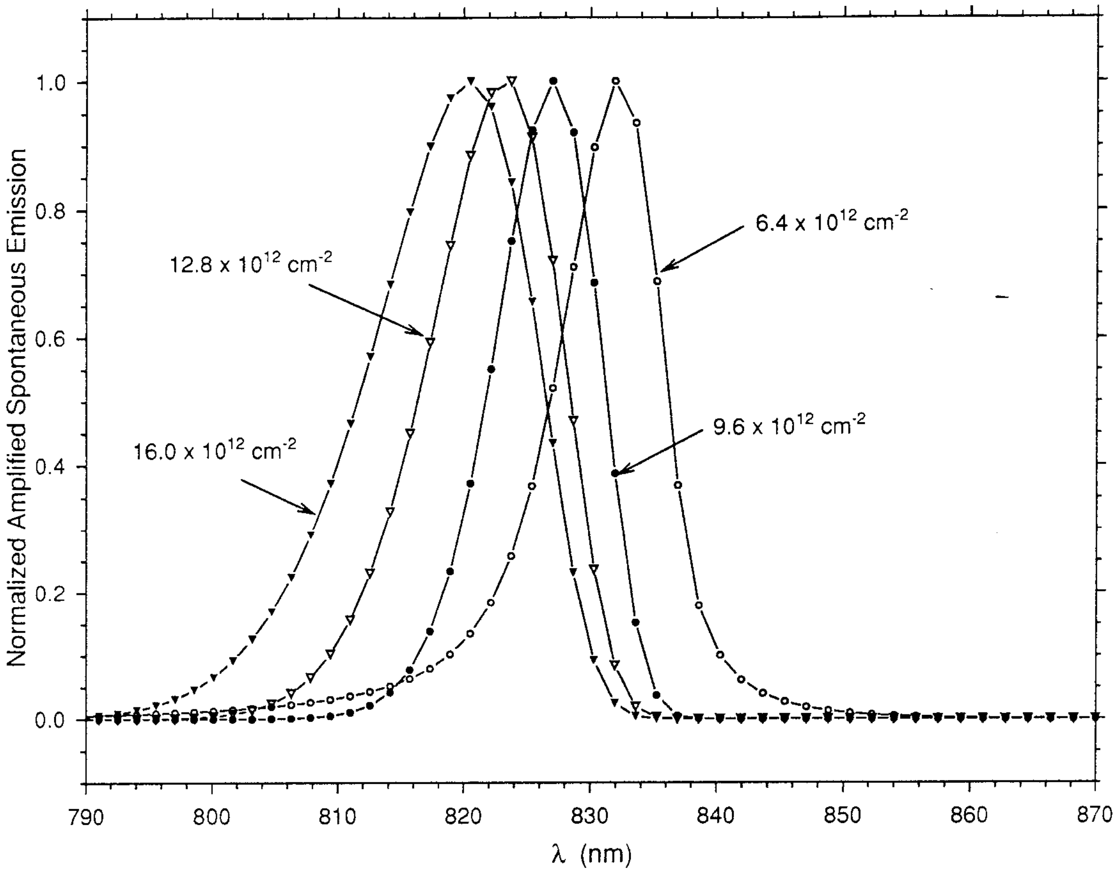

Figure 3.19: Calculated ASE spectra for the device structure and the noted carrier densities.

As physically displayed in the figure representing ASE generation (Fig. 3.18), the light exiting the gain facet is proportional to

$$ASE_{out}(\omega) = \frac{R_{sp}(\omega)(e^{g(\omega)L} - 1)}{g(\omega)}. \tag{3.11}$$

For material band gap, $E_g = 1.424$ eV, $L_z = 10$ nm, 4 quantum wells, $L = 500$ μm, $T_2 = 0.1$ ps, $\Gamma = 0.16$, $|\chi_{cv}|^2 = 6.6 \times 10^{-57}$ m-C, and the carrier densities shown on the graph, the ASE spectra and expected gain spectra are calculated. In Fig. 3.19, four ASE spectra that correspond closely to the measured ASE spectra are plotted. The calculated spectra are narrower than those measured which may mean the intraband relaxation time was underestimated, or more likely, the quantum wells are not ideally uniform as we had assumed in the calculation. The laser begins lasing at about 33 mA when it is aligned within the cavity and therefore, when lasing, is obviously clamped to a carrier density smaller than the cases of 40 mA and 50 mA pumping. The partial saturation of the isolation region and absorber and the non-zero Q near threshold in the experiment mean that the laser is likely limited to a carrier density below 30 mA during mode-locked operation. For this reason, the calculated gain spectra for 20 mA and 30 mA are plotted in Fig. 3.20. As shown, the long wavelength side of the gain spectrum does not move significantly with changes in carrier density, however, the short wavelength side rises considerably meaning that the gain spectrum broadens significantly with increased carrier density. Because of this, one could hope to be able to achieve a much broadened gain spectra through the use of single well lasers pumped to essentially four times the volumetric carrier density to achieve the same modal gain as one requires from a quadruple quantum well laser. The results for the quadruple quantum well laser are in agreement with the existence of a 20-40 nm gain bandwidth for the operating conditions of the passively mode-locked laser. A total two-dimensional threshold carrier density of 8×10^{12} cm^{-2} is calculated for the quadruple well laser operating with absorber grounded when coupled to an external cavity with the 70% mirror in place. One should also consider over what range the absorber is comparably effective to truly consider the possible mode-locked spectral width that can be achieved, but significant problems beyond "fine-tuning effects" are not expected to be a major problem here, and for the external cavity setup,

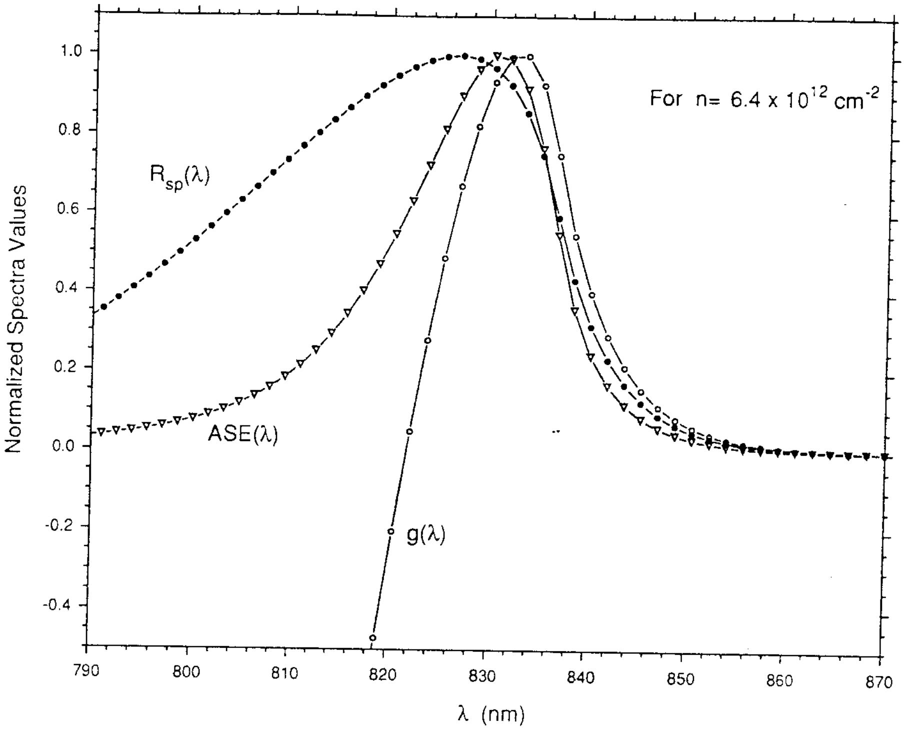

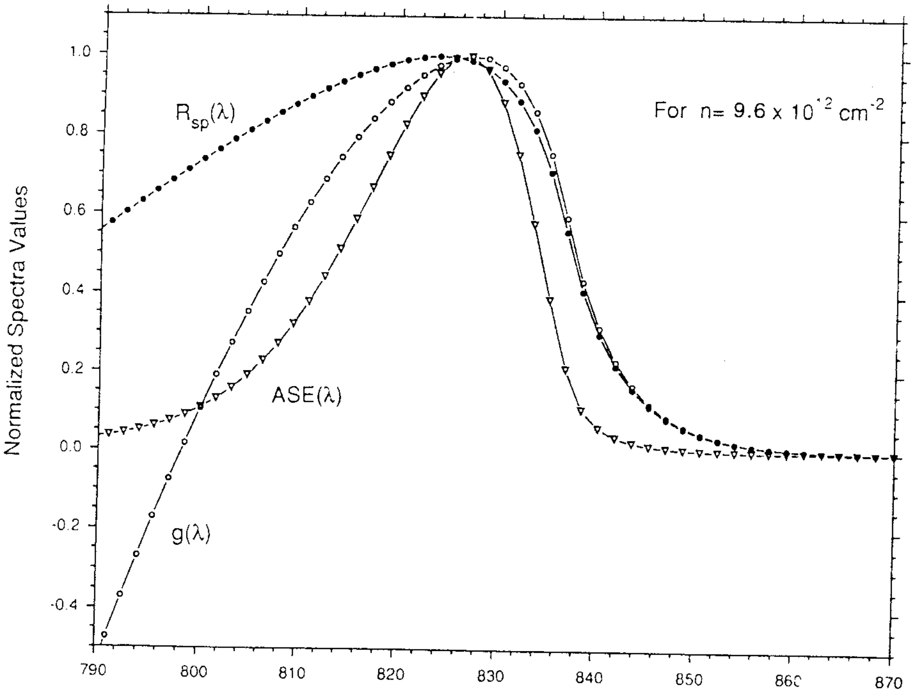

Figure 3.20: Calculated gain spectra for quadruple well devices for carrier densities that roughly correspond to 20 mA and 30 mA ASE operation.

approximately 30 nm FWHM gain spectral width is expected to be a reasonable estimate for these devices.

3.6.2 Tunability limits

The gain spectrum's finite width is considered to be the dominant limitation also on the mode-locked laser's tunability. As previously discussed, the tuning of the mode-locked laser was accomplished by rotating a 600 line/mm grating to change the compound cavity's peak gain. The filter response of the microscope objective and grating setup is calculated to produce essentially a Gaussian bandwidth of 67 nm FWHM. The center frequency of this spectrum is moved relative to the ~ 30 nm gain bandwidth of the device. As one moves the two filter center wavelengths apart, the net feedback is reduced. Separate measurements have been made with a variable attenuating beam splitter and have shown that, typically, a beam splitter power reflectivity of around 30% or more (*total power* coupling back from the external cavity setup was closer to 20% due to additional coupling losses) was required to maintain stable modelocking. Reflectivities below this had monolithic modelocking and/or self pulsations corrupting the pulse train.

The feedback grating was found to have a power reflectivity of approximately 70% into the +1 order. Pulling the spectrum about 15 nm off of the center of its tunability range decreases the effectiveness of the gain (which mostly may be made up for by raising the current) and reduces the strength of external cavity feedback by an additional 50% (assuming parabolic near-the-peak approximations for the filters).

This reduces the net feedback to 35%, a level comparable to the minimum required feedback for stable passive modelocking in this setup. Thus, the demonstration of 26 nm tuning from the 4 quantum well laser [19] is only slightly smaller than the $\sim$ 30 nm tuning range we would expect from the rough calculation. As with single well passively mode-locked lasers suggested for broader mode-locked spectra in the previous section, we would expect to achieve broader tunability from single well lasers also. This is one area in which we feel improved results could be obtained.

For comparison with other homogeneously broadened lasers, the broadest tunability which has been achieved with the Rhodamine 6G dye laser is 30 nm by Wittmann [33] for a gain spectrum with of 55 nm FWHM, giving a fractional tuning bandwidth of 0.54. The best results for the tunable passively mode-locked semiconductor laser are a 26 nm tuning range, and assuming a relatively strongly pumped gain section, a bandwidth $\sim$ 40 nm FWHM (as additional loss from a pellicle beam splitter was inserted into the cavity during this tunability measurement), gives a fractional tuning bandwidth of 0.65. So tunability for quadruple quantum well lasers, even in our generous estimate of the gain bandwidth FWHM, slightly exceeds the record tunability of other well-developed passively mode-locked systems in existence.

References

[1] E. P. Ippen, D. J. Eilenberger, and R. W. Dixon, *Appl. Phys. Lett.*, **37**, 267 (1980).

[2] S. Sanders, A. Yariv, J. Paslaski, J. E. Ungar, and H. A. Zarem, *Appl. Phys. Lett.*, **58**, 681 (1991).

[3] S. Sanders, *Ph.D. Thesis*, California Institute of Technology (1992).

[4] A. Yariv, **Optical Electronics**, 3rd ed., p. 173, Holt, Rinehart and Winston (1985).

[5] W. Dietel, J. J. Fontaine, and J. C. Diels, *Opt. Lett.*, **8**, 4 (1983).

[6] E. B. Treacy, *IEEE J. Quantum Electron.*, **5**, 454 (1969).

[7] O. E. Martinez, *IEEE J. Quantum Electron.*, **23**, 59 (1987).

[8] J. D. Kafka and T. Baer, *Opt. Lett.*, **12**, 401 (1987).

[9] H. G. Winful, *Appl. Phys. Lett.*, **46**, 527 (1985).

[10] A. Yariv, D. Fekete, and D. Pepper, *Opt. Lett.*, **4**, 52 (1979).

[11] N. Henmi, T. Saito, and T. Ishida, *J. Lightwave Technol.*, **12**, 1706 (1994).

[12] W. J. Tomlinson, R. H. Stolen, and C. V. Shank, *J. Opt. Soc. B*, **1**, 139 (1984).

[13] Y. Silberberg and P. W. Smith, *IEEE J. Quantum Electron.*, **22**, 759 (1986).

[14] T. Schrans, R. A. Salvatore, S. Sanders, A. Yariv, *Electron. Lett.*, **28**, 1480 (1992).

[15] P. W. Smith, Y. Silberberg, and D. A. B. Miller, *J. Opt. Soc. B*, **2**, 1228 (1985).

[16] H. A. Haus and Y. Silberberg, *J. Opt. Soc. B*, **2**, 1237 (1985).

[17] Y. Silberberg, P. W. Smith, D. A. B. Miller, B. Tell, A. C. Gossard, and W. Wiegmann, *J. Opt. Soc. B*, **16**, 701 (1985).

[18] W. H. Knox, R. L. Fork, M. C. Downer, D. A. B. Miller, D. S. Chemla, C. V. Shank, A. C. Gossard, and W. Weigmann, *Phys. Rev. Lett.*, **54**, 1306 (1985).

[19] T. Schrans, S. Sanders, and A. Yariv, *IEEE Photon. Technol. Lett.*, **4**, 323 (1992).

[20] R. A. Salvatore, T. Schrans, and A. Yariv, *IEEE Photon. Technol. Lett.*, **5**, 756 (1993).

[21] J. P. van der Ziel, W. T. Tsang, R. A. Logan, R. M. Mikulyak, and W. M. Augustyniak, *Appl. Phys. Lett.*, **39**, 525 (1981).

[22] P. J. Delfyett, L. Florez, N. Stoffel, T. Gmitter, N. Andreadakis, G. Alphonse, and W. Ceislik, *Opt. Lett.*, **17**, 670 (1992).

[23] R. J. Helkey, D. J. Derickson, A. Mar, J. G. Wasserbauer, J. E. Bowers, and R. L. Thornton, Conf. Lasers and Electro-Optics, 1992, **12**, OSA Tech. Dig. Series, p. 408, Optical Society of America, Washington D.C. (1992).

[24] N. Stelmakh and J. M. Lourtioz, *Electron. Lett.*, **29**, 160 (1993).

[25] M. C. Wu, Y. K. Chen, T. Tanbun-Ek, R. A. Logan, and M. A. Chin, *IEEE Photon. Technol. Lett.*, **3**, 874 (1991).

[26] J. M. Wiesenfeld, M. Kuznetsov, and A. S. Hou, *IEEE Photon. Technol. Lett.*, **2**, 319 (1990).

[27] M. Serenyi, J. Kuhl, and E. O. Gobel, *Appl. Phys. Lett.*, **50**, 1213 (1987).

[28] W. H. Knox, R. L. Fork, M. C. Downer, R. H. Stolen, C. V. Shank, and J. A. Valdmanis, *Appl. Phys. Lett.*, **46**, 1120 (1985).

[29] T. F. Johnston, *Tunable Dye Lasers*, **Encyclopedia of Physical Science and Technology**, **14**, edited by R. A. Meyers, pp. 96-141, Academic Press, Orlando (1987).

[30] B. W. Hakki and T. L. Paoli, *J. Appl. Phys.*, **46**, 1299 (1975).

[31] K. Petermann, **Laser Diode Modulation and Noise**, ch. 3, Kluwer Academic Publishers, Boston (1991).

[32] A. Yariv, **Quantum Electronics**, 3rd ed., ch. 12, Wiley, New York (1989).

[33] M. Wittmann, A. Penskofer, and W. Baumler, *Opt. Commun.*, **90**, 182 (1992).

Chapter 4

Characterizing ultrashort pulses from semiconductor lasers

Although the results of the previous chapter qualitatively agree quite well with expectations, there are many details that should experimentally be examined further if one wants to better understand the ultrashort pulses from these lasers. Perhaps most troublesome is the question: "Why do the pulses from the broadly tunable subpicosecond laser show long tails in their autocorrelations when the laser is tuned to shorter wavelength?" This is completely beyond explanation if one makes the common assumption that the pulses are a simple shape like a Gaussian or hyperbolic secant. New techniques have been found to, for the first time, gather the necessary detailed information for accurate analysis of the ultrashort semiconductor laser pulses. A second question one notes is: "Why is there an excess time-bandwidth product for these lasers and is it explained by the fact that the spectrum is only locked in clusters of modes?" Evidence that the spectrum is fully locked will be presented in the last section of this chapter. The next section will deal with preliminary information and the question of the long tails in the autocorrelation.

4.1 Amplitudes, phases, and long autocorrelation tails

In the generation of ultrashort pulses, a knowledge of the complex pulse envelope, i.e., both amplitude and phase behavior, of the pulses exiting the laser is a key to achieving optimally short pulses. As early as 1980, passively mode-locked semiconductor lasers were known to generate picosecond, although not time bandwidth limited, optical pulses. In 1985, it was first concluded that the excess time-bandwidth product of these typical picosecond pulses was due to an up-chirp (an increasing optical frequency during each pulse) [1]. Often the chirp is extremely linear and thus easily compensated by a dual-grating pulse compressor, allowing generation of < 300 fs pulses [2]-[4]. Under other conditions, when tuned to different wavelengths or biased differently, the laser does not produce such a linear chirp. We describe general trends of the passively mode-locked laser's pulse shape and chirp as the laser's spectrum is tuned to different wavelengths in the tuning range.

Standard autocorrelation measurements preclude extraction of information concerning the pulse shape and chirp. Most techniques for measuring pulse shape or chirp require algorithmic methods involving interferometric field autocorrelations [5] or are

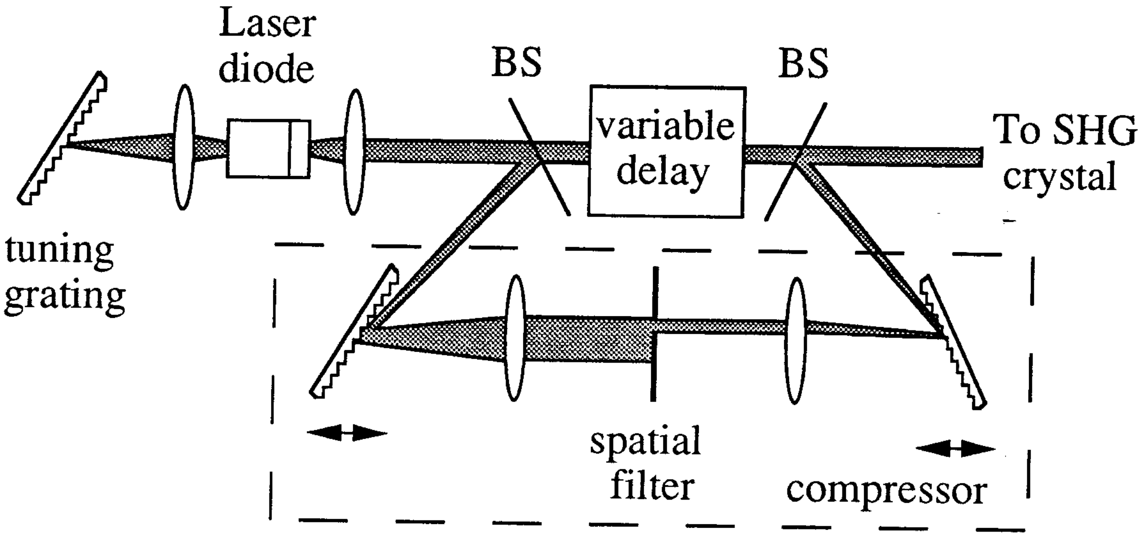

Figure 4.1: Setup of cross-correlation system for measurement of intensity envelope of pulses. A spatial filter with adjustable position is used in the Fourier plane for spectral filtering in chirp measurements only.

useful only for higher energy pulses (1 nJ or more), such as the FROG technique [6]. In this paper, we use a direct measurement of pulse shape and a direct measurement of the chirp similar to that used by Chilla for dye lasers [7]. It is demonstrated for the first time, that for passively mode-locked semiconductor lasers, the asymmetric pulse shape, linear chirp and second order chirp can be measured using cross-correlation and filtering techniques.

In order to measure the pulse shape, a setup as shown in Fig. 4.1 was used. The laser is a quadruple quantum well, two-section, GaAs buried heterostructure as described previously [8]. Because the pulses coming directly from the laser are naturally stretched out, and can easily be compressed by at least an order of magnitude, we split off part of the beam, sending it into a dual-grating compressor (without spatial filter), thus making it effectively a delta function. Next the two beams are collinearly recombined and sent into a second harmonic generation (SHG) crystal, and their temporal cross-correlation is measured. The resulting cross-correlation will thus be the shape of the intensity envelope of the original pulse exiting the laser.

The results of the measurement are shown in Fig. 4.2. The asymmetry of the pulses is readily visible. To quantify this, the 10% to 90% rise time and fall time of the pulse intensity are measured. When the laser is tuned near the center or longer wavelengths of the tuning range (838 nm to 854 nm) [3], the ratio of the fall time to rise time is about 2.3 to 1 (Fig. 4.2). The pulse shape for the laser tuned to the shorter wavelength side of the tuning range is shown (for 841 nm center wavelength) in Fig. 4.2 (bottom). In this case, a more sharply peaked pulse is measured, yet with tails extending slightly further. Here, again, the fall time to rise time ratio was similarly found to be 2.0 to 1.

The asymmetry in the resulting pulse shapes is explained by the fact that in the passively mode-locked laser, both the rising and falling edges are shaped by different physical phenomena. The rising or front edge of the pulse is shaped by the loss of the absorber section until it is saturated, while the falling edge of the pulse is shaped as the gain section undergoes enough saturation to again present a net loss [9]. The absorber has a relatively large (in magnitude) differential absorption, $A = -d\alpha/dn_a$, which means each photon absorbed reduces the absorption rather effectively. This helps provide a relatively fast saturation process. The saturation rate is, from the

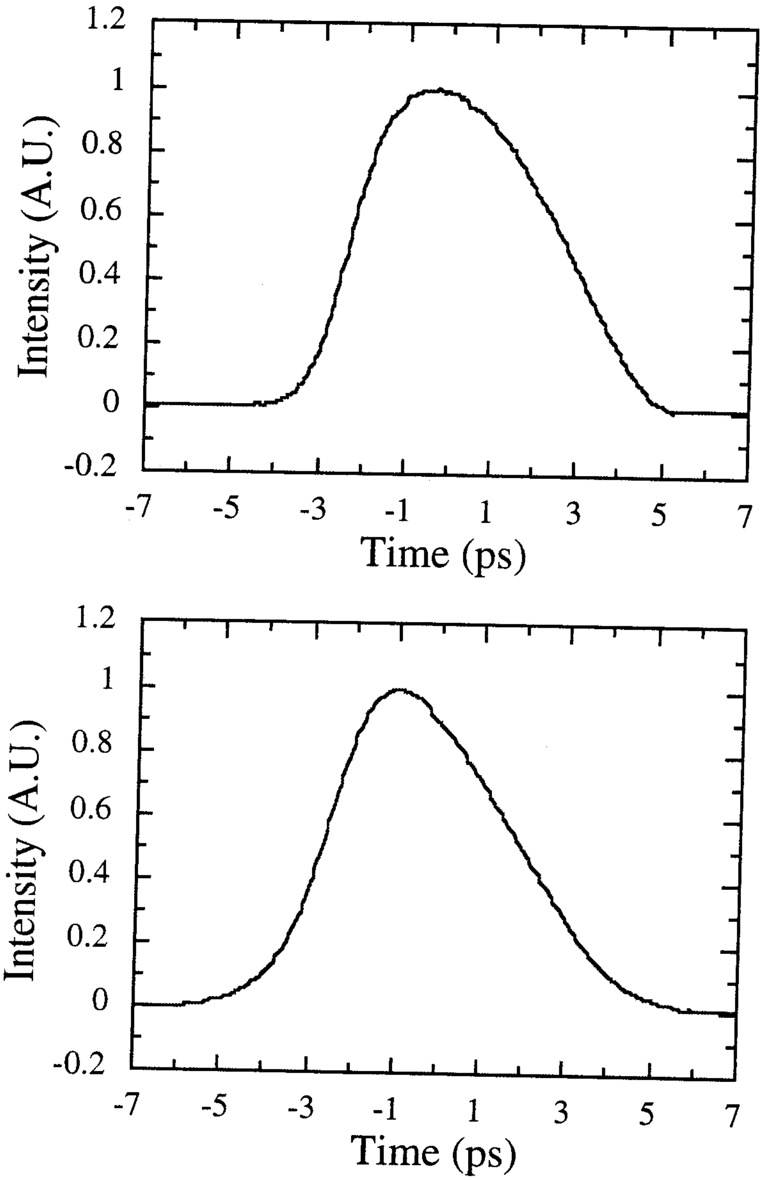

Figure 4.2: Measured shape of pulse exiting the semiconductor laser for spectrum center tuned to 848 nm (top) and 841 nm (bottom).

carrier rate equation [similar to (2.2)], given by

$$\frac{dn_a(t)}{dt} = -\Gamma A n_a(t) S(t), \tag{4.1}$$

where $n_a(t)$ is the density of carriers contributing to absorption, Γ is the confinement factor, and $S(t)$ is the photon intensity.

On the other hand, since typically differential gain saturates with higher population, the differential gain, $G = dg/dn_g$, is smaller by about a factor of 2, resulting in a larger saturation energy and a slower saturation rate,

$$\frac{dn_g(t)}{dt} = -\Gamma G n_g(t) S(t), \tag{4.2}$$

where $n_g(t)$ is the density of carriers contributing to gain. The gain section's slower saturation rate can account for the slower shaping at the fall-off of the optical pulses. To double check the pulse shape results, we have numerically generated an autocorrelation of a pulse from Fig. 4.2 and compared the result to the actual measured autocorrelation taken under the same conditions. The two resulting plots match very well indicating that the compressed pulse is close enough to a delta function and does not introduce significant broadening.

The setup for measuring the spectral phase is identical to the setup for measuring the pulse shape (Fig. 4.1), except now a single slit spatial filter is added in the Fourier plane between the two lenses of the dual grating compressor to pass a narrow "slice" of the spectrum [10]. The full field spectrum may be described as $F(\omega)e^{-j\tau_n(\omega-\omega_0)}$, where $F(\omega)$ represents the magnitude of the spectrum, w_0 is the spectrum's center frequency, and τ_n is the delay for slice "n" and can vary across the spectrum, accounting for any spectral phase. Upon filtering, a slice of the spectrum having center frequency ω_f and filter width $\Delta\omega_f$ (assuming a Gaussian filter for simplicity) is then

$$F(\omega)e^{-j\tau_n(\omega-\omega_0)}e^{\frac{-(\omega-\omega_f)^2}{(\Delta\omega_f)^2}}. \tag{4.3}$$

Taking the transform of this expression (to within a constant), one can see that τ_n exactly represents the group delay of the pulse from any narrow slice of the spectrum,

$$[f(t-\tau_n) * e^{\frac{-(\Delta\omega_f)^2(t-\tau_n)^2}{4}}]e^{j\omega_f t}. \tag{4.4}$$

If τ_n is a nonzero constant throughout the spectrum, this adds a uniform time delay to the pulse as seen from the above convolution. If τ_n varies linearly or quadratically with n, a broadening or asymmetry of the pulse results, respectively.

Using this setup, and choosing any slice of the spectrum, the corresponding time delay for the slice's center wavelength can be measured. By measuring the peak's position in the cross-correlation, the group delay, τ_n, can be determined for different wavelengths, thus the sign and magnitude of the chirp can be measured. For even more accuracy in measuring the nonlinear chirp, both beams are sent through the compressor (using cylindrical lenses to keep the beams distinct) delaying one and filtering the other, and using the proper grating spacing to remove the linear part of τ vs. λ.

The directly measured curves for the cross-correlation delay vs. slice center wavelength are plotted in Fig. 4.3 using 1.2 nm slices. The chirp in Fig. 4.3 (top) is extremely linear, meaning that it would be ideal for compensation from a dual grating pulse compressor. Results from pulse compression confirm this, as this is the

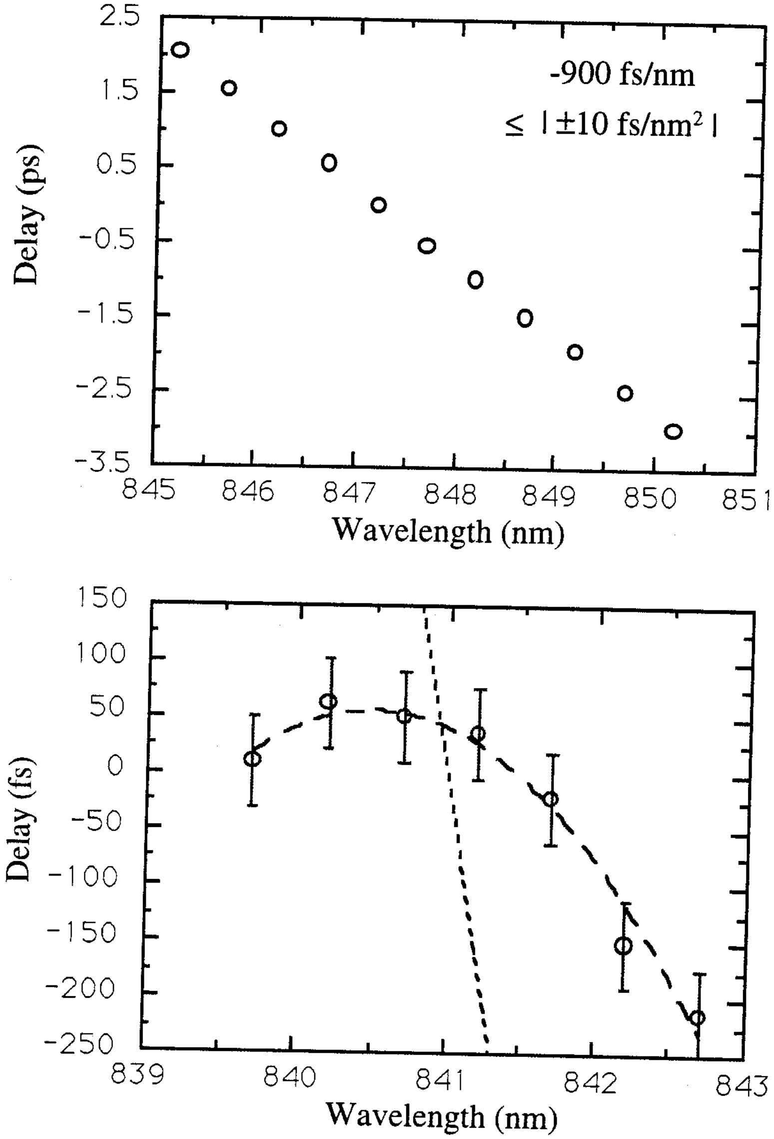

Figure 4.3: (top) Measurement of chirp in terms of group delay vs. rectangular filter's center wavelength giving -900 fs/nm and ± 10 fs/nm^2 for laser tuned to 848 nm and (bottom) for laser tuned to 841 nm, nonlinear chirp (dashed curve) of -60 fs/nm^2. Linear chirp shown for comparison (dotted line) -800 fs/nm.

case where a minimum compressed near-transform-limited pulse width of 260 fs is achieved [3]. Even when both beams are phase compensated by sending each though the compressor, eliminating the linear chirp, no nonlinear chirp can be detected. Only a linear chirp of -900 fs/nm is measured. Resolution for the measurement of nonlinear chirp is estimated to be no more than ±10 fs/nm^2. The dual grating compressor is expected to add a negligible nonlinear chirp of 5 fs/nm^2.

The chirp resulting from the laser when tuned to the shorter wavelength side of the tuning range (841 nm) has a significant nonlinear component. The τ vs. λ curve shows a steeper slope at the long wavelength side of the spectrum. The linear chirp was measured to be slightly smaller in magnitude, -800 fs/nm. More accurately measuring the nonlinear chirp by removing most of this linear chirp, as described previously, gives a nonlinear chirp of -60 fs/nm^2 ± 10 fs/nm^2. Higher order terms in the nonlinear chirp are not found to be present. The external cavity grating which is rotated for tuning is known to add no dispersion by itself and may only add dispersion due to lens aberrations which are considered negligible here, therefore the nonlinear chirp results from the semiconductor laser itself. The same long-tailed autocorrelations will result from the laser when the feedback from an external cavity mirror (used in place of the grating) is reduced. Thus, the long tails and nonlinear chirp do not seem to be an inherent result of the tuning but a result of larger self phase modulation (SPM) nonlinearities induced through the deeper cycling of the gain section. In these measurements at about 1 mW average optical power and 600 MHz pulse repetition, smaller time-bandwidth products and slightly less linear chirp (in terms of $d\tau/d\lambda$) are obtained from lower Q cavities even though higher peak powers and more nonlinear chirp are present.

As is known from studies of semiconductor laser amplifiers, the linewidth enhancement factor $\alpha(w, n_g)$ which couples amplitude to phase, will cause a frequency chirp across the pulse [11]. The effect of the changing index over some length of gain material is not unlike the effect one would expect from a Doppler redshift as the optical path length is increased. Assuming a relationship between the gain and the change in index, $n(t) = \alpha(n_g(t), w)g(t)$, the phase shift upon travelling through a length L_g of laser material is:

$$\phi(t) = \omega t - k_0 L_g (n_0 + \frac{dn(t)}{dt} t), \tag{4.5}$$

and using (2), the SPM frequency shift is found to be approximately:

$$\Delta\omega(t) = -k_0 \alpha(\omega, n_g(t)) \Gamma^2 G^2 n_g(t) L_g P(t). \tag{4.6}$$

In our measurements, the SPM, in terms of the magnitude of $d\tau/d\lambda$, from the gain section significantly dominates the equivalent term that results from the absorber section. A plot of the changes in gain carrier density and expected frequency shift during the pulse is shown in Fig. 4.4. The half-way saturation of $n_g(t)$, and even more so, the peak frequency shift is expected to occur before the pulse reaches its peak intensity. The upward concavity in a plot of $\omega(t)$ near the pulse's peak is consistent with the measured sign of nonlinear chirp. Although a self-consistent solution with these large nonlinearities must be found to conclusively explain the extremely linear chirp, it is likely that during the peak of the pulse, a rather linear up-chirp occurs

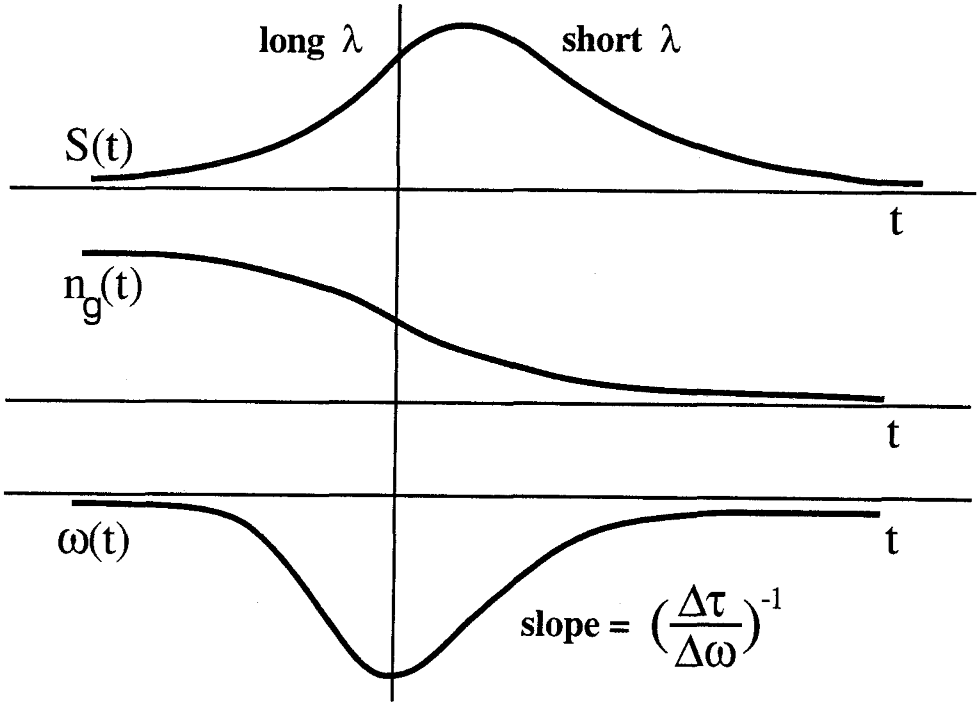

Figure 4.4: The change in pulse intensity plotted along with the change in carrier density it induces and the change in instantaneous frequence it induces.

[12].

To verify and extract further information, the pulse and compression system have been simulated numerically. Using the pulse shape measurements and estimated linear and quadratic chirp and requiring the resulting spectrum to match the measured spectrum well, the resulting uncompressed and compressed pulse autocorrelations are calculated and found to be in good agreement with the measurements. In Fig. 4.5 (top), the solid line is the measured autocorrelation for the compressed pulse for the laser tuned to 848 nm, and a simulation with -800 fs/nm and -15 fs/nm^2 gives an autocorrelation that matches very well (indiscernible on the plot). The dotted line represents, according to the simulation, the actual pulse intensity envelope we would expect to measure for the compressed pulse.

Fig. 4.5 (bottom) shows the corresponding simulation for the laser operating at 841 nm. Again the solid line represents the measured autocorrelation for the compressed pulse. The dashed line is the simulation and matches the long tails very well with -700 fs/nm and -70 fs/nm^2 chosen for the pulse in this case. Also, the expected envelope of the compressed pulse is displayed by the dotted line. The nonlinear chirp can adequately explain the long tails remaining after pulse compression. From the measured sign of the nonlinear chirp, it is expected that small lobes precede the actual compressed subpicosecond pulses in time.

In conclusion, the shape of pulses exiting the mode-locked semiconductor laser is directly measured and its asymmetry is attributed to the slower saturation rate of the gain section compared to the absorber section. Linear and nonlinear chirp

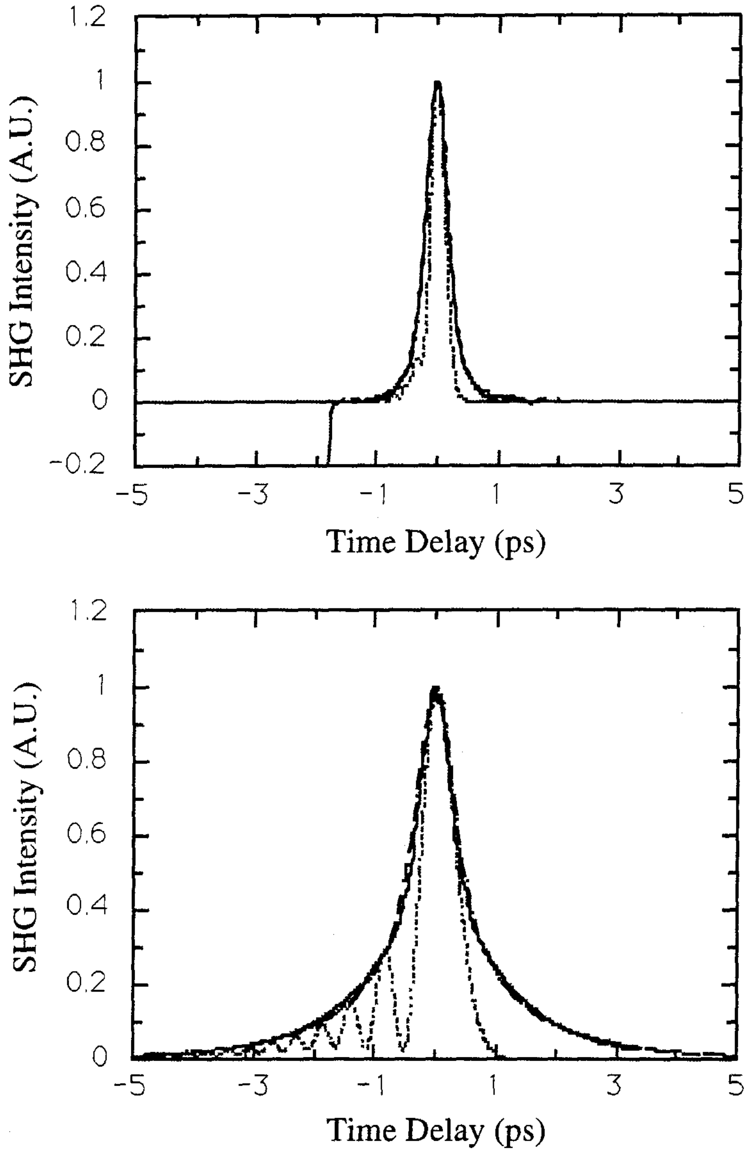

Figure 4.5: For laser tuned to 848 nm (top) and 841 nm (bottom), a fit of calculated (dashed line) to measured autocorrelation of compressed pulse (solid line) and the calculated compressed pulse intensity resulting from the fit (dotted line). Fit shows that nonlinear chirp is mainly quadratic.

is measured for various center wavelengths. The nonlinear chirp is associated with reduced external cavity feedback which has been known to force deeper cycling of the gain section, and by shifting the linear segment of the SPM away from the pulse center, results in a significant nonlinear chirp which is seen to leave large tails limiting the minimum pulse width of the dual-grating-compressed pulse.

4.2 Modelocking across entire spectrum

Past experiments with mode-locked semiconductor lasers have shown evidence that modelocking has involved separate clusters of locked modes oscillating independently [13]. There have even been suggestions that the sometimes seen self pulsations are a result of beating between different clusters of modes [14]. Therefore, it is important to be careful in experimentally testing the spectrum's coherence before we assume the ideal case, that it is modelocked across the full spectrum. The measurements in the previous section require a fully mode-locked spectrum.

There are a few ways to test this fully locked condition. Firstly, one can think of selecting a slice of certain width from the optical spectrum. This may be done with the single slit filter mentioned previously. Assuming the spectrum to be relatively free of phase terms cubic or higher, which we expect to be the case from measurements presented previously, one expects to measure the same autocorrelation width independent of where the filter is centered. On the contrary, if one has a spectrum that is not fully locked, there will be ranges within the spectrum where the filter can be placed and a broadened autocorrelation would be obtained since the spectrum within the slice would have a smaller than optimal time-bandwidth product. These measurements were carried out using a rectangular filter width of 1 nm and systematically taking autocorrelation widths for different filter center wavelengths. The results of this measurement showed autocorrelation widths all equal within our experimental accuracy.

One would also suspect that if the spectrum were not fully locked across its full range, then cutting off one tail would lead to no significant change in pulse width. One can carry this idea further and measure autocorrelations from a certain rectangular filter center wavelength and only change the spectral slice width. The results can be compared with what is expected. A plot for the mode-locked laser spectrum is shown in Fig. 4.6, and a rectangular filtered slice is shown for a specific case. Since the spectrum is essentially the shape of a single sawtooth, one may assume a fully mode-locked spectrum of this shape and carry out the operation $\mathcal{F}^{-1}[|\mathcal{F}(|\mathcal{F}^{-1}[E(\omega)F(\omega)]|^2)|^2]$ to obtain the temporal autocorrelation, where $E(\omega)$ is the optical spectrum, $F(\omega)$ is the transfer function for the rectangular filter, and $\mathcal{F}$ and $\mathcal{F}^{-1}$ represent the Fourier transform and inverse Fourier transform operations, respectively.

We note that more narrowly slit filtering a strongly chirped spectrum causes an initial narrowing of the pulse width (dubbed the "poor man's compressor" by Dr. Yariv) and later a sudden broadening as the time-bandwidth limit is approached. An unchirped triangle optical power spectrum gives a time-bandwidth product of 0.50 and an autocorrelation that is 1.37 times the pulse FWHM. Results of the measurement

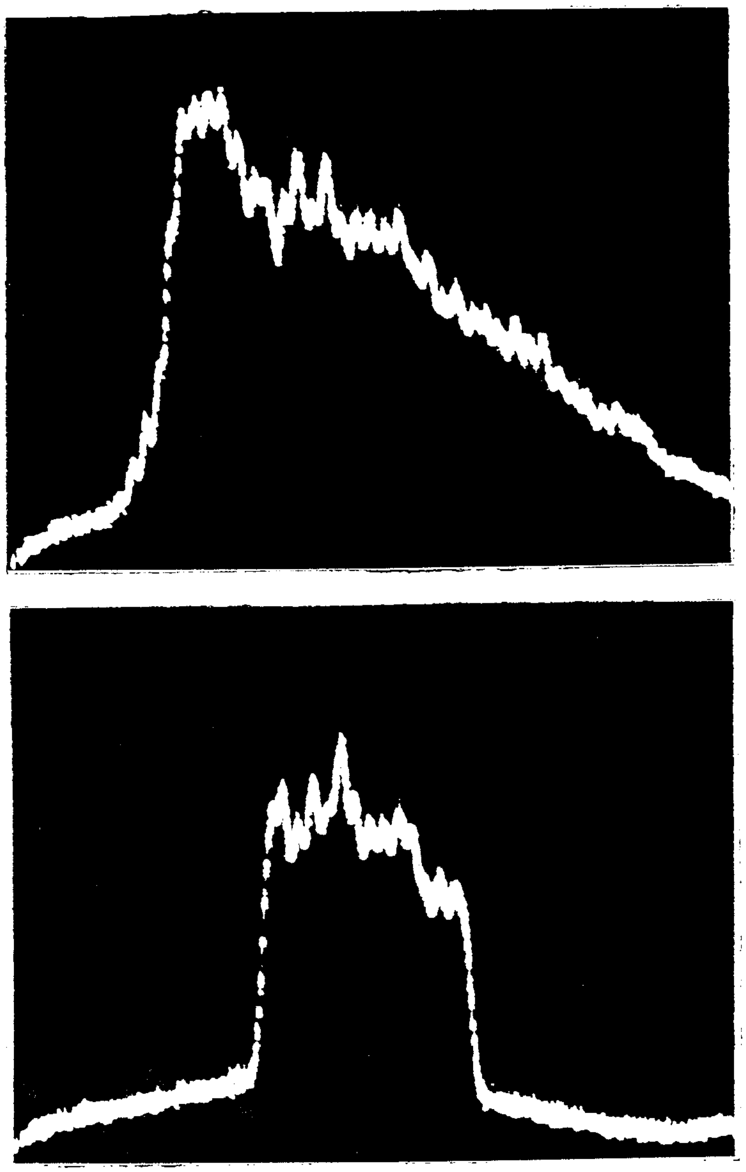

Figure 4.6: Monochrometer measurement of full spectrum emitted from mode-locked laser (top) and spectrum after rectangular filter (bottom).

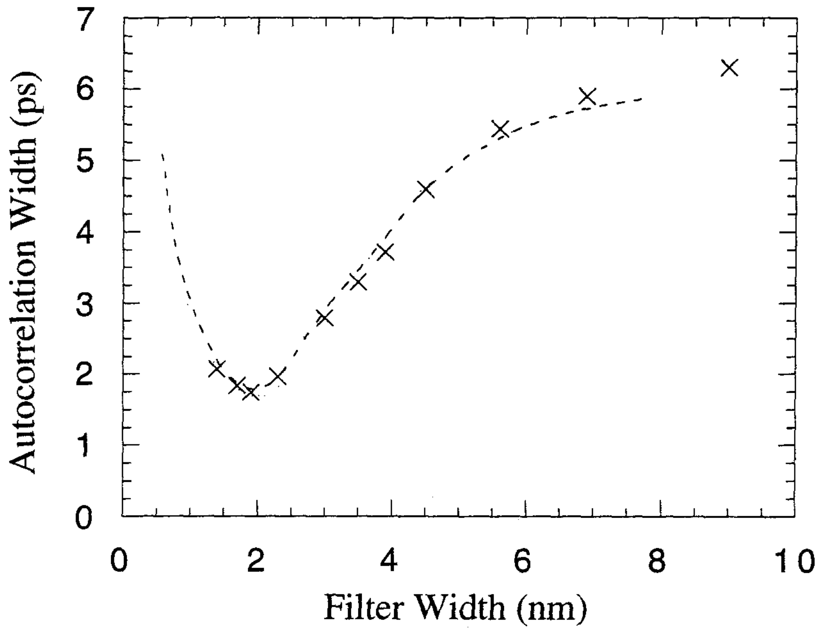

Figure 4.7: Autocorrelation FWHM for different rectangular filter widths. The filter's center frequency remains the same in all cases. The experimental points are shown as × symbols. The rough theoretical fit assuming a fully locked spectrum is shown as a dashed line.

of this rectangular filter experiment and a rough theoretical calculation based on one free parameter for that expected from filtering the chirped triangular optical power spectrum are shown in Fig. 4.7.

In conclusion, the results show quite good agreement with our theoretical expectations from the fully mode-locked single-sawtooth spectrum. Therefore, convincing data is presented showing that a stable, fully mode-locked spectrum is produced by the passively mode-locked semiconductor laser.

References

[1] Y. Silberberg and P. W. Smith, *IEEE J. Quantum Electron.*, **22**, 759 (1986).

[2] P. J. Delfyett, L. Florez, N. Stoffel, T. Gmitter, N. Andreadakis, G. Alphonse, and W. Ceislik, *Opt. Lett.*, **17**, 670 (1992).

[3] R. A. Salvatore, T. Schrans, and A. Yariv, *IEEE Phot.Tech.Lett.*, **5**, 756 (1993).

[4] N. Stelmakh and J. M. Lourtioz, *Electron. Lett.*, **29**, 161 (1993).

[5] P. Simon, N. Gerhardt, and S. Szatmari, *Opt. and Quantum Electron.*, **23**, 73 (1991).

[6] D. J. Kane and R. Trebino, *IEEE J. Quantum Electron.*, **29**, 571 (1993).

[7] J. L. A. Chilla and O. E. Martinez, *IEEE J. Quantum Electron.*, **27**, 1228 (1991).

[8] S. Sanders, A. Yariv, J. Paslaski, J. E. Ungar, and H. A. Zarem, *Appl. Phys. Lett.*, **58**, 681 (1991).

[9] H. Haus, *IEEE J. Quantum Electron.*, **11**, 736 (1975).

[10] A. M. Weiner, J. P. Heritage, and E. M. Kirschner, *J. Opt. Soc. Am. B*, **5**, 1563 (1988).

[11] A. Dienes, J. P. Heritage, M. Y. Hong and Y. H. Chang, *Opt. Lett.*, **17**, 1602 (1992).

[12] T. Schrans, *Ph.D. Thesis*, California Institute of Technology (1994).

[13] E. P. Ippen, D. J. Eilenberger, and R. W. Dixon, *Appl. Phys. Lett.*, **37**, 267 (1980).

[14] T. L. Paoli, and J. E. Ripper, *Phys. Rev. Lett.*, **22**, 1085 (1969).

Chapter 5

Pulse shaping through spectral filtering

Because ultrashort optical pulses are useful in a variety of applications from spectroscopy to laser radar to optical communications, it is useful to develop techniques for shaping them. There is an analogy between nuclear magnetic resonance (NMR), which is one of the dominant techniques for chemical analysis, and ultrashort optical pulse spectroscopy [1]. In the optical case, phase coherence in pump-probe experiments is more difficult to maintain, but some progress has been made in the past five years [2].

Spectroscopy using ultrashort pulses has been used to study carrier dynamics of band structure material, exciton dynamics, super heating/cooling effects, phonon lifetimes in crystalline material, vibrations in amino acid strands, etc. Unlike standard spectroscopy, ultrashort pulse spectroscopy allows the temporal resolution necessary for detailed study of the intermediate products of chemical reactions or determination of the direction chemicals reaction proceed in. There have even been methods demonstrated by which ultrashort pulses can be used not just to identify but also to select or direct chemical reactions [3]. A pair of pulses having a definite optical phase and a controlled time delay between them can be used to perform "the chemist's equivalent of Young's double slit experiment" since one pulse can be used to coherently excite molecules which evolve in time and will show constructive or destructive interference in the transition state depending on the phase and delay of a second pulse. Demonstration of this coherent technique for directed chemical reactions has been carried out in experiments with molecular Iodine [3], and chemists are actively pursuing reactions involving more complicated molecules.

One major area necessary for development of these techniques is the ultrashort pulse shaping systems for the pulse sources in these experiment [4]. Using two liquid crystal spatial light modulators in a system similar to the telescoped dual-grating compression system used in the previous chapter, a programmable amplitude and phase femtosecond pulse-shaping system has been demonstrated [5]. Features of 100 fs within an available 2.9 ps window are generated. The system used a 70 fs mode-locked Ti:sapphire laser at 800 nm to show that arbitrarily positioned and phased pulses could be adequately produced for a source in chemistry applications.

Another important application of pulse shaping systems is to use them to compensate for dispersion that is introduced in the propagation of pulses in optical communication systems. Phase shaping of the optical spectrum can be used to cancel out the dispersion added during propagation. In addition to this, a new and complementary technique has been developed to produce pulses that are more immune to dispersion. This new technique of making spread-resistant pulses will be described in the next section.

5.1 Dispersion compensation through spectral filtering

In the previous chapter, passively mode-locked laser pulses were very well characterized. Now, we can use this convenient well-characterized source of ultrashort pulses as a tool in studies of dispersion compensation. Compensating for dispersive effects, specifically the pulse spreading they induce, is one of the most important problems in optical communications. It is a prerequisite to high data rate ($>$ 10 Gbits/second) transmission over long ($>$ 100 km) distances.

It has already been mentioned in chapter 3 that a number of techniques exist for dispersion compensation. We have, for the first time, demonstrated a technique for making pulses more resistant to the effects of dispersion by shaping their optical spectrum [6]. There is an analogy between temporal pulse dispersion and one-dimensional spatial beam diffraction. Both can be described through the Fresnel integral [7,8]. Using this analogy one can apply previous algorithms from the field of beam shaping to the problem of pulses propagating through a dispersive medium [9]. In the beam shaping problem, one's goal is to enhance the depth of focus. In the case of dispersion, this corresponds to extending the amount of dispersion a pulse can tolerate before it spreads out, or more specifically, since the concept of "spreading out" or pulse width is not unambiguously defined, our algorithm for pulse shaping is optimized to extend the amount of dispersion pulses can tolerate before the peak drops to some predefined minimum level. This technique for spread-resistant pulses may be used in conjunction with most of the other dispersion compensation techniques to further improve performance. A description of the theory and experiment follows.

5.2 Brief theoretical description of spread-resistant pulses

Denoting z as the position along the dispersive channel, v_g as the group velocity, and $T = t - z/v_g$ as the delayed time, the influence of GVD on the complex temporal pulse electric field envelope, $u(T, z)$ is given by [9]

$$u(T,z) = \int_{-\Delta\omega/2}^{\Delta\omega/2} U(\Omega, z=0) \exp(\frac{i\beta_2 z\Omega^2}{2} - i\Omega T) d\Omega, \tag{5.1}$$

where $U(\Omega, 0)$ is the Fourier transform of $u(T, 0)$, Ω is the angular frequency (relative to the laser's center frequency, ω_0), $\Delta\omega$ is the spectral width corresponding to the pulse, and $\beta_2 = d^2\beta/d\omega^2|_{\omega 0}$ is the GVD per unit length.

Recently [9], the possibility of pulses that do not disperse by virtue of their unique shaping was introduced. Based on the time–space analogy, Rosen et al. proposed

$$u(T,0) = u_c(T,0) = \frac{1}{\sqrt{2i\beta_2 f}} \int_{-\infty}^{\infty} \cos[|\frac{t'}{b}|^p - (\frac{t'}{a})^2] \times \exp(i\frac{Tt'}{\beta_2 f}) dt' \tag{5.2}$$

as the initial pulse envelope to reduce the effect of GVD. Here, a, b, f, and $p > 2$ are real positive parameters of the pulse. This pulse ($u = u_c, \Delta\omega = \infty$) propagates along a dispersive channel to a distance of $\Delta z \approx 2\sqrt{2\pi}\beta_2 f^2 p[4(1+p)]^{(2-p)/p}/b^2$ while maintaining a near-constant peak value of $|u_c(0,z)|$. The spectrum of u_c is taken as

$$U(\Omega,0) = U_C(\Omega,0) = \cos[(T_b\Omega)^4 - (T_a\Omega)^2], \tag{5.3}$$

where $T_b = \beta_2 f/b, T_a = \beta_2 f/a$, and the power $p = 4$ has been chosen as an example.

5.3 Simulation of spread-resistant pulses

In what follows we describe a simulation to investigate the possibility of creating dispersion-resistant pulses through pulse shaping and show that it can be accomplished by using a simple binary phase mask in the spectral plane. We find that using a binary approximation of the initial pulse spectrum, $U_B(\Omega,0) = U_C(\Omega,0)/|U_C(\Omega,0)|$, still leads to a considerable reduction in pulse distortion. This approximation enables the use of a binary (0 or π) phase mask instead of a complicated amplitude and phase filter.

The pulse field U_B and its capability of maintaining its shape without distortion when traveling through a dispersive channel depend on the ratio T_b/T_a. We find numerically that $T_b/T_a = \sqrt{8/5}$ is sufficient in that the intensity $I_B(T = 0, z) = |u_B(0,z)|^2$ of the center of the symmetric pulse and its shape remains at a nearly constant height over the interval $\Delta z \approx 8T_b^2/\beta_2$ near $z = 0$. This interval may be increased by increasing the ratio T_b/T_a, yet increasing the interval spoils the constancy of $I_B(0,z)$ in the region of interest. At $z = 0$, the pulse has a main lobe width around $T = 0$ of order T_b and a tail length that depends on $T_b\Delta\omega$. Although reducing $T_b\Delta\omega$ reduces the pulse tail length, it increases the tail intensity compared with $I_B(0,0)$ and introduces small oscillations in $I_B(0,z)$ as a function of z.

In Fig. 5.1 the pulse intensity shape $I(T,z)$ normalized by $I(0,0)$ is shown as a function of the delayed time T for different values of GVD, i.e., the normalized distance $\beta_2 z/2T_b^2$. Fig. 5.1(a)-Fig. 5.1(d) describe $I_B(T,z)/I_B(0,0)$ with a binary phase mask, $U(\Omega,0) = U_B(\Omega,0)$ and $T_b\Delta\omega = 4.044$, using the first nine lobes of the cosine spectrum function. The pulse essentially maintains its shape and height even for $\beta_2 z/2T_b^2 = 1.6$, as can be seen from comparison among Fig. 5.1(a)-Fig. 5.1(c). In these cases the main lobe of the pulse envelope as well as $I_B(0,z)$ are essentially invariant. The changes that occur due to chromatic dispersion are mostly in the tails. The reduction of $I_B(0,z)$ for $\beta_2 z/2T_b^2 = 0.8$ [Fig. 5.1(b)] is a result of finite $T_b\Delta\omega$, as mentioned above. Note that this result is independent of the sign of β_2 because $I_B(0,-z) = I_B(0,z)$. Therefore, in practice one can exploit this fact and shape the pulse $u_B(T,\sim -4T_b^2/\beta_2)$ at the beginning of the dispersive channel and use the full interval of $8T_b^2/\beta_2$.

These results are compared with those from a rectangular spectrum without the phase mask. For this comparison [the solid curves in Fig. 5.1(e)-Fig. 5.1(h)] we choose $U(\Omega,0) = U_S(\Omega,0) = 1$ and spectral width $\Delta\omega_S = 2.156/T_b$ to generate the same pulse main lobe width as with the mask. The pulse shape is $I_S(T,0)/I_S(0,0) = \mathrm{sinc}^2(\Delta\omega_S T)$, where $\mathrm{sinc}(x) = \sin(x)/x$. The primary difference between the pulse

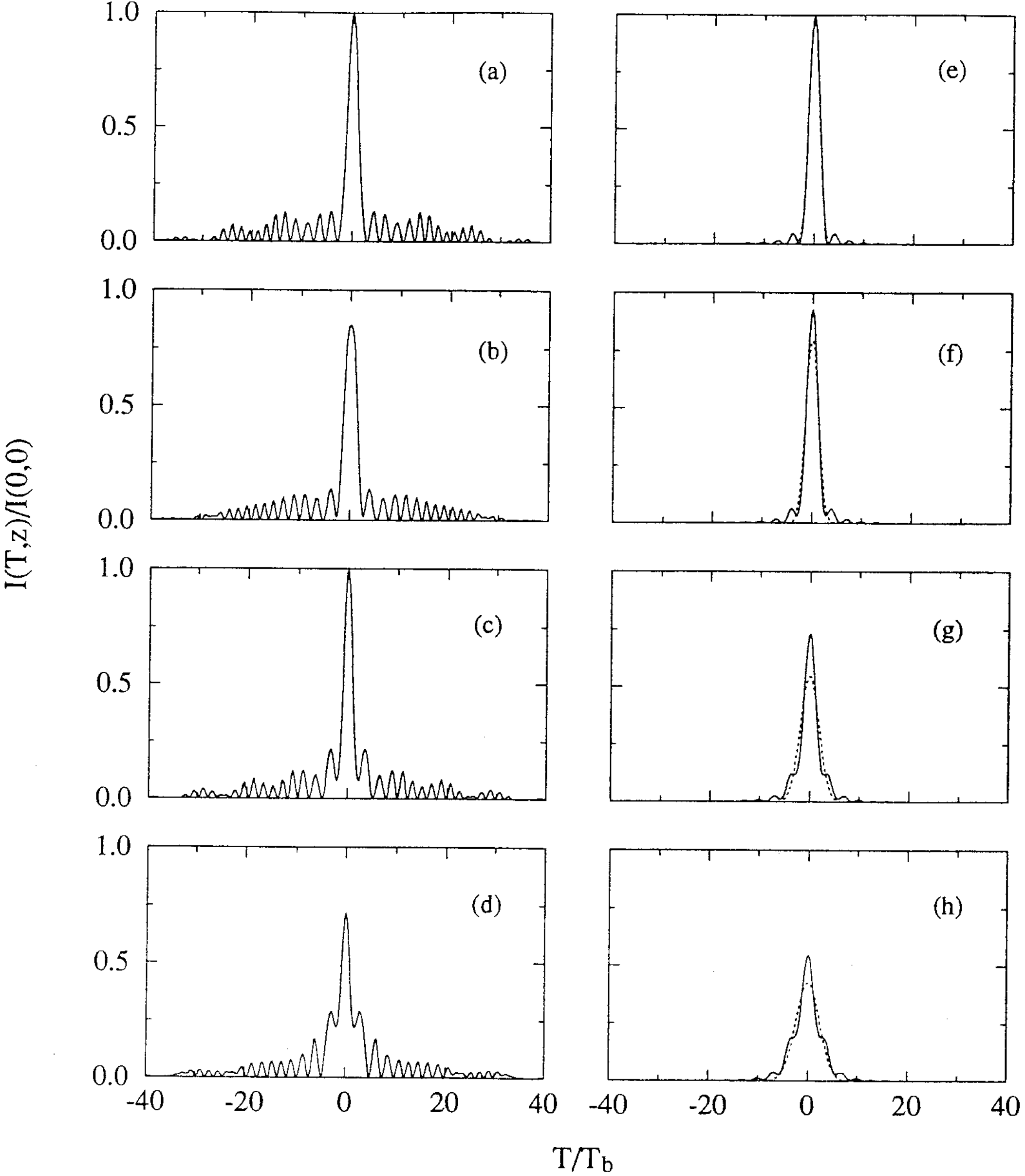

Figure 5.1: Calculated pulse intensity envelopes $I(T,z)/I(0,0)$ after adding different amounts of dispersion. The binary phase mask case $[U(\Omega,0) = U_B(\Omega,0)$ and $T_b\Delta\omega = 4.044]$ is displayed in (a)-(d). The rectangular filter case $[U_S(\Omega,0) = 1$ and $T_b\Delta\omega = 2.156]$ is shown (solid line) in (e)-(h) along with the Gaussian pulse (dotted line). The GVD, $\beta_2 z/2T_b^2$, is equal to: 0 in (a) and (e), 0.8 in (b) and (f), 1.6 in (c) and (g), and 2.2 in (d) and (h).

U_B and U_S is in the tails. The second pulse has shorter tails and therefore suffers more distortion and reduction of $I(0,z)$ compared with $I(0,0)$ along its propagation in the dispersive channel.

Results from the familiar Gaussian pulse [dotted lines in Fig. 5.1(e)-Fig. 5.1(h)] are also compared. This pulse has just one lobe and suffers a reduction of $I_G(0,z)$ at distances even shorter than those of U_S. Its complete dependence on T and z can be written in closed form and is given by

$$\frac{I_G(T,z)}{I_G(0,0)} = \frac{\exp(-\frac{T^2}{T_G^2[1+(\beta_2 z/T_G^2)^2]})}{1+(\beta_2 z/T_G^2)^2]^{1/2}}. \tag{5.4}$$

We chose $T_G = 1.44 T_b$ so that the main lobe width is identical to that of the two cases described above at $z = 0$. From Fig. 5.1(c)-Fig. 5.1(g), one can see that although the Gaussian pulse decays to 54% of its initial intensity [Fig. 5.1(g)], the pulse with the U_B spectrum maintains its value.

5.4 Experimental demonstration of spread-resistant pulses

The above theoretical results were tested experimentally for the cases of U_B and the rectangular spectrum U_S. The experimental setup is shown in Fig. 5.2. The laser is an LPE regrown passively mode-locked quadruple quantum well two-section, GaAs structure as described previously. Its spectrum had half-power points at 839.9 and 845.2 nm in this experiment. The pulse spectrum was flatter on top than the one

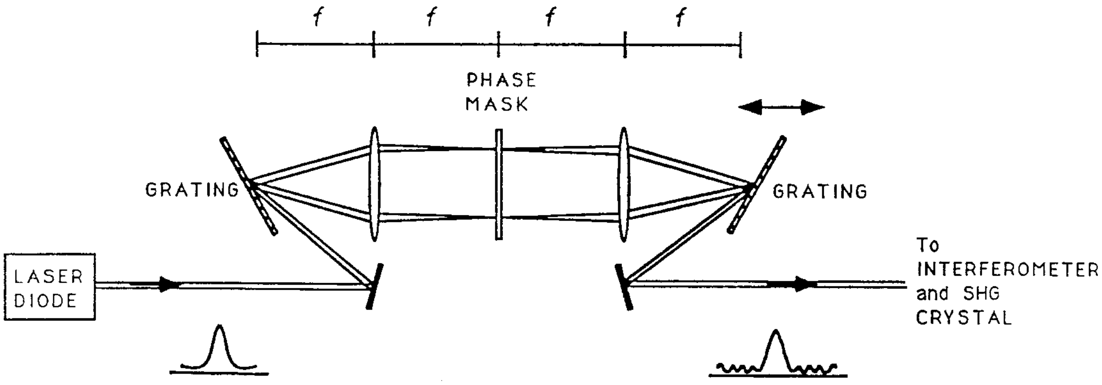

Figure 5.2: The apparatus used for spectral shaping, compression, and fiber GVD simulation. The phase mask is inserted in the spectral plane to shape the pulses.

displayed in the previous chapter and was approximated by a rectangular function with a quadratic phase. The laser pulses were sent to a telescoped dual-grating compressor (1/d = 2000 lines/mm) to achieve pulse shaping [4], laser chirp cancellation, and GVD addition. Different optical frequency components of the input laser pulse are spatially dispersed by the left grating and then resolved spatially in the Fourier plane of the lens. At this plane the spectrum is filtered through either the spatial binary phase mask or a window to reshape the pulse. The spectrum is recombined spatially by a second lens and grating. The laser chirp cancellation and GVD addition are easily achieved by moving the right grating in Fig. 5.2. The laser chirp is canceled by simply moving the grating to minimize the pulse width (without the phase mask or the window) and specifying the position of the grating as $z = 0$. Then the phase mask is introduced in the Fourier plane and autocorrelations measurements are taken for different positions, z, of the right grating. The GVD is given by [10]

$$\frac{\beta_2 z}{2T_b^2} = \frac{\lambda_0^3 z}{4\pi T_b^2 c^2 d^2 \cos^2(\theta)}, \tag{5.5}$$

where z is the distance of the right grating location along the central axis of the dual-grating compression system. Also $\theta = 51.1^o$ is the angle between this axis and the normal to the grating surface, $\lambda_0 = 2\pi c/\omega_0$ is the optical carrier wavelength, and c is the velocity of light.

The reshaped pulses are sent into a Michelson interferometer and a SHG crystal to measure their temporal autocorrelation. Autocorrelations were taken for the case where $U(\omega, 0) = U_B(\omega, 0)$ and $T_b\Delta\omega = 4.044$. We find numerically that the pulse shape is insensitive to small variations in the amplitude distribution of the spectrum. Therefore the assumption of a rectangular function between $-\Delta\omega/2$ and $\Delta\omega/2$ for the laser amplitude spectrum is justified, and the need for a complicated mask is reduced to that for a simple binary phase mask. The mask, made photolithographically [11], has a width of 3.4 mm (the spatial width of the optical spectrum in the Fourier plane), which is equivalent to $\Delta\omega = 12.2 \times 10^{12}$ rad/sec. The mask was encircled by a window of the same width to eliminate undesirable influences from the tails of the spectrum. The index of refraction of the glass mask is $n = 1.5$, therefore the depth of the etching is λ_0. The autocorrelations measured while using the phase mask are given in Fig. 5.3(a)-Fig. 5.3(c). Two parameters (T_b and β_2) describe the fit between the theoretical (solid curves) and experimental (dotted curves) autocorrelation results.

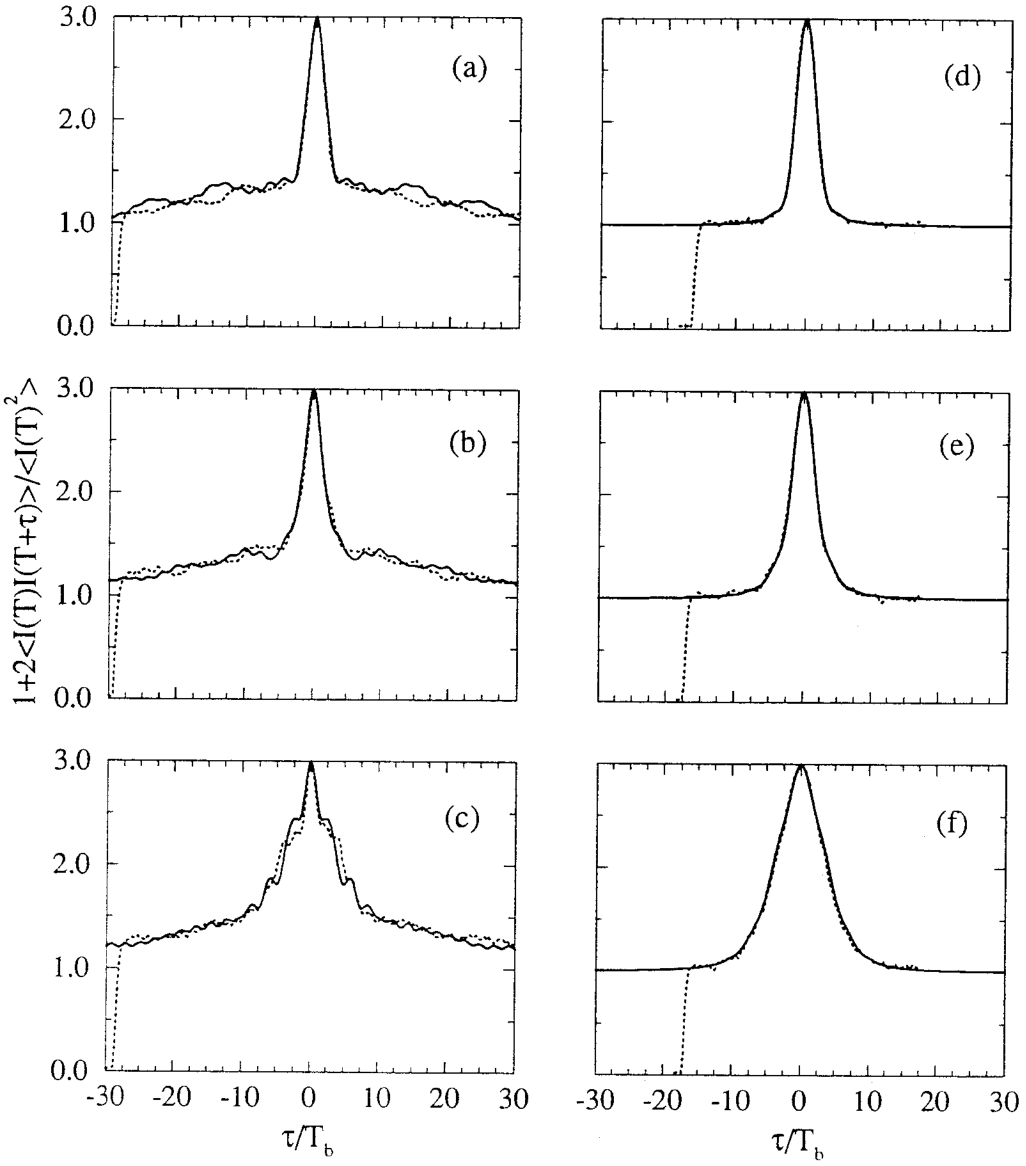

Figure 5.3: Comparison between experimental (dotted curves) and theoretical (solid curves) autocorrelations. Results from the binary phase mask $[U(\Omega,0) = U_B(\Omega,0)$ and $T_b\Delta\omega = 4.044]$ are shown in (a)-(c). Results from the rectangular spectrum $[U_S(\Omega,0) = 1$ and $T_b\Delta\omega = 2.156]$ are shown in (d)-(f). The GVD, $\beta_2 z/2T_b^2$, is equal to: 0 in (a) and (d), 1.1 in (b) and (e), and 2.2 in (c) and (f).

First, for $z = 0$ [Fig. 5.3(a)], the parameter T_b was found to be equal to $T_b = 370$ fs, whereas the theoretical calculation gives $T_b = 4.044/\Delta\omega \approx 340$ fs. A second measurement [Fig. 5.3(b)] was taken at $\beta_2 z/2T_b^2 = 1.1$ ($z = 2.5$ cm) to specify the second parameter β_2 (theoretical calculation gives $\beta_2 z/2T_b^2 = 1.16$ at this location). A third measurement [Fig. 5.3(c)] was taken for $\beta_2 z/2T_b^2 = 2.2$. A good fit is indicated between theoretical and experimental results.

A similar series of autocorrelations was measured without the phase mask, in which $U_S(\omega, 0) = 1$ and $T_b\Delta\omega = 2.156$, to check the rectangular spectrum case. In this case, a window was located in the Fourier plane allowing the center of the laser spectrum to pass and blocking the rest. Its width was adjusted to give the same autocorrelation half width, which is nearly equivalent to getting the same main lobe pulse width as with the phase mask. The allowed spectrum had $\Delta\omega \approx 6.62 \times 10^{12}$ rad/s. The results of this experiment are shown in Fig. 5.3(d)-Fig. 5.3(f). The fit was done without any free parameters. The same values of T_b and $\beta_2 z/2T_b^2$ as before were used. A good agreement between theoretical and experimental results is found again.

Two differences are prominent from the different pulses used to generate Fig. 5.3(a)-Fig. 5.3(f). Firstly, the autocorrelation tails in Fig. 5.3(a)-Fig. 5.3(c) for the pseudo-nondispersive pulse (U_B) decay slowly, reaching the background value of 1 only for very large τ. This is a direct result of the pulse tails as can be seen from Fig. 5.1(a)-Fig. 5.1(d). The U_S pulse, which has much shorter tails, has collinear autocorrelations that reach the value of 1 [Fig. 5.3(d)-Fig. 5.3(f)] for smaller τ. Secondly, for higher values of $\beta_2 z/2T_b^2$, the autocorrelation has steps in it. This occurs when the main lobe of the pulse [Fig. 5.1(d)] becomes comparable in magnitude to the secondary lobes on each side. The width of the autocorrelation for small τ/T_b indicates the width of the main peak of the pulse.

The pulses used in this experiment are approximately 1 ps and therefore experience effects from what are considered rather small magnitudes of dispersion. In a fiber optic communication system at today's state of the art, one typically would use pulses, say for 10 Gbit/s, of 30 ps. In this case, the length of fiber that this compensation technique would be appropriate for is 900 times longer. A table has been calculated to give an idea of the appropriateness of this technique for practical cases. The table shows that approximately a factor-of-three increase in repeater spacings could be obtained (Table 5.1). This would certainly be a significant advantage. The table is for a fiber optic communication system with $\lambda = 1500$ nm, D $= 17$ ps/km/nm or $\beta_2 = 2.03 \times 10^{-26}$ sec^2/m, and $T_b/T_a = \sqrt{8/5}$. Additional complexities are involved in the implementation of such a system, however, since the spectral shaping adds tails that extend far from the pulse. In high speed optical communications, where one sends pulses closely packed in time, these tails will overlap with neighboring pulses and are likely to give a significant decrease in the attainable signal-to-noise ratio due to their interference. Analysis of whether the spectral filtering is still worthwhile in this case is still under investigation.

In conclusion, the possibility of pulse shaping to reduce the distortion caused by GVD was theoretically considered and experimentally checked. It was found that

Pulse FWHM (ps)	Reduction of peak (%)	Distance (km) [Gaussian pulse]	Distance (km) [Shaped Pulse]
1.5	70	0.16	0.58
1.5	50	0.28	0.63
5	70	1.8	6.5
5	50	3.1	7.1
10	70	7.25	26
10	50	12.3	28.1
30	70	65.25	234
30	50	110.8	252

Table 5.1: Spreading in practical fiber optic communications systems. The table shows that distances over which pulses remain relatively unaffected by dispersion can be increased. For example, from last line, a 30 ps Gaussian pulse will fall to half of its original peak intensity in 110.8 km while the spread-resistant pulse presented here will not drop to half its peak intensity until 252 km.

a simple phase mask in the spectral plane can add tails with many lobes, which considerably alleviate distortion to the main lobe of the pulse and permit longer propagation distances in dispersive channels than for other pulses.

References

[1] W. S. Warren and A. H. Zewail, *J. Chem. Phys.*, **78**, 2279 (1983).

[2] W. S. Warren, H. Rabitz, and M. Dahleh, *Science*, **259**, 1581 (1993).

[3] N. F. Scherer, R. J. Carlson, A. Matro, M. Du, A. J. Ruggiero, V. Romero-Rochin, J. A. Cina, G. R. Fleming, and S. A. Rice, *J. Chem. Phys.*, **95**, 1487 (1991).

[4] A. M. Weiner, J. P. Heritage, and E. M. Kirschner, *J. Opt. Soc. Am. B*, **5**, 1563 (1988).

[5] M. M. Wefers and K. A. Nelson, *Opt. Lett.*, **18**, 2032 (1993).

[6] D. Eliyahu, R. A. Salvatore, J. Rosen, A. Yariv, and J. J. Drolet, *Opt. Lett.*, **20**, 1412 (1995).

[7] B. H. Kolner and M. Nazarathy, *Opt. Lett.*, **14**, 630 (1989).

[8] A. W. Lohmann and D. Mendlovic, *Appl. Opt.*, **31**, 6212 (1992).

[9] J. Rosen, B. Salik, A. Yariv, and H. K. Liu, *Opt. Lett.*, **20**, 423 (1995).

[10] E. B. Treacy, *IEEE J. Quantum Electron.*, **5**, 454 (1969).

[11] D. C. O'Shea, J. W. Beletic, and M. Poutous, *Appl. Opt.*, **32**, 2566 (1993).

Chapter 6

High-repetition-rate passive mode-locking theory

6.1 Introduction to time domain models of passive modelocking

Among the most elegant analytical models in optics is the time domain model of passive modelocking. The analytical solution for this steady-state problem was largely developed by Herman Haus in 1975 [1] shortly after a thorough analysis of active mode locking [2]. The analysis expanded on earlier descriptions of passive mode-locking by Letokhov [3], Garmire and Yariv [4], Gunn [5], and New [6] allowing steady-state solutions and parameter ranges to be determined. It is considered the dominant theoretical view of passive modelocking today and was introduced in chapter 2 for this reason.

Every model of a complex physical phenomenon, however, makes some assumptions and a model's inherent assumptions always place some limit on the range of its validity. Some assumptions present in Haus' theory are that:

(1.) The material's gain and loss spectra are symmetric (parabolic) in frequency and are homogeneous.

(2.) Saturation of gain and loss and the change in the optical pulse are small for each pass (i.e. $< 20\%$) such that a linear or quadratic function is sufficient for exponential functions involved in material response.

(3.) Spatial arrangements of elements inside the cavity and colliding pulse effects are not to be considered.

(4.) The discrete mode-locked spectrum is to be modelled as a continuous spectrum so that its Fourier transform and the second derivative of this transform can be easily manipulated.

(5.) Each saturable element (gain and loss), although it may saturate quickly, is considered to recover negligibly during the optical pulse.

(6.) The linear phase effects occurring along with material gain/loss frequency dependence and the nonlinear phase effects occurring along with saturation of gain and loss are both considered negligible.

In most cases these assumptions are adequate and are helpful in presenting a tractable theoretical model of passive modelocking. These assumptions do not all break down in the same cases. For example, assumption 1, which assumes a homogeneously broadened laser, is indeed a useful description for dye, semiconductor, or other lasers whose gain or loss spectra saturate uniformly for an arbitrary optical signal incident on them. The symmetric parabolic spectrum is typically a reasonable assumption since the important region of the spectrum is usually only that very near the peak which has been measured to be nearly parabolic in most cases. The assumption of the loss and gain spectrum possessing the same peak frequency is somewhat less supported but is acceptable if second-order effects or timing jitter effects are not to be studied in detail.

Assumption 2 restricts the applicability to devices with reasonably high reflectivities from the ends of the cavity and to devices in which the laser's absorption and gain do not modify the energy of a pulse by more than 20% in any single pass. This limits the applicability to lasers whose sections are not deeply modulated and is still appropriate for high-repetition-rate modelocking.

Assumption 3 only eliminates the study of second-order effects, and through the choice of appropriate parameters one will be able to take into account the resulting effects from additional parameters.

Assumption 4 is accurate in all cases except when the modes of the mode-locked laser are separated quite far in frequency. The inaccuracy of this assumption will become apparent when the mode spacing becomes about 1/5 of the spectral FWHM.

This may cause the model to break down at high repetition rates. To consider the accuracy of this assumption (assumption 4) one should accept Haus' other assumptions for the sake of a fair comparison and first just consider the accuracy of the approximation of a discrete spectrum by a continuous spectrum. Haus arrives at the result (e.g. chirp-free, approximating exponentials, etc.) that the spectral envelope should be

$$E(f) = \mathrm{sech}(f/\Delta f_{spect}). \tag{6.1}$$

This implies the time domain pulse envelope is

$$E(t) = \mathrm{sech}(\pi^2 \Delta f_{spect} t). \tag{6.2}$$

The true mode-locked spectrum is discrete and has the form

$$E(f) = \sum_{n=-\infty}^{\infty} \mathrm{sech}(n\Delta f/\Delta f_{spect})\delta(f - n\Delta f) \approx \mathrm{sech}(f/\Delta f_{spect}), \tag{6.3}$$

with the approximate equality representing what I will call the continuous spectrum approximation. This continuous spectrum approximation is only accurate when Δf is small. Here Δf represents the mode spacing as defined in Fig. 6.1. Of course, the pulse train period is $T_{per} = 1/\Delta f$, thus it is apparent that if Δf is large enough such that the repetition period is within a factor of ten of the pulse width, some overlap of the previously assumed independent pulses exists, and the time domain result may not be accurate. Fourier transforming the above spectrum leads to

$$E(t) = 1/2 + \sum_{n=1}^{\infty} \mathrm{sech}(n\Delta f/\Delta f_{spect}) \cos(n2\pi\Delta f t) \approx \mathrm{sech}(\pi^2 \Delta f_{spect} t). \tag{6.4}$$

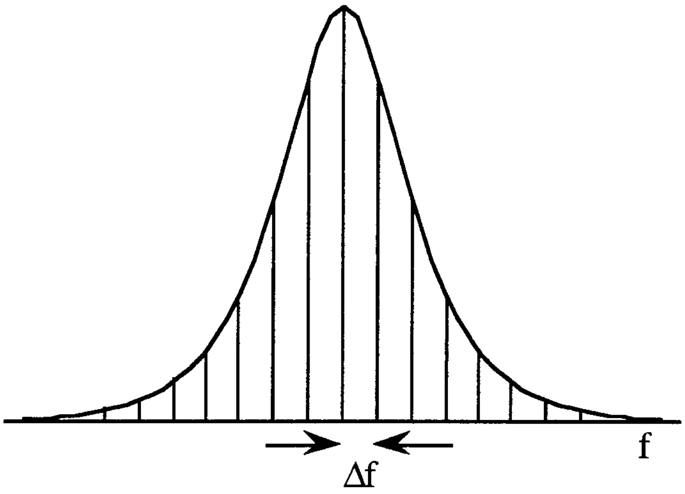

Figure 6.1: The mode spacing, Δf, is shown for the a high repetition rate mode-locked spectrum. Haus' theory uses the envelope to approximate the actual spectrum.

The approximation in the previous equation is compared for various mode spacings. A plot with $\Delta f = 0.569$ of the spectral full width at half maximum is shown in the Fig. 6.2 and already shows some disagreement with a normalized RMS error calculated to be 4.9%. For a range of Δf values, a curve of normalized RMS error values is plotted in Fig. 6.3. The onset of significant error occurs when Δf is about 0.380 of the spectral FWHM, and the plot vividly demonstrates that there are some assumptions in Haus' theory that do not permit it to accurately describe high-repetition-rate modelocking.

In fact, the gain material has a spectral response $\sim 1 - b\Omega^2$ and reshapes the optical spectrum each time the pulse passes through it (here we are still ignoring saturation effects). Only in the case of a continuous spectrum can one say this is

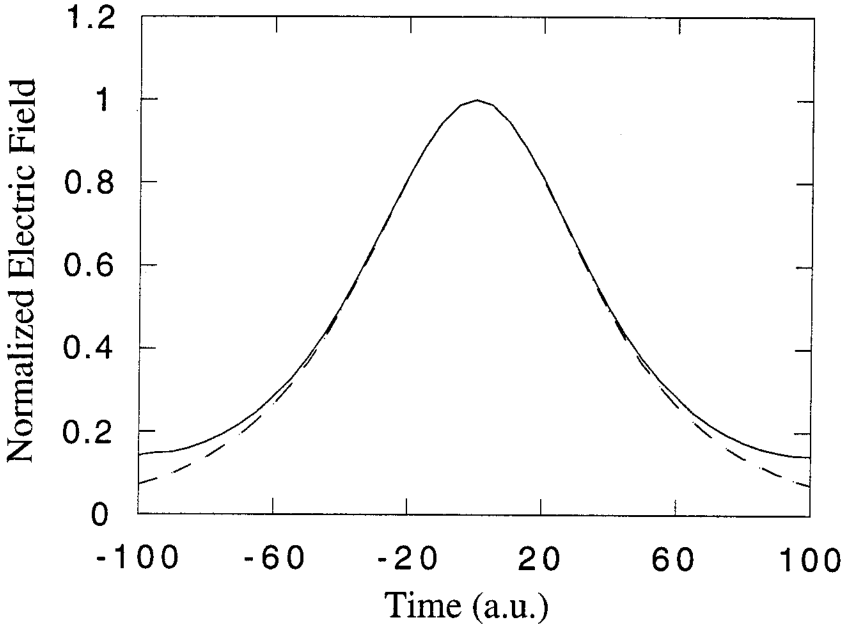

Figure 6.2: Agreement of the actual pulse shape with $\Delta f = 0.569$ (dashed line) and pulse shape from the continuous spectrum approximation (solid line).

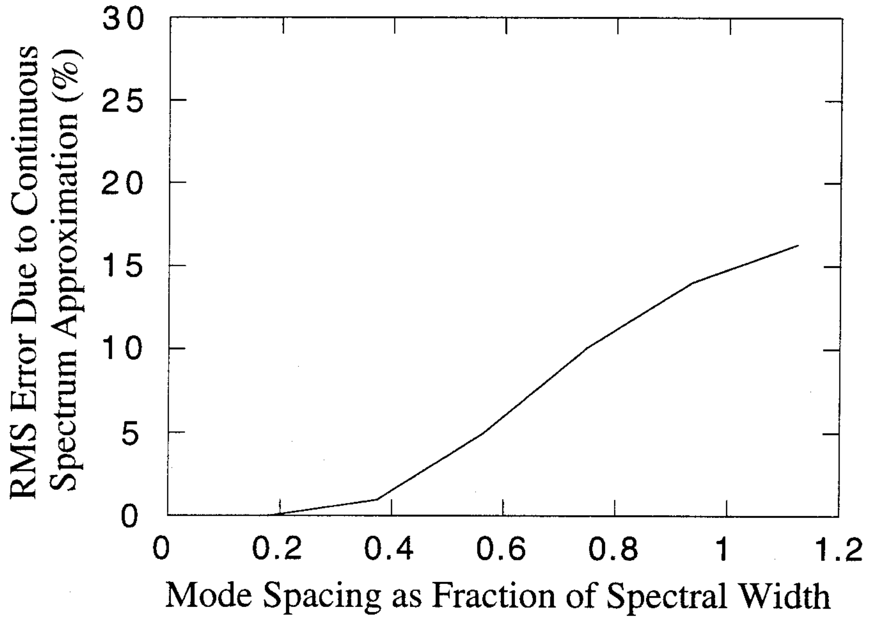

Figure 6.3: Plot showing the adequacy of the continuous spectrum approximation versus mode spacing.

equivalent to an operator of $(1 + b\frac{d^2}{dt^2})$ in time domain as in Eqn. (2.5). Therefore the continuous spectrum approximation is involved once again, here. In this case the agreement between the time domain second derivative from the approximation and the corresponding quantity from the exact calculation are even further in disagreement since the tail in the time domain extends farther, meaning the independence of some of the pulses displayed in Fig. 6.3 is actually an optimistic estimate.

6.2 Limits of the standard time domain model due to carrier saturation

Not only does the continuous spectrum approximation present a source of error in the standard time domain model at high repetition rates, but even larger discrepancies result from approximating the carrier saturation and recovery effects. To date, I am aware of no studies on the adequacy of this standard time domain model for high-repetition-rate lasers, yet there has been attempted application of the theory for describing high-repetition-rate lasers [8].

Using the form of $E(t)$ for discrete modes spaced Δf apart, we may calculate the material's response through the rate equations for the gain and loss,

$$\frac{dn_g(t)}{dt} = \frac{-n_g(t)}{\tau_g} - G|E(t)|^2(n_g(t) - n_{tr}) + R_{pg} \tag{6.5}$$

and

$$\frac{dn_a(t)}{dt} = \frac{-n_a(t)}{\tau_a} - A|E(t)|^2(n_a(t) - n_{tr}), \tag{6.6}$$

where the terms above have been defined in chapter 2. One expects that if Δf approaches $1/\tau_g$ or $1/\tau_a$, the material does not recover fully at any point within the cycle. However, the standard time domain model assumes a full recovery between pulses. Therefore, it gives a greatly overestimated modulation depth of the carrier densities at high repetition rates. When the model is applied to cases where the carrier recovery between pulses is incomplete, the reduction in the magnitude of carrier modulation depth which is limited by the exponential material recovery occurring over the cycle period T_{per}, can be partially taken into account [1]. Still, at high repetition rates, for example, if the pulse width is more than $T_{per}/10$, a noticeable amount of the material's recovery occurs within the pulse itself and less than 9/10 occurs during the space between pulses. Most high repetition rate lasers have a duty cycle far larger than 1/10, and therefore in this regime, the accuracy of this assumption becomes questionable. For reasonable parameters of monolithic semiconductor lasers as shown in the parameter list below, a calculation testing the accuracy of this assumption has been carried out.

$$n_{tr} = 1 \times 10^{18}\,\mathrm{cm}^{-3}$$

$$\tau_g = 1\,\mathrm{ns}$$

$$\tau_a = 0.3\,\mathrm{ns}$$

$$G = 1 \times 10^{-15}\,\mathrm{cm}^2$$

$$A = 3 \times 10^{-15}\,\mathrm{cm}^2$$

$$E_0 = 1.903 \times 10^{12}\,\mathrm{cm}^{-2}\mathrm{sec}^{-1}$$

$$R_{pg} = 5.23 \times 10^{27}\,\mathrm{cm}^{-3}\mathrm{sec}^{-1}$$

$$n_g(t = 0) = 3 \times 10^{18}\,\mathrm{cm}^{-3}$$

$$n_a(t = 0) = 5 \times 10^{17}\,\mathrm{cm}^{-3}$$

The calculation involved breaking the period of one repetition cycle into 200 points in time and numerically integrating the rate equation over this interval. Initial volumetric carrier densities for each section were assumed, $n_g(t = 0)$ and $n_a(t = 0)$. The peak electric field, E_0, was chosen such that the absorber carrier density possesses the same value at the beginning and end of each cycle. Then, requiring the same condition to be satisfied for the gain, R_{pg},the gain pumping rate, was chosen. An example of the time evolution of the carrier density for $\Delta f = 0.15$ (normalized to the spectral FWHM) is shown in Fig. 6.4 for one repetition cycle. One can see a significant disagreement exists during the pulse, even though the same maximum and minimum carrier densities are obtained in both cases. The pulse-intensity-weighted RMS error is found to be 29% in this case, meaning that even during the pulse, a considerable disagreement is obtained at high repetition rates for Haus' $n(t) \sim \exp(\frac{V}{2}(1 + \tanh(t))$ expression resulting from assumption 5. A plot of the pulse-intensity-weighted RMS error for various Δf is displayed in Fig. 6.5 and shows significant error results for assumption 5 if $\Delta f < 0.019$ of the FWHM, showing it will generate questionable results when used to analyze high-repetition-rate lasers.

In summary of this section on the limits of the standard time domain model for passive modelocking, assumption 1-3 were not expected to impose significant limits on

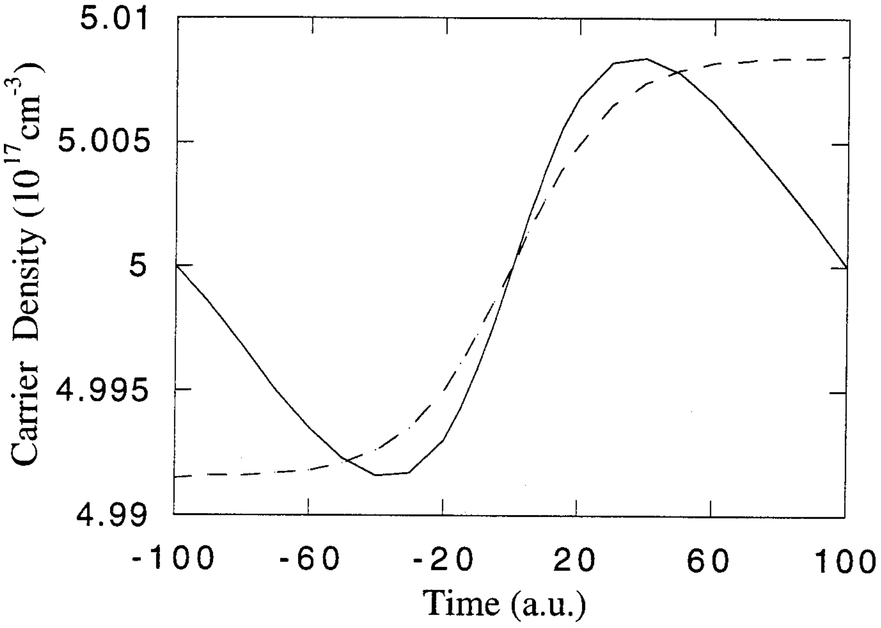

Figure 6.4: Change in the absorber carrier density during one cycle. The dashed line shows what would be derived from Haus' model.

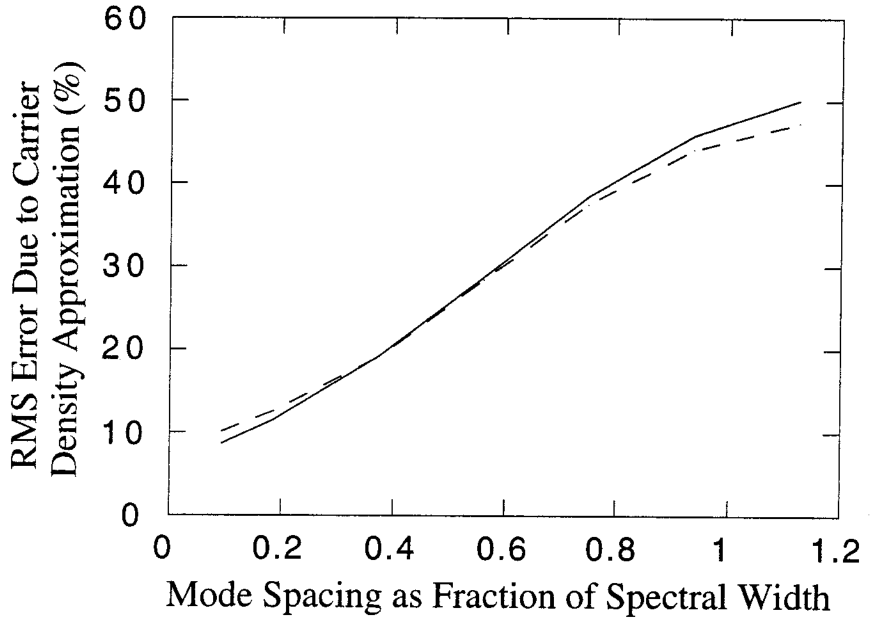

Figure 6.5: Pulse-intensity-weighted RMS error in the absorber carrier density (solid line) and the gain carrier density (dashed line) during one cycle plotted against mode spacing.

high-repetition-rate modelocking, assumption 4 is expected to limit the model to rates of $\Delta f < 0.380$, and assumption 5 is expected to limit the application of the model to rates of $\Delta f < 0.019$ or, more practically, duty cycles of about 5% or less which are certainly considered to be outside the regime of high-repetition-rate semiconductor lasers. Nothing has been mentioned yet about the limits of assumption 6. It is well known from experimental studies that most mode-locked semiconductor pulse trains are composed of strongly chirped pulses. There are some cases in which the mode-locked semiconductor laser has generated essentially unchirped pulses [7,8], and there has been some work extending the standard time domain mode-locking model to chirped pulses [9,10], however, these have only involved phase effects from fast saturable absorption (i.e., the assumption that the absorber recovers much quicker than the pulse duration) and are inappropriate for mode-locked semiconductor laser studies. The investigation of assumption 6 and chirped pulse high-repetition-rate modelocking will follow the extensive development of a frequency domain steady-state model of high-repetition-rate passively mode-locked lasers.

6.3 A supermode model for high-repetition-rate passive modelocking

In this section, a steady-state analysis of high-repetition-rate passively mode-locked semiconductor lasers is derived. The analysis includes effects of amplitude-to-phase coupling in both gain and absorber sections. A many-mode eigenvalue approach is presented to allow one to obtain supermode solutions. Using a nearest-neighbor mode coupling approximation, chirp-free pulse generation is explained. The presence of a non-zero alpha parameter is found to change the symmetry of the supermode and significantly reduce the mode-locking range over which the lowest-order supermode remains the minimum gain solution. The effects of individual laser parameters are considered, and agreement with recent experimental results is discussed. In addition to explaining the steady-state operation of the laser, another motivation exists for finding the supermode solution and that is that once the supermode solution is known, the noise effects due to perturbations around this steady state can accurately be found.

Previously, the theory of passive modelocking has been analyzed thoroughly in the time domain [1], but calculations in the previous section have shown Haus' model to be inaccurate for high-repetition-rate modelocking. Active mode-locking, on the other hand, has been analyzed thoroughly in both the time domain and the frequency domain [11]-[13]. It has been suggested that passive mode-locking should be analyzed in the time domain since simple products in the time domain analysis result in cumbersome convolutions in the frequency domain analysis [2], however, in the case of high-repetition-rate passive modelocking, where few modes are involved and the induced carrier modulation is much closer to a sinusoid [14], the frequency domain approach becomes more appropriate. In this section, an analysis is done in the frequency domain, extending that presented in [14]. Section 6.4 describes the model and arrives at an equation for each mode in the supermode. It incorporates dispersive effects through the common semiconductor laser parameters and is carried out for more than just three modes. Section 6.5 describes the eigenvalue formulation used to arrive at a self-consistent solution of the coupled nonlinear equations. Section 6.6 presents an approximate analytical expression based on (the minimum) three modes in order to reduce the complexity and allow one to build physical intuition about the gain requirements and amplitudes and phases of the supermode spectrum. Section 6.7 presents results for the full calculation. The following chapter will compare the results with experiments for high-repetition-rate passively mode-locked lasers and include conclusions.

6.4 Derivation of model for supermode analysis

High-repetition-rate modelocking ($\geq$ 50 GHz) was first demonstrated by Vasil'ev [15] and by Sanders et al. [16]. To date, semiconductor lasers are the only mode-locked lasers that have been able to generate repetition rates of hundreds of GHz. Due to their large material gain coefficients, short recovery times, and the ability to be made into short monolithic cavities, high-repetition-rate pulse trains can be generated easily. Typically, high-repetition-rate lasers involve a monolithic semiconductor laser structure, meaning no external cavity is used. The model presented is intended to analyze the monolithic multisection laser, and no intention of including an external cavity is made here although one could easily modify the modelled cavity to include a reflection-free facet and some length of free space to account for an external cavity.

Passive modelocking requires a minimum of two sections such that one section is

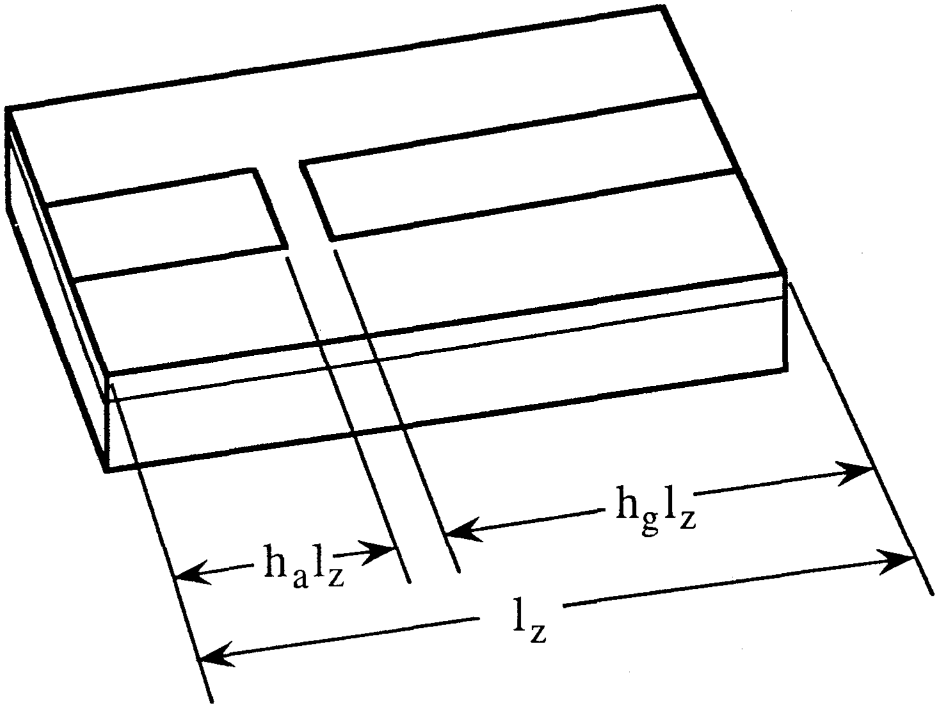

Figure 6.6: Schematic for two-section monolithic passively mode-locked laser.

pumped above transparency and one remains below. A standard two-section monolithic passively mode-locked laser structure is shown in Fig. 6.6. More complex structures have been made to achieve Bragg filtering [17], incorporate additional sections [7], change recombination rates [18], or develop transient gratings to increase the effectiveness of absorber saturation [7]. The steady-state effects of each of these can be taken into account by adjusting the appropriate parameters of the model in Fig. 6.6.

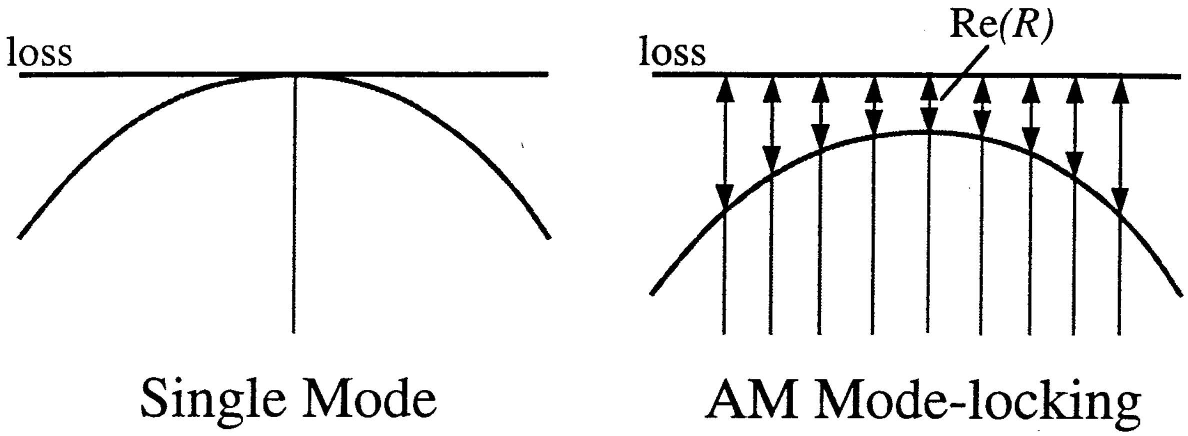

Figure 6.7: Without any mode coupling a homogeneously broadened laser will lase in the single mode at which the gain and loss are equal (left side of figure). Allowing mode coupling, amplitude modulated (AM) passive modelocking may permit a cooperative saturation of the absorber during some part of the repetition cycle and allow supermode lasing to occur (right side) with a lower threshold gain than if mode coupling were disallowed.

Physically, one may model the average net gain of a semiconductor laser as having an approximately parabolic spectrum near its peak. Typically, if one pumps the gain strongly enough, it will reach a point at which the gain equals the loss as shown in the left side of Fig. 6.7. If the gain equals the loss for some mode, this mode will start lasing, the homogeneous gain will become clamped, and further pumping will go into generating light in the lasing mode.

On the other hand, if one allows a coupling to exist between the modes, the presence of light in mode n, under some conditions, can make it easier for the light in mode $n+1$ (and vice versa) to saturate through the absorber at certain times during the repetition cycle. Thus, the laser may operate at a lower average carrier density than it could if mode coupling were disallowed (see right side of Fig. 6.7). One can write an equation for the net gain of each mode including the coupling effects due to each of its neighboring modes. Also there are phase effects, and for stable mode-locking one requires that all the modes will be equally spaced in frequency. The rest of this section will be devoted to deriving an equation for each of these coupled modes which will subsequently be solved to find the supermode for the high-repetition-rate passively mode-locked laser.

The net optical field inside the laser can be written as a sum over individual modes,

$$\vec{E}(\vec{r},t) = \sum_n \mathcal{E}_n(t)\vec{u}_n(\vec{r}), \tag{6.7}$$

where $\mathcal{E}_n(t)$ represents the time dependence of mode n, and $\vec{u}_n(\vec{r})$ represents the nth spatial eigenmode of the cold cavity and satisfies $\nabla^2\vec{u}_n(\vec{r}) + \mu_0\varepsilon_n{\Omega_n}^2\vec{u}_n(\vec{r}) = 0$. Here, μ_0 is the magnetic permeability of free space, ε_n is the electric permittivity, and Ω_n is the resonant frequency of the nth mode of the cold cavity. Assuming we have some uniform guiding (through index or gain-guiding) structure longitudinally throughout the laser, we can write

$$\vec{u}_n(\vec{r}) = \sqrt{2}\vec{a}(x,y)\cos(\beta_n z). \tag{6.8}$$

These modes of the cold cavity may be delta-function normalized,

$$\int \vec{u}_n(\vec{r})\cdot\vec{u}_m(\vec{r})dV = V_c\delta_{nm}. \tag{6.9}$$

Similar to (6.7) the net electronic polarization can be written as a sum of terms separable in space and time. Upon writing the wave equation for the net field and polarization and projecting onto $\vec{u}_n(\vec{r})$, we find

$$\frac{d^2\mathcal{E}_n(t)}{dt^2} + \frac{1}{\tau_{pn}}\frac{d\mathcal{E}_n(t)}{dt} + \Omega_n^2\mathcal{E}_n(t) = \frac{-1}{\varepsilon_n}\frac{d^2\mathcal{P}_n(t)}{dt^2}, \tag{6.10}$$

where $\mathcal{P}_n(t) = \frac{1}{V_c}\int \vec{P}(\vec{r},t)\cdot\vec{u}_n(\vec{r})dV$ is the projection of the polarization on mode n. Here τ_{pn} represents the photon lifetime for the nth mode.

With the optical frequency much greater than the repetition rate, we may write $\tilde{E}_n(t)$ as the slowly varying complex envelope of $\mathcal{E}_n(t)$ such that

$$\mathcal{E}_n(t) = \frac{1}{2}\tilde{E}_n(t)e^{i\omega_n t} + c.c., \tag{6.11}$$

where ω_n is the optical angular frequency of the nth lasing mode ($\omega_n \neq \Omega_n$ for non-zero detuning), and correspondingly $\tilde{P}_n(t)$ may be written as the slowly varying complex envelope of the polarization. Thus,

$$\frac{d\tilde{E}_n(t)}{dt} - i(\Omega_n - \omega_n)\tilde{E}_n(t) + \frac{1}{2\tau_{pn}}\tilde{E}_n(t) = -\frac{i\omega_n}{2\varepsilon_n}\tilde{P}_n(t), \tag{6.12}$$

where $\tilde{P}_n(t)$ will contain coupling terms to electric fields spaced at harmonics of the repetition rate, $\Delta = \omega_n - \omega_{n-1}$, since the net polarization is given by

$$\vec{P}(\vec{r},t) = \varepsilon_0\chi(\vec{r},t)\vec{E}(\vec{r},t), \tag{6.13}$$

where

$$\chi(\vec{r},t) = f(\omega_n)\chi_0(\vec{r}) + \sum_{k>0} f(\omega_{n+k})\chi_k(\vec{r})\cos(k\Delta t + \psi_k(\vec{r})) \tag{6.14}$$

may possess optical-pulse-induced oscillations in the carrier density [14], and $f(\omega_n)$ takes into account the frequency dependent gain or loss of the material. Although in general the material's loss spectrum has somewhat different center and shape than that of the material's gain spectrum, we shall not attempt to model that here.

Because lasers tend to operate at their gain peak and semiconductor lasers have a significant contribution of gain-dependent phase shift at their gain peak, $\chi_k(\vec{r}) = \chi'_k(\vec{r}) + i\chi''_k(\vec{r})$ presents not only a gain but a change in refractive index as well. The mode-locked laser is in fact no better in this respect. It tends to operate at an even longer wavelength than a continuous wave (CW) laser (due to the presence of the absorber) [14] and is expected to produce even a slightly larger amplitude-to-phase coupling factor α in its gain section [20], where $\alpha = -\chi'_k(\vec{r})/\chi''_k(\vec{r})$.

Since $\tilde{P}_n(t)$ is computed from a projection of $\vec{P}(\vec{r},t)$ onto $\vec{u}_n(\vec{r})$ over the whole length of the laser, there is a contribution from both the gain and absorbing sections

$$\tilde{P}_n(t) = f(\omega_n)\frac{\varepsilon_0}{V_c}\xi_0\tilde{E}_n(t)+$$

$$\frac{\varepsilon_0}{V_c}\sum_{k>0}[f(\omega_{n-k})(\xi_{kg-}e^{i\psi_{kg}}+\xi_{ka-}e^{i\psi_{ka}})\tilde{E}_{n-k}(t)+f(\omega_{n+k})(\xi_{kg+}e^{-i\psi_{kg}}+\xi_{ka+}e^{-i\psi_{ka}})\tilde{E}_{n+k}(t)], \tag{6.15}$$

where

$$\xi_0 = \int \chi_0(\vec{r})|\vec{u}_n(\vec{r})|^2 dV \tag{6.16}$$

and

$$\xi_{k(g/a)\pm}e^{i\psi_{k(g/a)}} = \int \chi_{k(g/a)}(\vec{r})\vec{u}_{n\pm k}(\vec{r})\cdot\vec{u}_n(\vec{r})dV. \tag{6.17}$$

(The notation (g/a) indicates quantities pertaining to the gain or absorber region, respectively.) We will use $\chi'' = \hat{g}\mu_r c/\omega_0$ to relate the material gain coefficient, $\hat{g}$, to the imaginary part of the susceptibility with μ_r being the cold-cavity refractive index.

The imaginary part of (6.16) yields

$$f(\omega_n)\frac{\xi_0''}{V_c} = \frac{f(\omega_n)\Gamma\mu_r c}{\omega_0}[\hat{g}h_g + \hat{a}h_a], \tag{6.18}$$

and this term is proportional to the average single pass gain where Γ is the confinement factor, c is the speed of light, $\hat{a}$ is the material gain coefficient of the absorber section ($\hat{a} < 0$), l_z is the total laser length, and h_g and h_a are the ratios of the gain section and absorber section lengths, respectively, to the full laser length. The term $\xi_{kg\pm}e^{-i\psi_{kg}}$ will be determined from the carrier dynamics by using a linear approximation for the change in optical gain (loss) versus carrier density for the gain (absorber) section with $\hat{g} = G(n_g(t) - n_0)$. Here, G is the differential gain, $n_g(t)$ is the the time dependent carrier density, and n_0 is the carrier density at transparency. Correspondingly, $\hat{a} = A(n_a(t) - n_0)$ for the absorber.

Gain and absorber dynamics result from the photon intensity, which is proportional to

$$S(z,t) = s_0 + \sum_k s_k(z)\cos(k\Delta t) \tag{6.19}$$

with

$$s_0 = \langle s_0(z)\rangle_\lambda = \frac{1}{2}\langle \sum_{n=-q}^{q} |\tilde{E}_n(t)|^2 u_n^2(z)\rangle_\lambda \tag{6.20}$$

and

$$s_k(z) = s_k\cos(\frac{k\pi z}{l_z}) = \langle \sum_{n=k-q}^{q} \tilde{E}_n(t)\tilde{E}_{n-k}^*(t)u_n(z)u_{n-k}(z)\rangle_\lambda, \tag{6.21}$$

where $\langle\rangle_\lambda$ represents a spatial average over a wavelength. Permitting this form, one notices from the carrier rate equation that a modulation in the light intensity will induce a modulation in the carrier density at the same fundamental and harmonics of that frequency. However, the effect of both the small number of modes and the shorter in-phase overlaps of quickly beating pairs of modes causes the coupling of higher harmonics to drop off. Ignoring the terms responsible for second nearest neighbor and higher coupling terms to simplify the problem and still keep it suitable for high-repetition rate modelocking, from the carrier rate equation,

$$\frac{dn_{(g/a)}(z,t)}{dt} = R_{p(g/a)} - (\hat{g}/\hat{a})(z,t)S(z,t) - \frac{n_{(g/a)}(z,t)}{\tau_{(g/a)}}, \tag{6.22}$$

we find a saturated material gain $\hat{g}$ for the gain section, dependent on the gain recombination time τ_g and the injection pumping $R_{p(g/a)}$ and correspondingly $\hat{a}$ for the absorber section dependent on the absorber recombination time τ_a,

$$\hat{g} = \frac{\hat{g}'}{1 + G\tau_g s_0} \tag{6.23}$$

$$\hat{a} = \frac{\hat{a}'}{1 + A\tau_a s_0}. \tag{6.24}$$

Here, $\hat{g}'$ and $\hat{a}'$ represent the unsaturated gain and unsaturated loss. Additionally, the carrier density is written $n_{(g/a)}(z,t) = n_{0(g/a)} + n_{1(g/a)}(z)\cos(\Delta t + \psi_{(g/a)}) + \ldots$, and terms showing modulation at the first harmonic in the rate equation lead to:

$$\tilde{n}_{g1}(z) = \frac{-\hat{g}s_1(z)}{\sqrt{\Delta^2 + (1/\tau_g + Gs_0)^2}}, \tag{6.25}$$

$$\psi_g = -\arctan\left(\frac{\Delta}{1/\tau_g + Gs_0}\right), \tag{6.26}$$

$$\tilde{n}_{a1}(z) = \frac{-\hat{a}s_1(z)}{\sqrt{\Delta^2 + (1/\tau_a + As_0)^2}}, \tag{6.27}$$

and

$$\psi_a = -\arctan(\frac{\Delta}{1/\tau_a + As_0}). \tag{6.28}$$

So the carrier modulation becomes small and it lags the optical pulses by nearly $\pi/2$ radians since the repetition rate is well beyond the recombination rate or saturation rate. Computing the spatial integrals in (6.17), we find that

$$\frac{\xi_{1g\pm}e^{i\psi_g}}{V_c} = (-\alpha_g + i)\frac{{\mu_r}^2}{\omega_0\tau_p}\kappa_g s_1 e^{i\psi_g}, \tag{6.29}$$

where

$$\kappa_g = \frac{-G\tilde{g}_0}{\sqrt{\Delta^2 + (1/\tau_g + Gs_0)^2}}[\frac{1}{2} + \frac{1}{4\pi h_g}\sin(2\pi h_g)] \tag{6.30}$$

and

$$\tilde{g}_0 = \Gamma\hat{g}h_g\frac{c\tau_p}{\mu_r} \tag{6.31}$$

is the normalized gain. Likewise for the part of the integral over the absorber,

$$\frac{\xi_{1a\pm}e^{i\psi_a}}{V_c} = (-\alpha_a + i)\frac{{\mu_r}^2}{\omega_0\tau_p}\kappa_a s_1 e^{i\psi_a}, \tag{6.32}$$

where

$$\kappa_a = \frac{-A\tilde{a}_0}{\sqrt{\Delta^2 + (1/\tau_a + As_0)^2}}[\frac{1}{2} + \frac{1}{4\pi h_a}\sin(2\pi h_a)] \tag{6.33}$$

and

$$\tilde{a}_0 = \Gamma\hat{a}h_a\frac{c\tau_p}{\mu_r}. \tag{6.34}$$

One can write the single pass gain from (6.18) along with its corresponding phase contribution. Also, for generality, one should allow the inclusion of a frequency dependence [21] of α (accomplished through $\alpha_{(g/a)n}$), giving the single pass net gain and phase effects that are not due to coupling as

$$\frac{\xi_{0n}}{V_c} = f(\omega_n)\frac{\mu_r^2}{\omega_0\tau_p}[(-\alpha_{gn} + i)\tilde{g}_0 + (-\alpha_{an} + i)\tilde{a}_0]. \tag{6.35}$$

For steady state we can ignore all time derivatives and using (6.12), (6.15), (6.29), (6.31), (6.32), (6.34), and (6.35), the equation for mode n becomes,

$$\{2i\tau_{pn}(\Omega_n - \omega_n) - 1 + f(\omega_n)[(1 + i\alpha_{gn})\tilde{g}_0 + (1 + i\alpha_{an})\tilde{a}_0]\}\tilde{E}_n + \frac{s_1}{s_0}(\tilde{\eta}_{n-}\tilde{E}_{n-1} + \tilde{\eta}_{n+}\tilde{E}_{n+1}) = 0, \tag{6.36}$$

where we have defined coupling coefficients for the nearest neighbor modes,

$$\tilde{\eta}_{n-} = f(\omega_n)[\kappa_g(1 + i\alpha_{gn})e^{i\psi_g} + \kappa_a(1 + i\alpha_{an})e^{i\psi_a}]\frac{s_0}{2} \tag{6.37}$$

$$\tilde{\eta}_{n+} = f(\omega_n)[\kappa_g(1 + i\alpha_{gn})e^{-i\psi_g} + \kappa_a(1 + i\alpha_{an})e^{-i\psi_a}]\frac{s_0}{2}. \tag{6.38}$$

These two terms are completely determined by the structure of the laser and the average photon intensity.

Let a single detuning in the separation of modes be defined, $\delta = \omega_n - \Omega_n - (\omega_{n-1} - \Omega_{n-1})$, since for stable modelocking the detuning of the repetition rate, δ, must equal the detuning in the separation between all neighboring modes. The detuning, δ_n, of mode n with respect to Ω_n is then the detuning of the zeroth mode plus n times the repetition rate detuning, $\delta_n = \delta_0 + n\delta$. The general equation then for the nth mode with nearest neighbor coupling, for α parameters incorporated for the gain and absorber, and with geometric overlap factors included is

$$[-2i\tau_{pn}(\delta_0 + n\delta) + (1 + i\alpha_{gn})\tilde{g}_n + (1 + i\alpha_{an})\tilde{a}_n - 1]\tilde{E}_n + \tilde{s}_1(\tilde{\eta}_{n-}\tilde{E}_{n-1} + \tilde{\eta}_{n+}\tilde{E}_{n+1}) = 0. \tag{6.39}$$

Here $\tilde{s}_1 = s_1/s_0$, and the material gain bandwidth is taken into account with $\tilde{g}_n = f(\omega_n)\tilde{g}_0$, and $\tilde{a}_n = f(\omega_n)\tilde{a}_0$.

6.5 The solution of the supermode model

The coupled nonlinear equations (6.39) can be solved systematically. Also, one should solve the problem for a large enough number of equations such that the result does not depend strongly on the fact that the modes beyond those considered have been forced to have an electric field of zero. To reduce the number of parameters for the calculation, it will be helpful to transform to dimensionless parameters,

$$s = A/G, \tag{6.40}$$

$$r = \tau_a/\tau_g, \tag{6.41}$$

$$\tilde{\Delta} = \Delta\tau_g, \tag{6.42}$$

$$\tilde{s}_0 = G\tau_g s_0, \tag{6.43}$$

$$\tilde{\kappa}_g = \kappa_g/(G\tau_g), \tag{6.44}$$

and

$$\tilde{\kappa}_a = \kappa_a/(A\tau_a). \tag{6.45}$$

One may subtract out the detuning of mode zero from the set of equations (6.39). Defining a constant,

$$R = (\tilde{\eta}_{0-}\tilde{E}_{-1} + \tilde{\eta}_{0+}\tilde{E}_{+1})\frac{\tilde{s}_1}{\tilde{E}_0}, \tag{6.46}$$

$Im(R)$ is the component of detuning of the center mode due to mode coupling and $Re(R)$ is the reduction in required average gain for the center mode due to mode coupling, similar to that discussed in [22]. Taking the imaginary part of the $n = 0$ equation and subtracting it from the general mode n equation leads to

$$[-2i\tau_{pn}n\delta + (1 + i\alpha_{gn})\tilde{g}_n + (1 + i\alpha_{an})\tilde{a}_n - i(\alpha_{g0}\tilde{g}_0 + \alpha_{a0}\tilde{a}_0) - iIm(R) - 1]\tilde{E}_n +$$

$$\tilde{s}_1(\tilde{\eta}_{n-}\tilde{E}_{n-1} + \tilde{\eta}_{n+}\tilde{E}_{n+1}) = 0. \tag{6.47}$$

The net gain spectrum of the semiconductor material is concave downward and may be represented by the form $f(\omega_n) = 1/[1 + (\omega_n - \omega_0)^2/(\Delta\omega)^2]$. Since to second order, we can write $f(\omega_n) = 1 - bn^2$, we may substitute this, and since $b \ll 1$ and the coupling term is of the same order, we may ignore their product which goes like b^2. Now the general equation for mode n with center mode detuning subtracted finally becomes

$$[-2i\tau_{pn}n\delta + (\tilde{g}_0 + \tilde{a}_0)(1 - bn^2) - ibn^2(\alpha_{gn}\tilde{g}_0 + \alpha_{an}\tilde{a}_0) - 1 - iIm(R)]\tilde{E}_n +$$

$$\tilde{s}_1(\tilde{\eta}_{n-}\tilde{E}_{n-1} + \tilde{\eta}_{n+}\tilde{E}_{n+1}) = 0. \tag{6.48}$$

Considering a set of $2q + 1$ modal equations (all are complex except for the $n = 0$ equation), there are $4q + 1$ real equations and a list of $4q + 3$ unknowns including $4q + 1$ unknowns to specify the fields (we may take $\arg(\tilde{E}_0) = 0$ to define an absolute optical phase) and two other unknowns, $\tilde{g}_0$ and δ. The phase of the repetition rate is also a degree of freedom and we may specify $\arg(\tilde{s}_1) = 0$. Then, the modulation response of the laser sections can be referenced relative to the phase of the optical pulses. Since physically one considers a laser operating with a specific DC pumping (or more appropriately here, a constant average output power), one may specify a particular average cavity photon intensity for $\tilde{s}_0$. The latter two conditions, without loss of generality, reduce the number of unknowns in the field vector to $4q - 1$, making the problem completely determined. Due to the nonlinear dependence of the parameters $\tilde{g}_0, \tilde{a}_0, \delta, Im(R), \tilde{\eta}$'s, and $\tilde{s}_1$ on the vector $\vec{\tilde{E}}$, the problem remains challenging. However, the solution is vastly simplified by viewing it as an eigenvalue problem. For example, one may directly write the problem in a matrix form as below

$$\begin{bmatrix} A_{-q,-q}(\tilde{g}_0, \delta, \vec{\tilde{E}}) & A_{-q,1-q}(\tilde{g}_0, \delta, \vec{\tilde{E}}) & 0 & 0 & \cdots \\ A_{1-q,-q}(\tilde{g}_0, \delta, \vec{\tilde{E}}) & A_{1-q,1-q}(\tilde{g}_0, \delta, \vec{\tilde{E}}) & A_{1-q,2-q}(\tilde{g}_0, \delta, \vec{\tilde{E}}) & 0 & \\ 0 & A_{2-q,1-q}(\tilde{g}_0, \delta, \vec{\tilde{E}}) & A_{2-q,2-q}(\tilde{g}_0, \delta, \vec{\tilde{E}}) & & \\ 0 & 0 & A_{3-q,2-q}(\tilde{g}_0, \delta, \vec{\tilde{E}}) & \ddots & \\ \vdots & & & & \end{bmatrix} \begin{bmatrix} \tilde{E}_{-q} \\ \tilde{E}_{1-q} \\ \tilde{E}_{2-q} \\ \tilde{E}_{3-q} \\ \vdots \end{bmatrix} = 0. \tag{6.49}$$

Through multiplications of the rows by the appropriate complex factors one may also show that the problem can always be written, having a single complex eigenvalue, $\tilde{\lambda}$, in the form

$$[\mathbf{A}_m(\tilde{g}_0, \delta, \vec{\tilde{E}}) - \mathbf{I}\tilde{\lambda}]\vec{\tilde{E}}_m = 0, \tag{6.50}$$

where $\mathbf{A}_m(\tilde{g}_0, \delta, \vec{\tilde{E}})$ is a modified complex matrix and $\vec{\tilde{E}}_m$ is a modified eigenvector. The problem is more easily solved by keeping it in the form of (6.49), however. For a non-trivial eigen-solution, we require that the real and imaginary parts of the determinant of the matrix in (6.49) equal zero. This gives two conditions from which we may find a best estimate for $\tilde{g}_0$ and δ, and this was done simply through Newton's method. With this better estimate of the eigenvalue we proceed to update the relevant parameters and find a new estimate of the eigenvalue. The process is repeated as shown in Fig. 6.8 until convergence is reached. The computation gives the supermode solutions of the high-repetition-rate laser for the chosen average operating power $\tilde{s}_0$.

6.6 Results from an approximate 3-mode solution

The full numerical solution is complicated, involving a large number of interrelated parameters, and it does not quickly lead to a simple intuitive picture of the effects of the device parameters. To supplement the full numerical solution, an approximate analytical description involving only 3 modes and an approximation of the supermode symmetry is pursued. One may show that if the α parameters of the gain and absorber sections are ignored, and the gain bandwidth is symmetric relative to the cavity modes, a totally symmetric (odd symmetry) supermode solution for any number of modes will result. The form of the supermode solution will be

$$\tilde{E}_n = \tilde{E}^*_{-n}, \tag{6.51}$$

and one can always find a three-mode solution having all three modes exactly in phase. However, as soon as $\alpha_g \neq 0$ or $\alpha_a \neq 0$ is chosen, the symmetry is broken and one finds that now a chirp-free supermode solution of this form will not generally exist.

Thus no passively mode-locked supermode will exist having the form of (6.51) when the amplitude-to-phase coupling is taken into account. The relative phases of

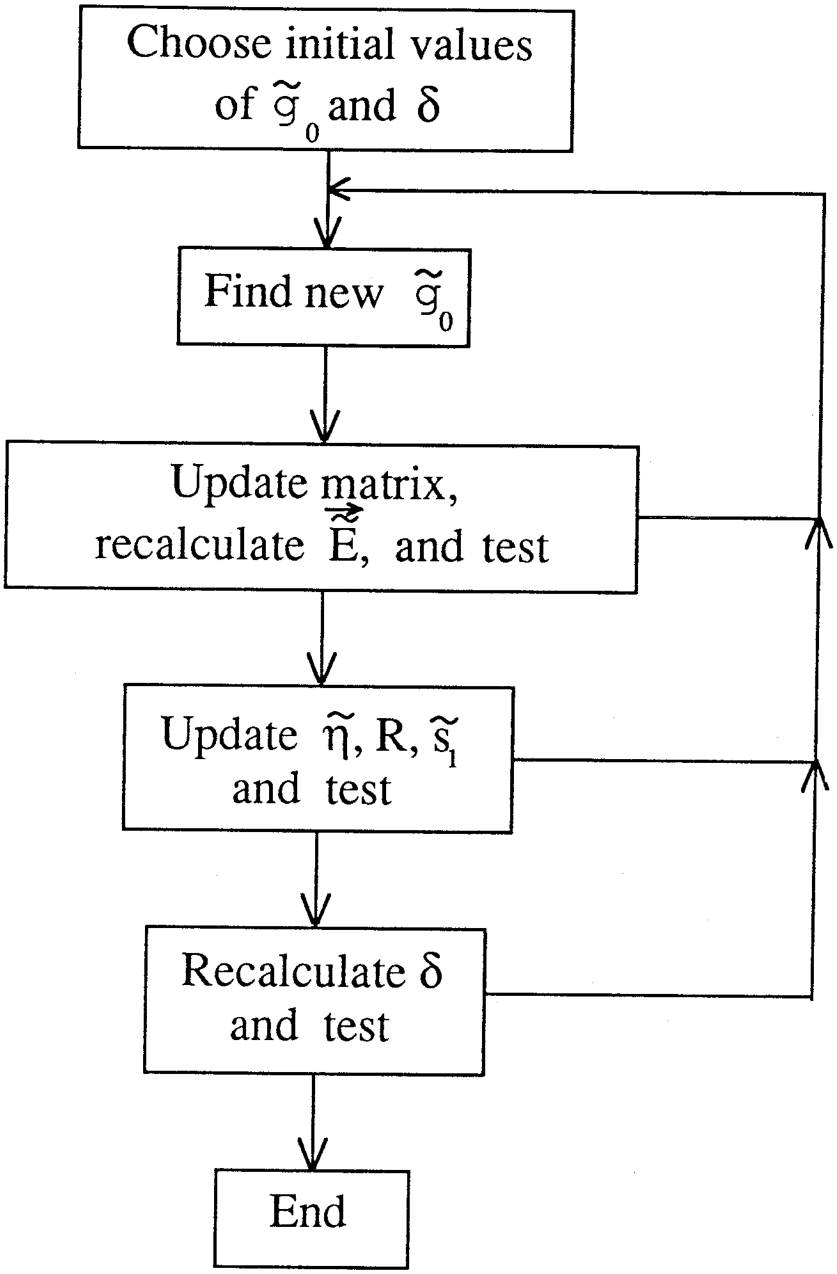

Figure 6.8: Flowchart of calculation for self-consistent supermode solution.

the modes in the supermode depend strongly on the amplitude-to-phase coupling. One finds, for numerous solutions of the full numerical analysis that once a non-zero α parameter is chosen, the solutions are of the even symmetric form

$$\tilde{E}_n \approx \tilde{E}_{-n}, \tag{6.52}$$

since phase effects resulting from the α parameter greatly outweigh the effects present when the α's were zero.

Since a simple, analytic, and reasonably accurate result can be obtained assuming (6.52) when some non-zero α is present, we derive a solution for three mode-locked modes using this even symmetric assumption. The term $-ib(\alpha_{g(\pm 1)}\tilde{g}_0 + \alpha_{a(\pm 1)}\tilde{a}_0)$ is found to have little effect on the net gain, amplitudes, or phases of the supermode and will, for this reason, be ignored in this 3-mode approximation.

From the $n = 1$ and $n = -1$ equations of (6.48), the expressions

$$\delta = \frac{Im(R)}{2\tau_p Re(\frac{\tilde{\eta}_{0+} + \tilde{\eta}_{0-}}{\tilde{\eta}_{0+} - \tilde{\eta}_{0-}})}, \tag{6.53}$$

and

$$\frac{\tilde{E}_1}{\tilde{E}_0} = \frac{i\tilde{s}_1(\tilde{\eta}_{0+} - \tilde{\eta}_{0-})}{4\tau_p \delta} \tag{6.54}$$

can be obtained. Combining this with the $n = 0$ equation, we can find the reduction in required gain for the center mode,

$$Re(R) = -(\tilde{g}_0 + \tilde{a}_0 - 1) = -Im(R)\frac{Im(\tilde{\eta}_{0+}^2 - \tilde{\eta}_{0-}^2)}{Re(\tilde{\eta}_{0+}^2 - \tilde{\eta}_{0-}^2)}. \tag{6.55}$$

From equation (6.54) we will find that a chirp-free solution will exist if

$$\tilde{\kappa}_g \alpha_g \sin \psi_g = -\tilde{\kappa}_a \alpha_a \sin \psi_a. \tag{6.56}$$

In this case, a soliton-like compensation effect occurs in the monolithic laser cavity. This condition implies that the self-phase modulation (SPM) of the absorber section may exactly oppose the SPM from the gain section [23,24]. For a larger ratio of $\alpha_g : \alpha_a$, a net upchirp (optical frequency rising with time during the pulse) due to SPM will occur. In the frequency domain picture this corresponds to a phase term, $e^{ia(\omega-\omega_0)^2}$, multiplying the optical spectrum, where a is negative. For a smaller ratio of $\alpha_g : \alpha_a$, a net down-chirp due to SPM is found to occur. A plot of chirp verses the ratio of $\alpha_g : \alpha_a$ for a specific laser operating point will be shown in the next section, using the full calculation. Evidence of both these regimes has recently been demonstrated [19].

6.7 The full supermode calculation

As formulated in section 6.6, the high-repetition-rate laser supermode can be found numerically. This may be accomplished even while eliminating all assumptions on the modal phase and removing any restrictions on the number of participating Fabry-Perot modes. One finds that if a large enough number of modes is allowed such that the outermost modes have powers of $< 10^{-6}$ compared to the strongest modes, there is little further change in the result if additional modes are included.

6.7.1 Before amplitude-to-gain coupling is included

Given reasonable parameters for laser material and structure, such as those shown in Table 6.1, one can find the supermode solution. In general, one would not expect the α parameter from the gain and absorber regions to be equal. Previously [20], the dependence of the interband transition component of this parameter has been calculated. One would expect a smaller α parameter for laser sections pumped to lower carrier densities. This, in fact, is found to be an important consideration in finding a stable supermode solution. Lau [14] has calculated supermode solutions for three modes with $\alpha = 0$ for both sections. We find reasonably good qualitative agreement with these results even as the number of modes considered is increased. The plots resulting from $\alpha = 0$, $\tilde{s}_0 = 2.5$, a 15-mode calculation, and the parameters in Table 6.1 are shown in Figs. 6.9-6.10. From here on, the frequency dependence of the cold cavity loss is neglected so $\tau_{pn} = \tau_p$. Fig. 6.9 shows the calculated field strengths for the 15-mode supermode. Fig. 6.10 shows the corresponding modal phases, where ϕ_n is defined as the optical phase in $\tilde{E}_n e^{i(\omega_n t+\phi_n)}$. Clearly, the symmetry of (6.51) is present here. Fig. 6.11 shows the threshold gain difference, $Re(R)$, as a function of $\tilde{s}_0$, defined previously and is displayed in units of 10^{-4} times the cold cavity loss (from τ_p). The right side scale of this plot shows the expected detuning, δ, of the cavity repetition rate. Fig. 6.12 shows the modulation depth at the first harmonic as a function of average intensity. The threshold gain for single mode operation must be greater than the mode-locking threshold gain, meaning $Re(R) > 0$

Variable	Symbol	Value	Units
Number of Modes Considered	$2q+1$	15	
Center Wavelength	λ	0.85	μm
Effective Index of Refraction	μ_r	3.6	
Differential Gain	G	1×10^{-15}	cm^2
Ratio of Diff. Abs. / Diff. Gain	s	2.2	
Gain Section Recovery Time	τ_g	1×10^{-9}	s
Ratio of Abs. Recov. Time / Gain Recov. Time	r	0.3	
Fundamental Repetition Rate	$\Delta/2\pi$	80	GHz
Gain Section α parameter	α_g	4	
Absorber Section α parameter	α_a	2.1	
Photon Cavity Lifetime	τ_p	10	ps
Confinement Factor	Γ	0.05	
Ratio of Absorber Length / Total Laser Length	h_a	0.25	
Normalized Unsaturated Absorption	$\tilde{a}_0'$	-2.0	
Gain Bandwidth	$\Delta\omega/2\pi$	10	THz
Coefficient for α's dependence on intensity	α_I	0.25	

Table 6.1: Parameter values used in supermode calculations.

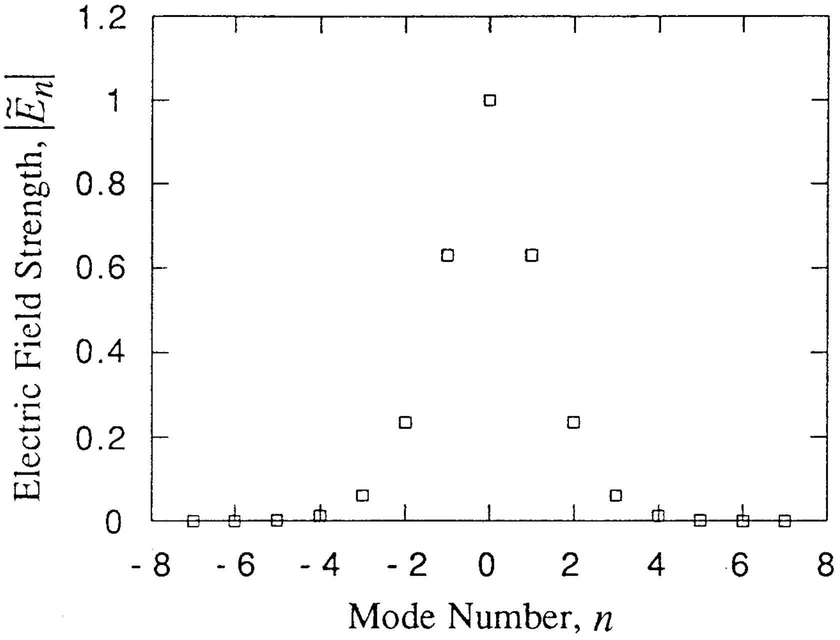

Figure 6.9: Calculated mode structure of supermode assuming no amplitude-to-phase coupling, $\alpha_g = 0, \alpha_a = 0$, $\tilde{s}_0 = 2.5$, and using the other parameter values as given in Table 6.1.

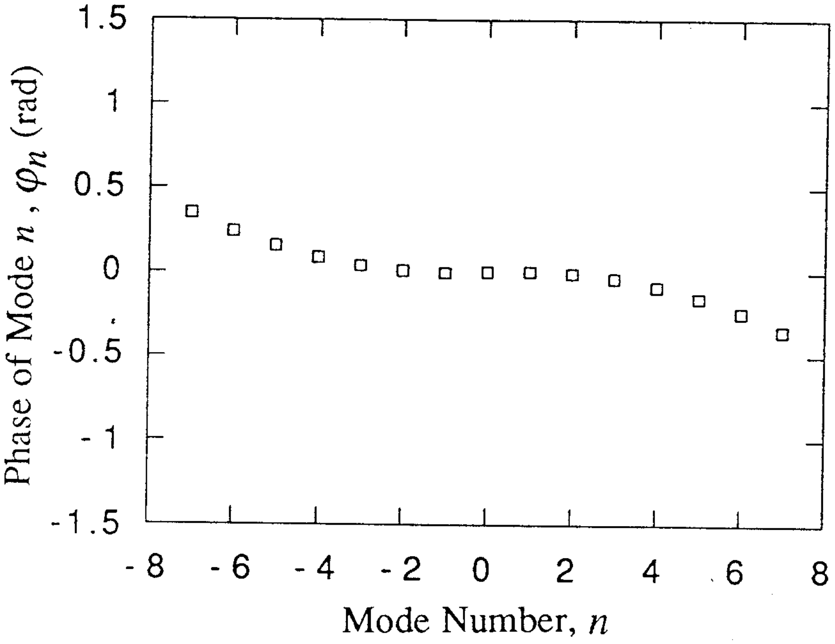

Figure 6.10: Calculated phase of the supermode assuming no amplitude-to-phase coupling, $\alpha_g = 0, \alpha_a = 0$, $\tilde{s}_0 = 2.5$, and using Table 6.1 to define all other parameters.

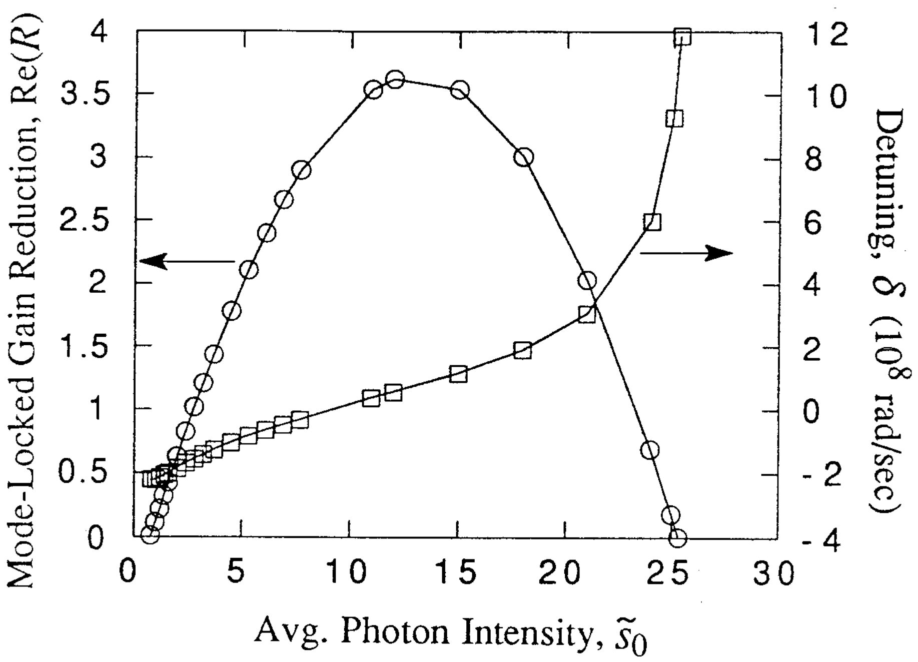

Figure 6.11: Calculated plot of $Re(R)$, the reduction in threshold gain due to mode coupling vs. average cavity intensity is plotted for $\alpha_g = 0, \alpha_a = 0$, $\alpha_l = 0$. The corresponding detuning, δ, of the repetition rate is shown on the scale at right.

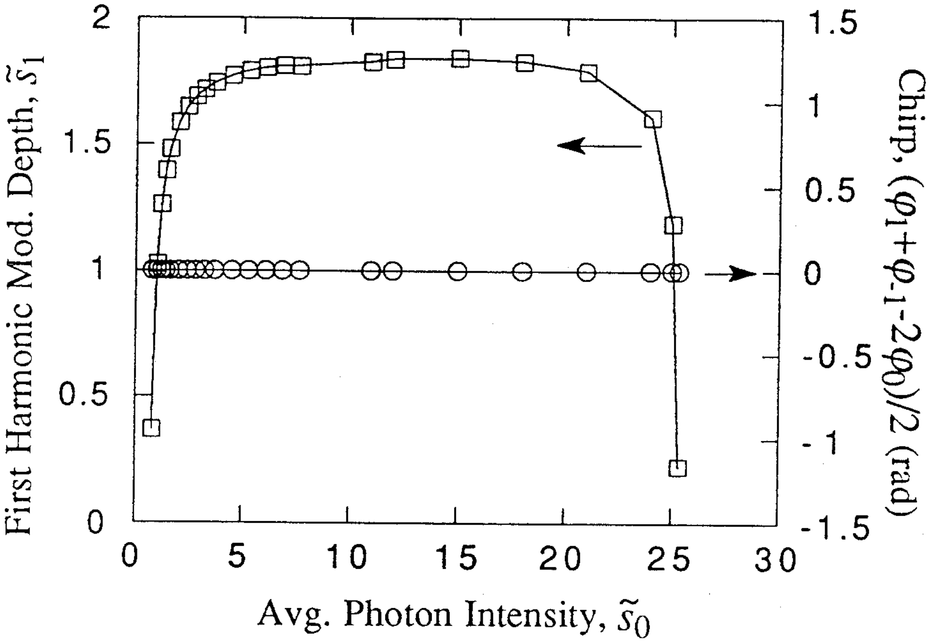

Figure 6.12: The calculated modulation depth for the signal at the first harmonic of the repetition rate is plotted for $\alpha_g = 0, \alpha_a = 0,\ \alpha_l = 0$.

for stable modelocking to be realized [14]. In ideal amplitude modulated (AM) passive modelocking, a minimum mode coupling is required in order to obtain simultaneous lasing from 3 or more modes of a homogeneously broadened laser. This requires a minimum nonlinearity to be present. Hence, if the average cavity intensity, $\tilde{s}_0$, is too low, an inadequate amount of mode coupling is generated, and mode-locked operation cannot be obtained. Additionally, if the cavity intensity is large such that the absorber is strongly saturated to a point far beyond the knee of the nonlinearity, the minimum mode coupling again cannot be obtained. This explains why modelocking may only be obtained over a finite range in Fig. 6.11. The right scale in Fig. 6.12 shows in this case where $\alpha_g = 0$ and $\alpha_a = 0$, one does not expect SPM to generate any pulse chirp effects and the quadratic phase $(\phi_1 + \phi_{-1} - 2\phi_0)/2 = 0$ indicates that, to first order, no linear chirp is present in this case.

6.7.2 Including amplitude-to-gain coupling

As discussed in the previous section, the α parameter can have a large effect on the phase of each optical mode. Assuming an α parameter of $\alpha_g = 4$ for the gain section, only a limited range of values for α_a, the α parameter for the absorber section, was found to give stable self-consistent solutions. A calculation of the approximately linear chirp (quadratic phase) at the center of the optical spectrum, $(\phi_1 + \phi_{-1} - 2\phi_0)/2$, versus α_a/α_g is plotted in Fig. 6.13 for the range of stable mode-locked solutions. The range is quite narrow and corresponds to a region where the SPM effects from absorber and gain nearly cancel as discussed in [19]. The dependence of the α's on

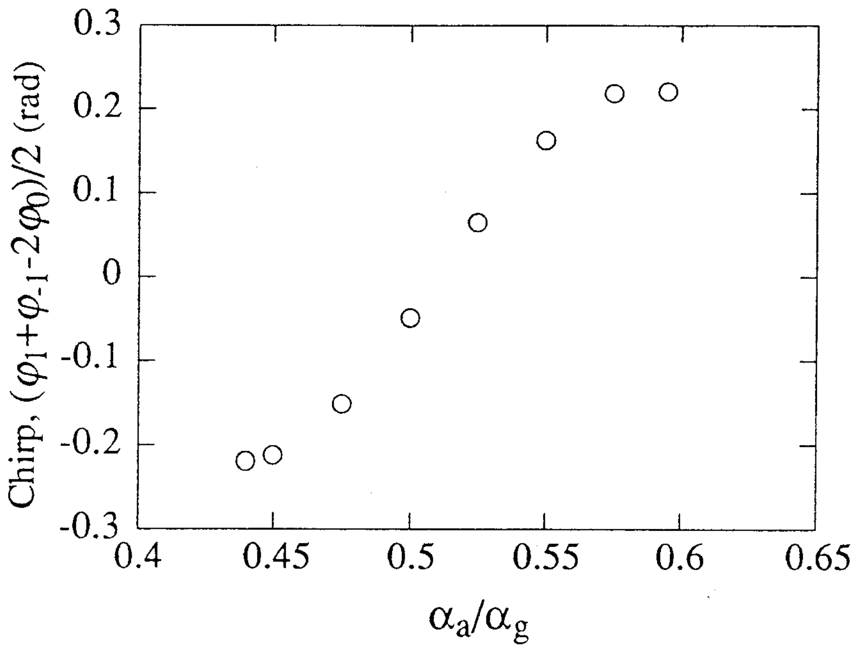

Figure 6.13: A calculation of the linear chirp, the quadratic phase around the center of the optical spectrum, for different values of α_a/α_g.

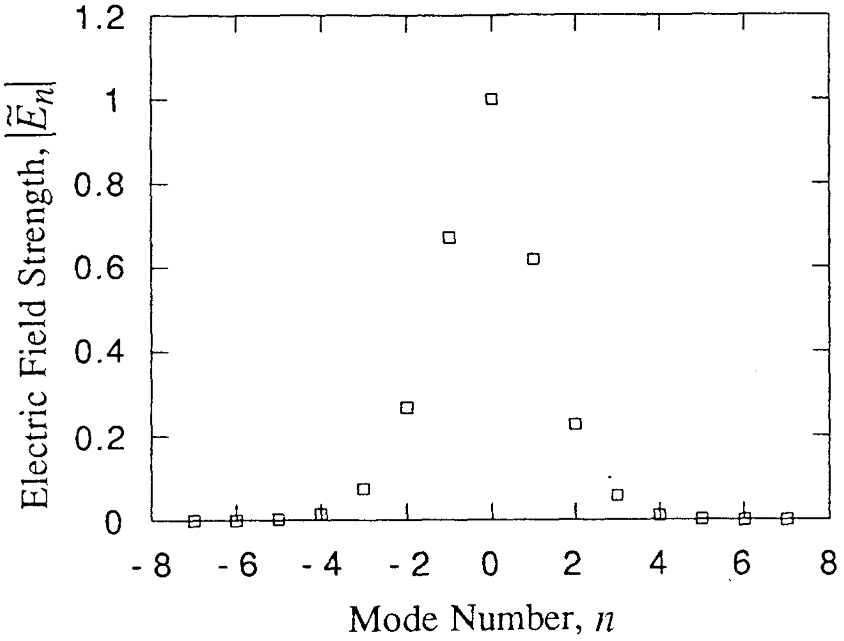

Figure 6.14: Calculated mode structure of supermode when allowing amplitude-to-phase coupling, $\alpha_g = 4, \alpha_a = 2.1$, and $\tilde{s}_0 = 2.5$. Parameters are exactly as shown in Table 6.1.

frequency is ignored in this and subsequent plots.

The same plots as shown in Figs. 6.9-6.12 can be shown for the case including effects of reasonable non-zero α's. The new calculated field strength for the 15-mode supermode with $\alpha_g = 4$ and $\alpha_a = 2.1$ is shown in Fig. 6.14. Fig. 6.15 shows the corresponding modal phases, ϕ_n. The previously discussed change in supermode symmetry is mainly shown in this plot of ϕ_n. Before discussing the other three plots, it should be mentioned that physically as the gain current in the laser is increased to raise the average intensity, $\tilde{s}_0$, one weakens the absorber section through the relation

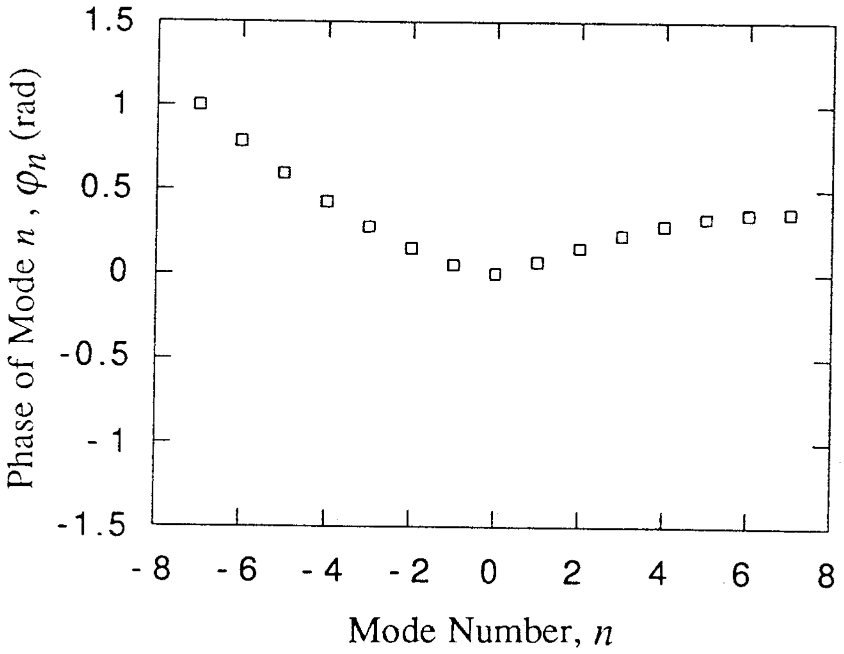

Figure 6.15: Calculated phase of supermode when allowing amplitude-to-phase coupling, $\alpha_g = 4, \alpha_a = 2.1$. Parameters are exactly as shown in Table 6.1.

$\tilde{a}_0 = \tilde{a}'_0/(1 + rs\tilde{s}_0)$, where $\tilde{a}'_0$ is the section's normalized unsaturated absorption. The strength of the gain is also weakened since we require that $\tilde{g}_0 + \tilde{a}_0 - 1 \approx 0$. Thus, the two sections both operate closer to transparency as $\tilde{s}_0$ is increased. This implies a change in each section's α parameter also occurs and their dependence on $\tilde{s}_0$ will be approximated to first order here by $\Delta\alpha_g = -\alpha_l\Delta\tilde{s}_0$ and $\Delta\alpha_a = \alpha_l\Delta\tilde{s}_0$, where α_l takes into account a linear decrease (increase) in α_g (α_a) as the cavity intensity is increased. Here, α_l is taken as 0.25 around the point $\tilde{s}_0 = 2.5$.

Fig. 6.16 shows the plot of required gain reduction, $Re(R)$, and the expected detuning in the repetition rate as a function of $\tilde{s}_0$. Fig. 6.17 shows the modulation depth and an estimate of the mode-locked laser's linear chirp $(\phi_1 + \phi_{-1} - 2\phi_0)/2$. One can see that the expected mode-locking range over which the coupled equations can be simultaneously satisfied is severely limited when the phase condition including the α parameter is considered. This is a direct result of the presence of the α parameters in the coupling terms and occurs consistently regardless of whether or not one includes more allowed modes in the calculation.

It is expected that the mode-locked laser's operation will change if one modifies the structure or bias parameters. These effects are important if one intends to understand or optimize the laser's operation. We have calculated results one would expect from modifying key laser parameters and using the nearest-neighbor mode coupling approximation for the range of supermode solutions that exist around the case considered in Fig. 6.14.

One finds that if s, the ratio of the differential absorption to differential gain is

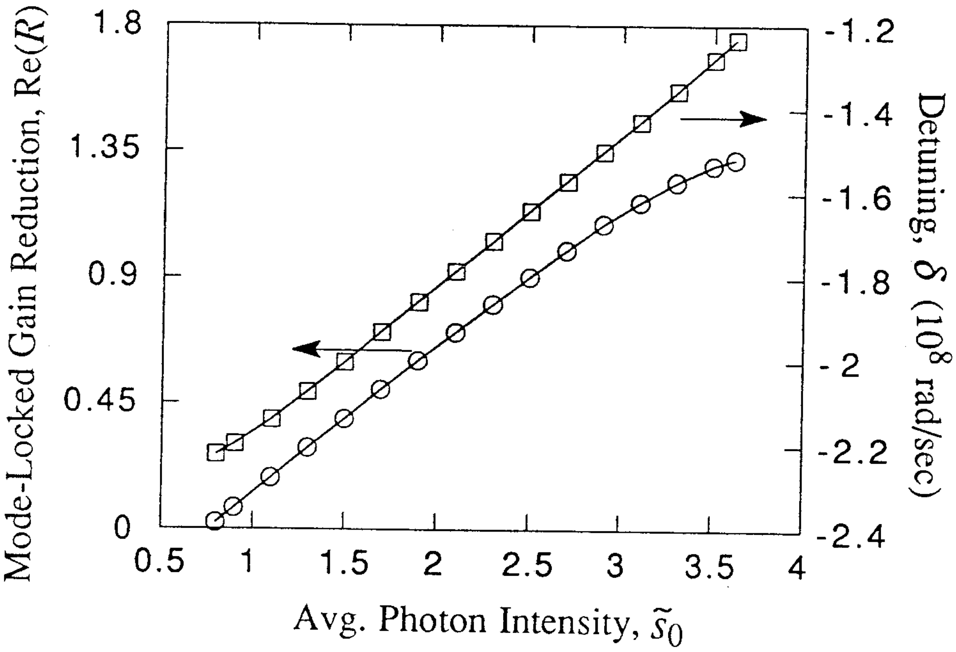

Figure 6.16: Calculated plot of $Re(R)$, the reduction in threshold gain due to mode coupling vs. average cavity intensity is plotted for $\alpha_g = 4, \alpha_a = 2.1$. The corresponding detuning of the repetition rate is shown on the scale at right.

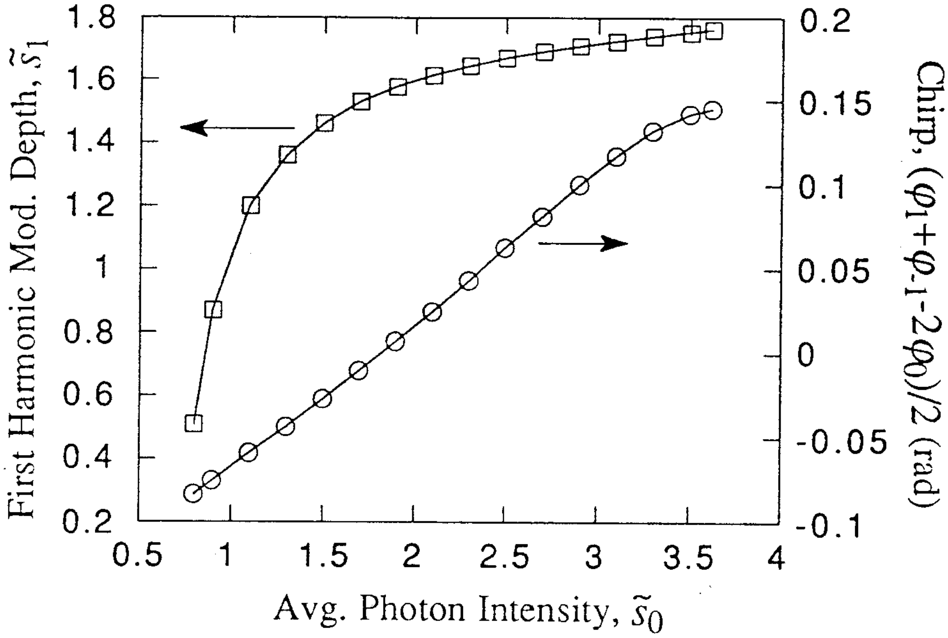

Figure 6.17: The calculated modulation depth for the signal at the first harmonic of the repetition rate is plotted for $\alpha_g = 4, \alpha_a = 2.1$. The corresponding linear chirp, $(\phi_1 + \phi_{-1} - 2\phi_0)/2$ is shown on the scale at right.

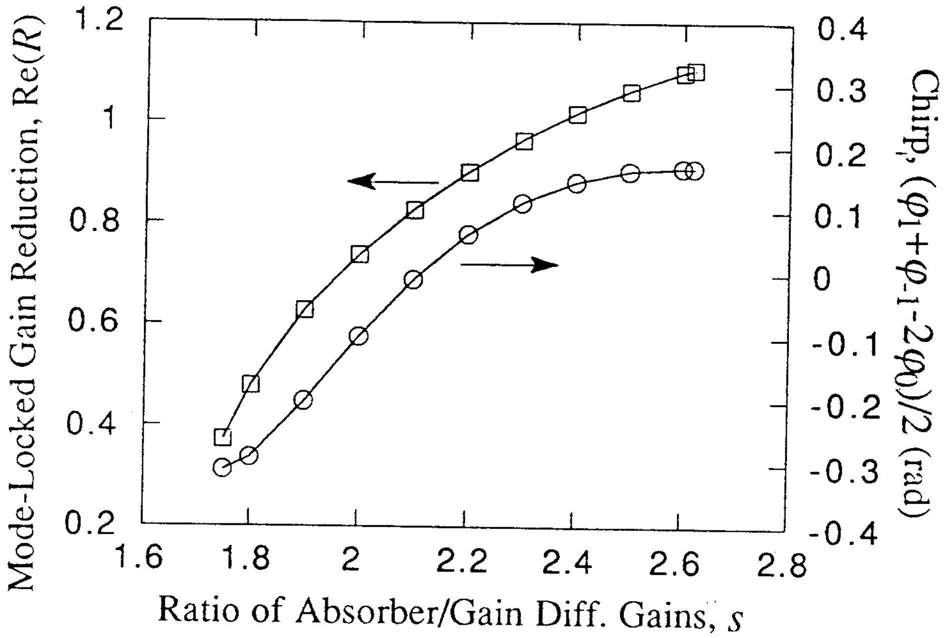

Figure 6.18: The calculated variation of $Re(R)$, the reduction in threshold gain due to mode coupling, plotted against s, the ratio of differential absorption to differential gain.

increased, a larger mode coupling is obtained. This leads to a larger value of $Re(R)$, the reduction in the mode-locking threshold relative to the single mode threshold, as shown in Fig. 6.18, which is expected to lead to a more stable mode-locked supermode. Fig. 6.18 also shows that a decreased up-chirp or increased down-chirp is expected to occur if a larger s is present and all other parameters are unchanged.

The effect of r, the ratio of absorber recovery time to gain recovery time, is expected to be nearly the opposite. Shown in Fig. 6.19, an increased r leads to a decrease in the mode-locked gain reduction and ultimately a loss of a stable mode-locked so-

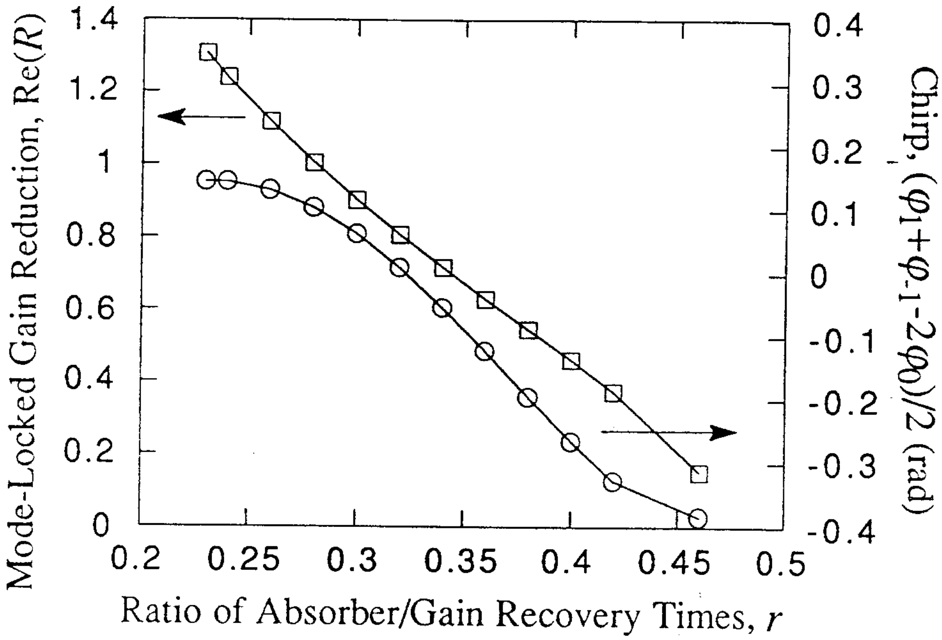

Figure 6.19: The calculated variation of $Re(R)$, the reduction in threshold gain due to mode coupling, plotted against r, the ratio of absorber recovery time to gain recovery time.

lution altogether as the ratio is increased above $r = 0.46$ in this case. Simultaneously the increased value of r will lead to an increased up-chirp as shown in Fig. 6.19. It is known that one can reduce the value of r through stronger reverse bias or ion implantation into the absorber section.

An increase in $\tilde{a}'_0$, the unsaturated absorption strength of the saturable absorber, is shown to lead (as shown in Fig. 6.20) to an increase in the mode-locked gain reduction, $Re(R)$. The strength of the unsaturated absorption is proportional to this section's length and absorption coefficient. An increase in either of these is expected

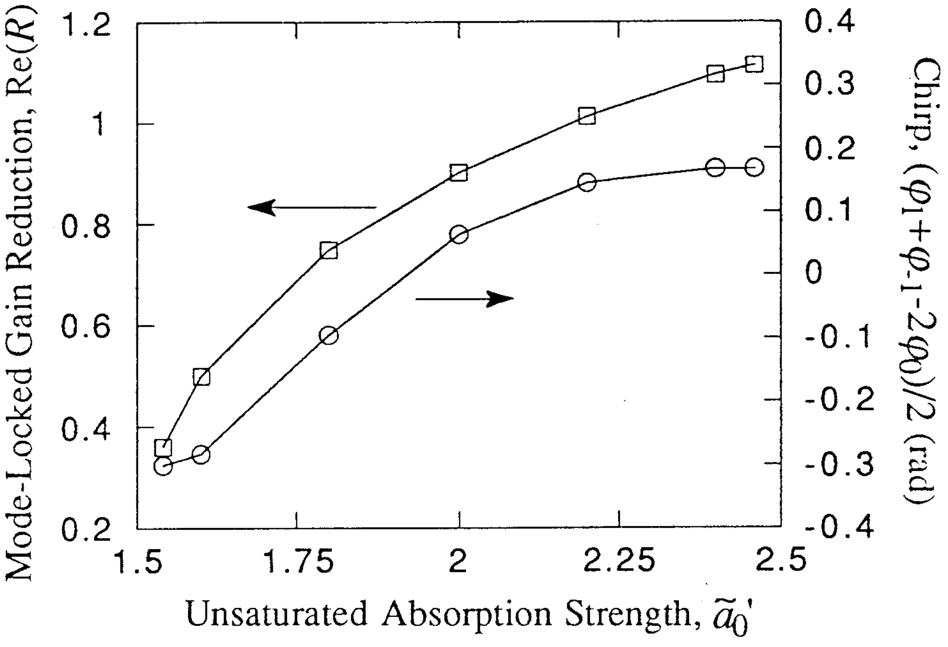

Figure 6.20: Calculated value of $Re(R)$, the reduction in threshold gain due to mode coupling, plotted against $\tilde{a}_0'$, unsaturated absorption strength.

to lead to a more strongly down-chirped pulse as shown in Fig. 6.20. This agrees with expectations described in [19] where a stronger saturable absorber is cited as the reason for a significant down-chirp being obtained over most of the experimental chirp-versus-current curve.

The ratio of the physical length of the absorber to the total laser length, h_a, is expected to change the effectiveness of mode coupling. If the same absorber strength can be incorporated into a smaller segment of the laser, one can achieve a more effective mode coupling and obtain a larger mode-locked gain reduction, $Re(R)$. This is consistent with results determined in [25]. Fig. 6.21 also shows the effects on pulse chirp when the parameter h_a is varied.

The mode-locked laser's round-trip frequency is determined by the laser's cavity length. A larger cavity round-trip frequency is expected to result in reduced mode coupling due to a reduction in κ_g and κ_a. This will eventually lead to a point where the minimum mode coupling cannot be obtained and no stable mode-locked supermode exists. Although the point is $\approx$ 105 GHz in this case (Fig. 6.22), using larger values of s (≈ 5), we have obtained stable supermode solutions slightly beyond 200 GHz. This agrees well with the theoretical results presented by Lau [14]. In this case, larger mode coupling effects resulted in a reduced down-chirp.

As intuitively expected, lasers having a larger gain and absorber bandwidth will obtain a greater mode-locked gain reduction. Fig. 6.23 shows the expected increase in $Re(R)$ as one solves the supermode equations allowing successively larger material bandwidths. Even larger advantages are found to occur if one assumes a gain band-

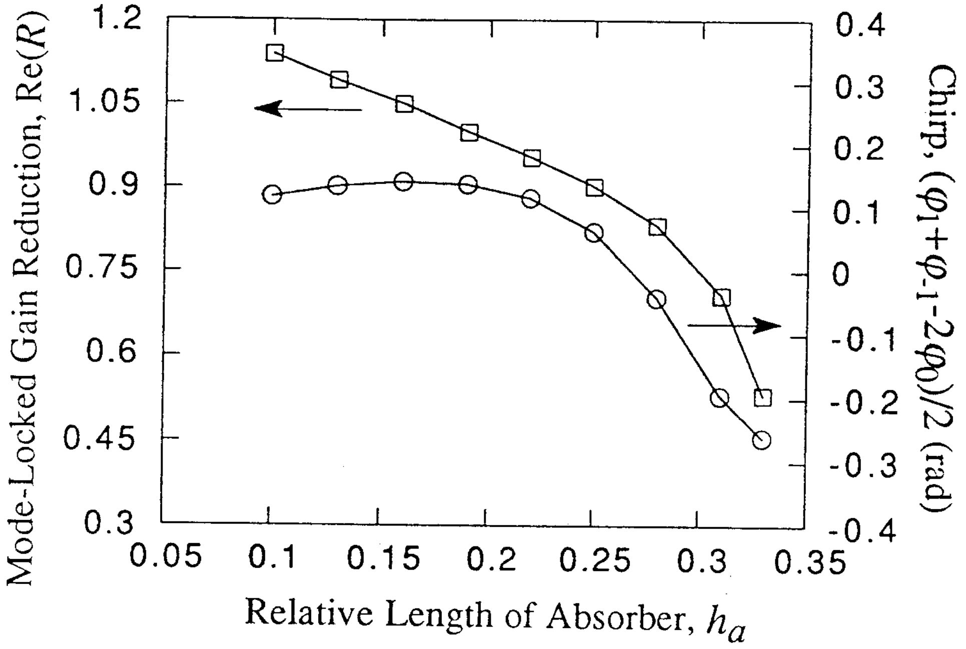

Figure 6.21: Calculated value of $Re(R)$, the reduction in threshold gain due to mode coupling, plotted against h_a, the physical length of the absorber as a fraction of the laser's full length.

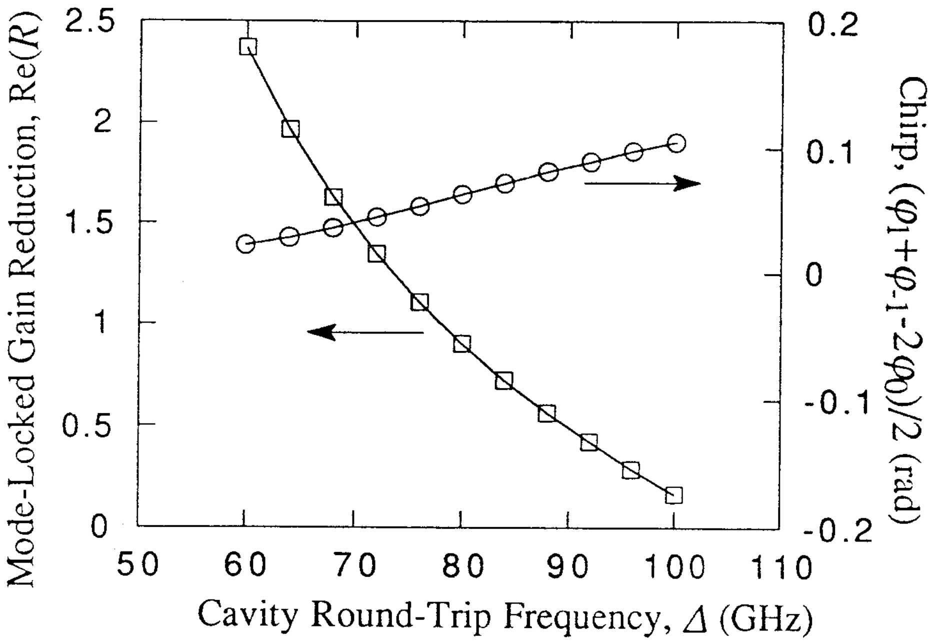

Figure 6.22: Calculated value of $Re(R)$, the reduction in threshold gain due to mode coupling, plotted against Δ, the repetition rate.

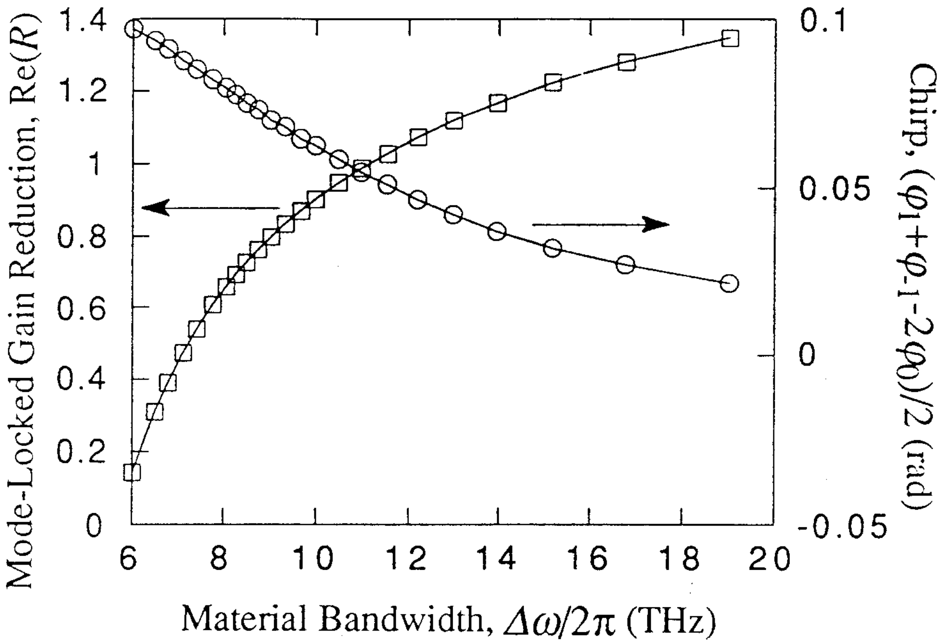

Figure 6.23: Calculated value of $Re(R)$, the reduction in threshold gain due to mode coupling, plotted against $\Delta\omega$, material bandwidth.

width wider than the laser's absorption bandwidth. An expected decreased pulse chirp for larger material bandwidth is also shown in Fig. 6.23.

References

[1] H. A. Haus, *IEEE J. Quantum Electron.*, **11**, 736 (1975).

[2] H. A. Haus, *IEEE J. Quantum Electron.*, **11**, 323 (1975).

[3] V. S. Letokhov, *J. Appl. Phys.*, **39**, 3318 (1968).

[4] E. M. Garmire and A. Yariv, *IEEE J. Quantum Electron.*, **3**, 222 (1967).

[5] J. B. Gunn, *IEEE J. Quantum Electron.*, **5**, 573 (1969).

[6] G. H. C. New, *IEEE J. Quantum Electron.*, **10**, 115 (1974).

[7] Y. K. Chen and M. C. Wu, *IEEE J. Quantum Electron.*, vol. 28, **2176** (1992).

[8] E. M. Garmire and A. Yariv, *IEEE J. Quantum Electron.*, **3**, 222 (1967).

[9] O. E. Martinez, R. L. Fork, and J. P. Gordon, *J. Opt. Soc. Am. B*, **2**, 753 (1985).

[10] J. C. Chen, H. A. Haus, and E. P. Ippen, *IEEE J. Quantum Electron.*, **29**, 1228 (1993).

[11] O. P. McDuff, *IEEE J. Quantum Electron.*, **3**, 101 (1967).

[12] A. E. Siegman, **Lasers**, ch. 24, University Science Books, Mill Valley, CA (1986).

[13] M. Sargent, M. O. Scully, and W. E. Lamb, **Laser Physics**, ch. 8, Addison-Wesley Publishing Co., Reading, MA (1974).

[14] K. Y. Lau, *IEEE J. Quantum Electron.*, **26**, 250 (1990).

[15] P. P. Vasil'ev and A. B. Sergeev, *Electron. Lett.*, **25**, 1049 (1989).

[16] S. Sanders, L. Eng, J. Paslaski, and A. Yariv, *Appl. Phys. Lett.*, **56**, 310 (1990).

[17] S. Arahira, S. Oshiba, Y. Matsui, T. Kunii, and Y. Ogawa, *Appl. Phys. Lett.*, **64**, 1917 (1994).

[18] J. H. Zarrabi, E. L. Portnoi, and A. V. Chelnokov, *Appl. Phys. Lett.*, **59**, 1526 (1991).

[19] R. A. Salvatore and A. Yariv, "Demonstration of down-chirped and chirp-free pulses from high-repetition-rate passively mode-locked lasers," to be published in *IEEE Photon. Technol. Lett.*, **7**, Oct. (1995).

[20] K. Vahala, L. C. Chiu, S. Margalit, and A. Yariv, *Appl. Phys. Lett.*, **42**, 631 (1983).

[21] A. Dienes, J. P. Heritage, M. Y. Hong, and Y. H. Chang, *Opt. Lett.*, **17**, 1602 (1992).

[22] J. Paslaski and K. Y. Lau, *Appl. Phys. Lett.*, **59**, 7 (1991).

[23] V. Petrov and T. Mirtchev, *Optical and Quantum Electron.*, **23**, 1161 (1991).

[24] G. P. Agrawal and N. A. Olsson, *IEEE J. Quantum Electron.*, **25**, 2297 (1989).

[25] S. Sanders, *Ph.D. Thesis*, California Institute of Technology (1991).

Chapter 7

Experimental results from high-repetition-rate passively mode-locked lasers

Presentation of a bold new theoretical analysis is useless unless it can aid our understanding or give good agreement with the actual experimental devices it is intended to model. In this chapter, we hope to show that the theoretical model developed in chapter 6 fills both these demands. First, the monolithic device structures will be described. Results from devices showing stable high-repetition-rate modelocking will be given. Then, agreement between experiment and theory will be discussed.

7.1 Structure of monolithic devices

A variety of monolithic devices were fabricated. Detailed information about all the different fabricated structures involved would require a full chapter, therefore, we will only briefly summarize the structures that led to the most stably mode-locked results and the reader will be referred elsewhere for more details about other fabricated structures. All the results to be presented in this chapter came from two structures: those from regrown two-section GaAs lasers from Ortel Corporation (similar to regrown lasers described in chapter 3) and those from colliding-pulse mode (CPM) stripe GaAs lasers fabricated in our facilities at Caltech.

7.1.1 Regrown two-section monolithic GaAs lasers

The regrown two-section monolithic GaAs lasers are similar in all but one major respect to those described in chapter 3. The monolithic lasers have high reflection coatings on both facets and are therefore set up without an external cavity. Those monolithic lasers with about 30% power reflectivities or less are typically prone to self pulsation when operated with no external cavity [1,2]. The high reflection (HR) coatings are created from multilayer quarter wavelength, $\lambda_0/4n$, coatings. These have been provided mainly from Silicon oxide (SiO_2) and Aluminum oxide (Al_2O_3) through Dr. T. R. Chen at Ortel Corporation and in some cases from SiO_2 and Silicon nitride (Si_3N_4) through Prof. Axel Scherer at Caltech. Typical coatings involve between 2 and 6 layers and give between 65 and 90% power reflectivity. Thresholds for the regrown structures are as low at 5-10 mA with the very low thresholds being due to the regrown structure's superior carrier and optical confinement. The onset of stable modelocking tends to be about 15 mA in our best devices.

7.1.2 Stripe CPM lasers

As mentioned previously, these stripe CPM devices were totally grown and processed within Caltech. This allows added flexibility to customize the laser structures for the monolithic mode-locking applications. By placing the absorbing section directly in the middle of the cavity, one can obtain an advantage over the two-section devices that do not have perfect reflection on their absorber facet. The first CPM mode-locked laser was made from a dye laser in 1981 [3]. The CPM laser is meant to operate in such a way that two pulses exist in the laser and saturate the absorber simultaneously. By operating in this manner, a stronger absorber saturation can be achieved for the same average power. This may upon first expectation appear to give a factor-of-two larger saturation effect within the absorber since, due to spatial beats, only half of the absorber media is exercised. The more exact saturation advantage calculation demonstrates that the effect is even more significant than that over operation without pulses colliding in the absorber [4]. This calculation which considers the coherent counter-propagating field coupling and assumes pulse widths temporally shorter than diffusion effects shows that a 3 to 1 absorber saturation advantage is obtained by designing the cavity such that the pulses meet within the absorber. This would equivalently be modelled by assuming a tripling of the differential absorption

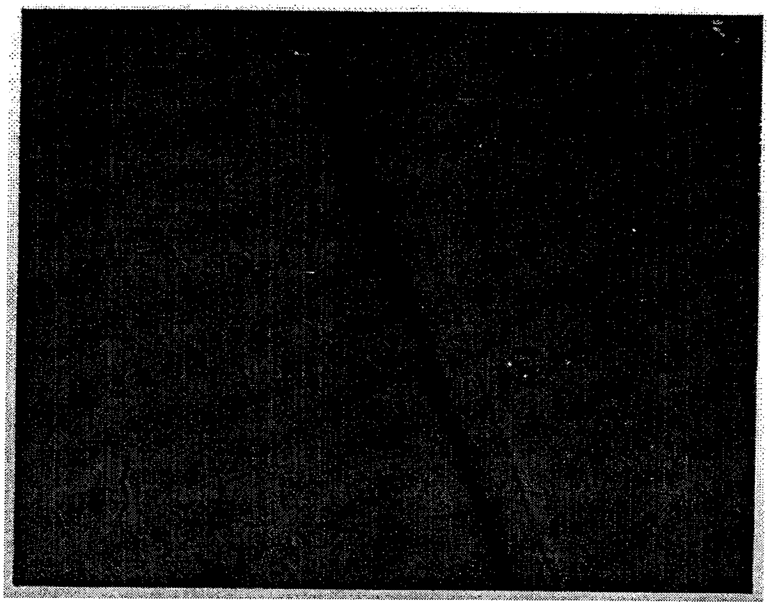

Figure 7.1: The top side of a GaAs wafer showing one ridge. To create stripe lasers, ridges of slightly less than 3 μm width and slightly more than 1 μm in height are etched uniformly across the wafer.

($A \rightarrow 3A$) in chapter 6 (or a 3/2 increase over that expected from the case of no transient material gratings from the steady state). In addition the transient material gratings are proposed to enhance noise performance of the mode-locked laser due to the coherent coupling between pulses [5]. However, incomplete mode suppression effects are suspected to reduce this noise advantage of the CPM effect and perhaps sometimes turn it into a disadvantage.

Separate laser contact sections were fabricated on top of a 2-3 μm ridge material as shown in Fig. 7.1. The main photolithographic mask used to make the three-section structure for the CPM lasers is shown in Fig. 7.2. It permits large (≥ 100 μm) pads intended for easy electrical contacting, an absorber region of 50 μm, and gain regions of up to 985 μm in length each with 15 μm spacing longitudinally between each contact giving it a pattern repetition period of 1065 μm. By appropriately cleaving the fully processed wafer one can produce laser devices with the absorber in the center. A diamond-tipped Kulicke and Soffa scribing system was used to accurately place a scribe transversely across part of the wafer to obtain accurate cleavage points. It was found that accuracies better than ± 10 μm could routinely be obtained and were adequate for CPM devices. The *n* contact of the cleaved laser bars was subsequently mounted with a conductive Indium alloy on Gold plated laser mounts.

7.1.3 Measurement of high-repetition-rate pulses from CPM lasers

About 10% of the numerous CPM lasers fabricated within the group actually displayed stable modelocking. Most lasers were deemed to have insufficient mode coupling (as defined in chapter 6) for their cavity round-trip frequency and would only operate in CW or self-pulsed modes as determined through streak camera and autocorrelation analysis. Many had thresholds that were excessive and could not be adequately tested due to the laser heating damage. Decent lasing thresholds for the stripe CPM lasers was typically 30 mA. A light versus injection current (L-I curve) for a CPM laser of 570 μm total length equally pumped at all contacts is shown in

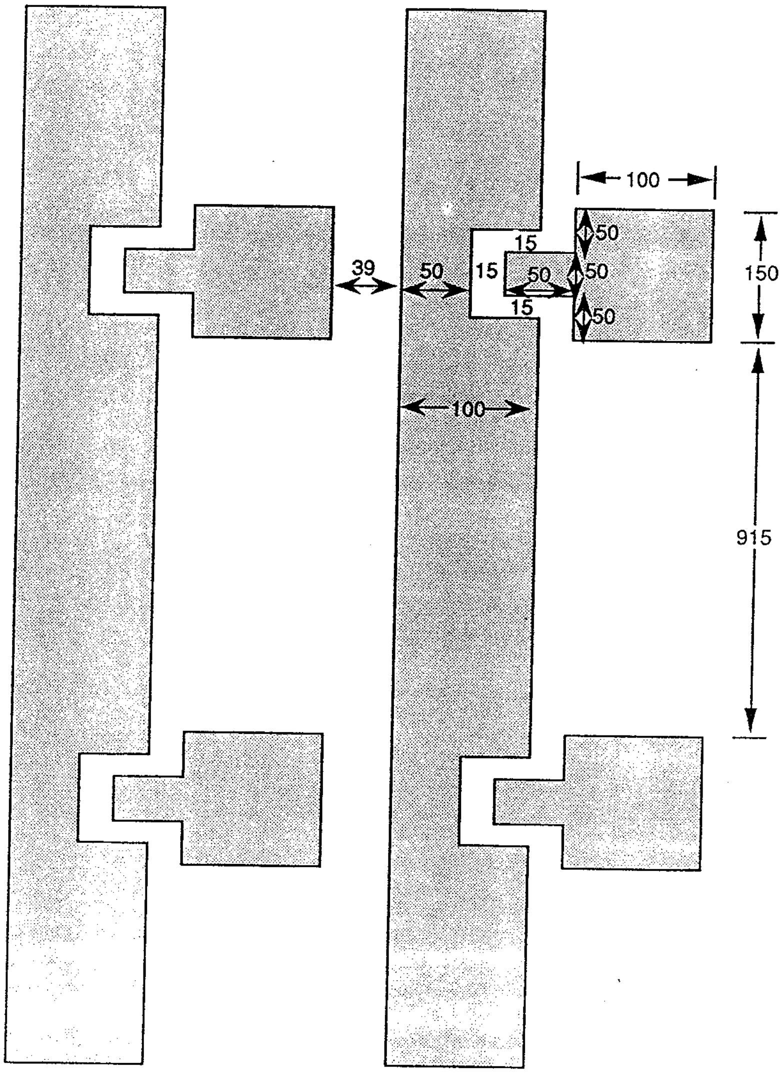

Figure 7.2: The mask which defines the contacts for the CPM laser fabrication.

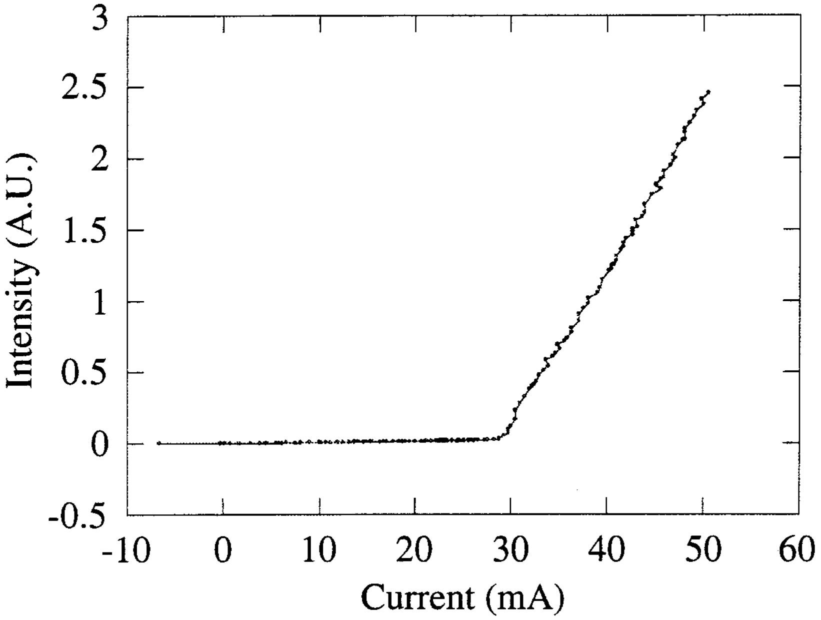

Figure 7.3: An L-I curve for all sections of the CPM laser equally pumped.

Fig. 7.3. Cavity lengths from about 1.4 mm down to as short as 400 μm total length have been fabricated. Under CPM operation, two pulses exist simultaneously in the cavity, therefore the expected repetition rate or mode spacing frequency is $c/(n_{gr}l_z)$ or in other words twice the expected cavity Fabry-Perot mode spacing. This means that under ideal CPM operation, every other mode is suppressed. It is not a priori known which set of modes will be suppressed and which will lase, however, once one set dominates, there is a bistability on the order of 0.5 mA in the L-I curve which exists and permits the laser to maintain stable operation until conditions change by at least some minimal amount to overcome the stability. If every other mode is not significantly suppressed then one cannot conclude that the pulses have a fundamental

repetition rate of $c/(n_{gr}l_z)$ or even that the pulses of this frequency are truly equally spaced. Otherwise, if the mode suppression is for all purposes complete, then the steady-state operation is equivalent to a two-section laser having a perfect (100%) HR coating on its absorber facet and having exactly half the length of the actual CPM laser. Therefore, the steady-state model in the previous chapter will apply directly to the CPM structure also.

There is a trade off in the advantages for high-repetition-rate modelocking versus the number of quantum wells. As mentioned in chapter 3, one can obtain the broadest modal gain spectrum from single well material since maximum cavity gain becomes much more on-par with the cavity losses and requires a higher volumetric carrier density. However, as seen in the previous chapter, the coupling strengths κ_a and κ_g must satisfy a minimum magnitude requirement, and are proportional to the modal differential gain which is proportional to the number of quantum wells. Thus, a higher number of quantum wells is necessary for high-repetition-rate modelocking. Too many quantum wells means an excessive current density will be needed in these structures which are already nearing the limits of heat sinking. The optimum number of quantum wells for the monolithic laser structures with these cavity losses is determined to be about 3 or 4 quantum wells.

We have achieved mode-locked pulse trains at frequencies up to 180 GHz. Unfortunately, the train, as seen through streak camera measurements was not consistent for all times. The laser did not undergo stable modelocking for CW current injection. Instead the pulse train disappeared and reappeared as is common with lasers having self pulsing as the envelope on top of the mode-locked pulse train. Most hopeful applications of passively mode-locked lasers more stringently require the pulse train to be continuous. Therefore only results satisfying this requirement will be presented in this thesis.

The highest repetition rate from stably mode-locked pulse trains from our CPM devices was 126 GHz. In the case of this high-repetition-rate modelocking only a few modes are present in the optical spectrum, and each of these modes is easily resolvable with a spectrometer. If the modes of the optical spectrum were all in phase, time-bandwidth-limited pulses would be obtained, however, measurements seem to indicate even in these small energy pulses, the SPM effects are important and cause noticeable chirp in the pulses. This is not surprising since the ratio of gain or loss saturation effects to SPM effects is still of the same order even though pulses may be a factor of 100 smaller in energy than they were in the external cavity laser.

A measured pulse train from streak camera measurements for a laser having 250 μm long gain contacts and therefore a total length of 570 μm is shown in Fig. 7.4. For this measurement, the gain current was 112 mA and the absorber bias was –0.84 V. It shows a distinctly periodic pattern of pulses spaced by about 8 ps (more precisely at 126 GHz), and the average pulse width from this measurement was found to be 2.9 ± 1.0 ps. From these results one finds that the group index corresponds to $n_{gr} = 4.16$. which is a reasonable value. At these low pulse energies and high repetition rates, streak camera measurements (especially at 0.85 μm or longer wavelength) are much noisier than the actual pulse trains. These pulses are also approximately at the limit

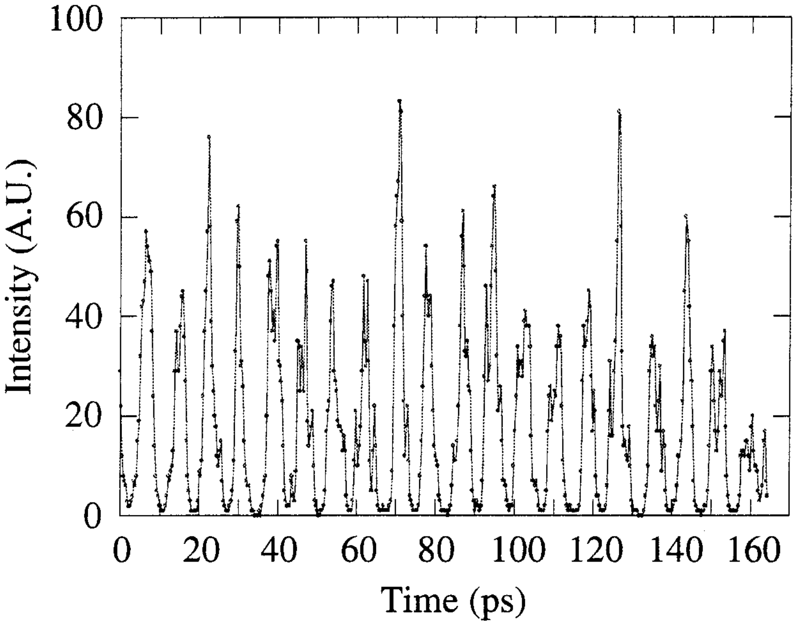

Figure 7.4: A single shot streak camera trace showing the intensity of the CPM pulse train having a repetition rate of 126 GHz.

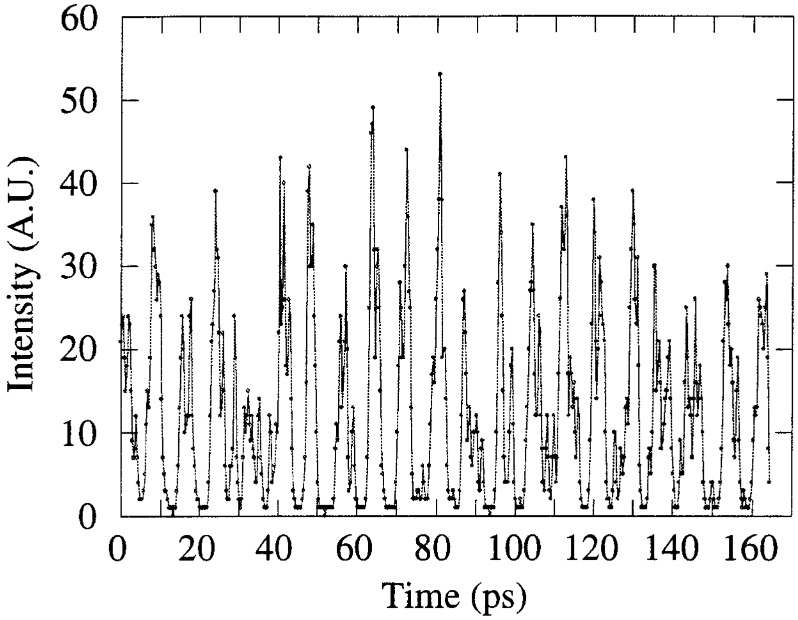

Figure 7.5: A single shot streak camera trace showing a second point within the regime of stably mode-locked CPM pulse trains having a repetition rate of 126 GHz.

of our streak camera's quoted 2 ps resolution limit.

For a significant region in the range of gain currents and absorber voltages, one can obtain stably mode-locked pulse trains. For the same laser but with a smaller gain current of 103.8 mA and a bias across the absorber section of −1.13 V a second trace of the pulse train is shown in Fig. 7.5. As one goes to lower currents, the laser will stop lasing as it is unable to achieve the necessary bleaching of the absorber. However, before that happens, or with simultaneous reduction of the absorber reverse bias, one typically reaches a regime where the laser self pulsates. Firstly, one notices (through the electrical current alone) that when the laser leaves the mode-locked regime, there

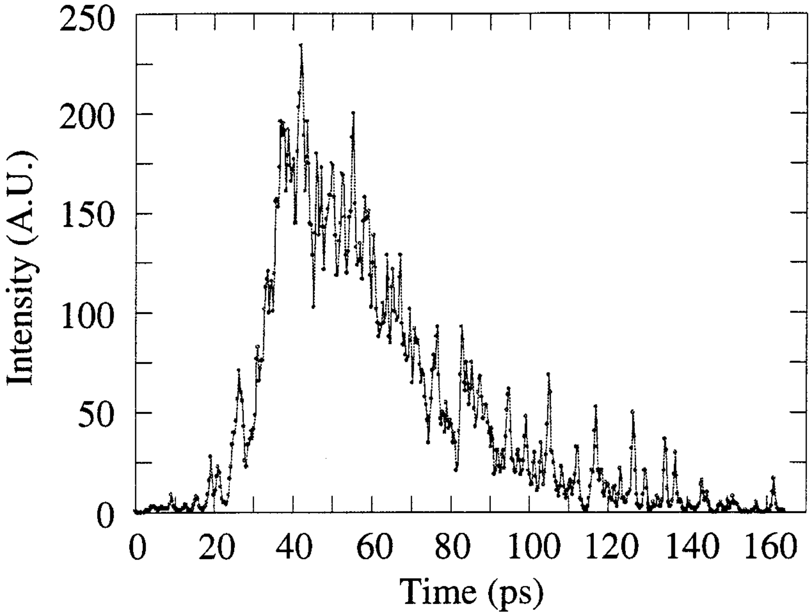

Figure 7.6: A streak camera trace showing the intensity of a single self pulsation in a consistent train of self pulsations from the CPM laser driven with a gain current below the regime of modelocking.

is an abrupt drop in the DC current drawn from the voltage source supplying the absorber section. This is due to the fact that less of the rapid exponential recovery per unit time occurs for low-repetition-rate pulses. Self pulsations typically occur at the rate of about 1 GHz in these monolithic semiconductor lasers. Data was taken to capture the consistent self pulsation that occurs in these lasers at current levels beneath that necessary for modelocking. Fig. 7.6 shows a detailed graph of a single self pulsation with a FWHM of about 40 ps. In this case the gain current was 85.4 mA, and the absorber bias was −2.2 V (with absorber current being only −14.2 mA as

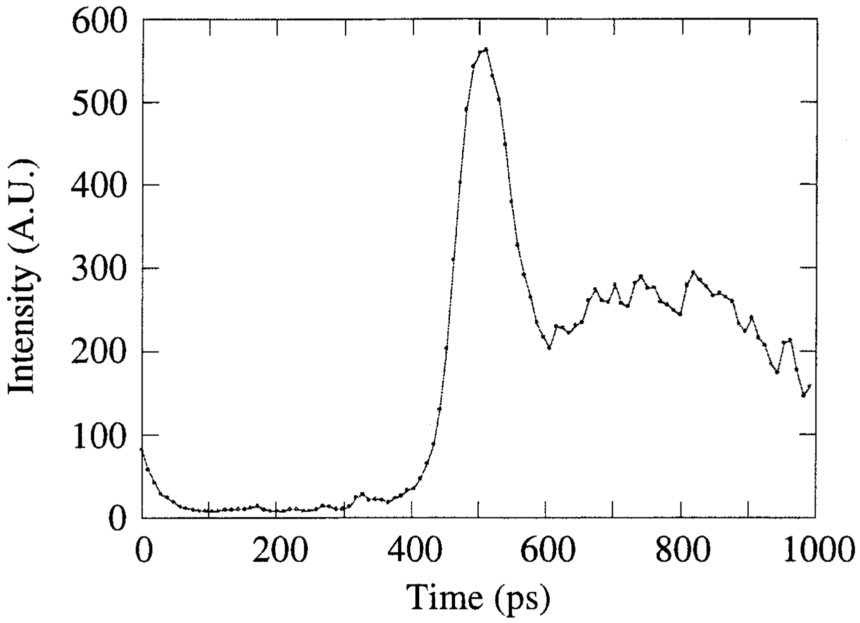

Figure 7.7: A streak camera trace showing the self pulsation in a consistent train of self pulsations for gain currents beyond that of the stably mode-locked regime.

opposed to -24 mA in the stably mode-locked case). The self-pulsed repetition rate of these lasers was about 400 MHz. Thus, the duty cycle was quite low.

When one applies larger currents, all lasers tested have also exited the regime of modelocking. They tend to begin self pulsation in this case also, but here the characteristics of the self pulsations are different. The frequency of the self pulsations is higher, close to or beyond a GHz (roughly agreeing with the trend mentioned in chapter 2). The pulses tend to have a larger width also. Both these factors tend to give pulses having a rather low duty cycle at the higher currents. Fig. 7.7 shows a typical self pulsation from a pulse train of about 0.95 GHz. This data was taken from a CPM

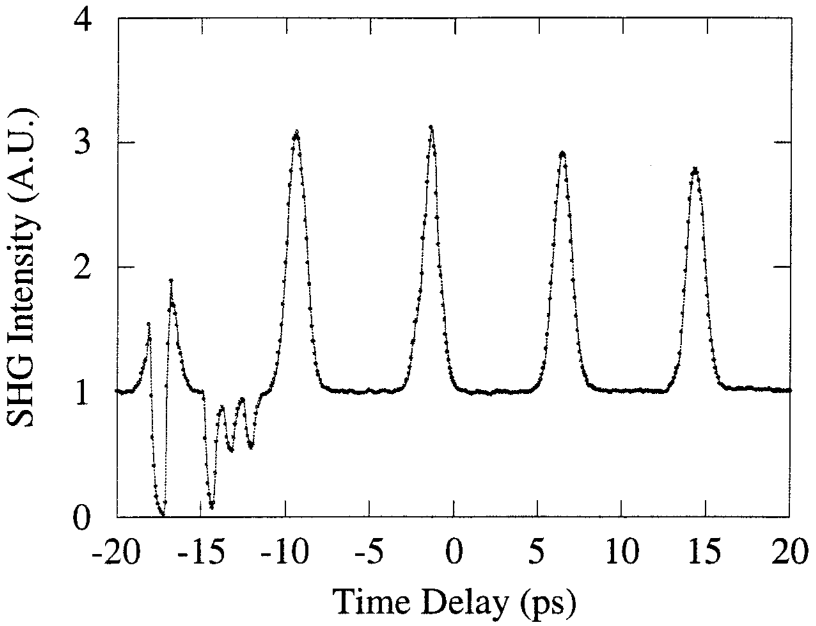

Figure 7.8: An autocorrelation of the 126 GHz CPM laser pulse train.

laser operating with a gain current of 119.2 mA and an absorber voltage and current of –1.6 V and –20.2 mA, respectively. A sharp peak followed by a broad rounded tail is a common, although yet unexplained, characteristic of many self-pulsing lasers.

More accurate pulse width estimates can be determined from autocorrelation measurements. The measured autocorrelation under conditions of 112 mA current into the gain contact and -0.84 V bias across the absorber section is shown in Fig. 7.8. The FWHM of the measured autocorrelation was 1.3 ps which, assuming a $sech^2$ pulse shape would give a 0.84 ps FWHM pulse. These are the shortest pulses we have produced directly within the laser, and correspond to a spatial length of 61 μm within the laser cavity. The absorber length is 50-80 μm (actual absorber contact 50 μm long) thus the pulse FWHM is essentially the same length spatially as the absorber section. Perhaps shorter pulses could be obtained by using a shorter absorber section as collision effects are more complete in a shorter absorber, but a corresponding drop in pulse energy would likely result.

7.2 Experimental results in regrown high-repetition-rate lasers

Similar measurements along with more in-depth measurements of the high-repetition-rate regrown lasers were taken. These measurements included the first chirp characterization of monolithic passively mode-locked semiconductor lasers and led to the first demonstration of direct chirp control in passively mode-locked lasers. Knowledge and control of the chirp parameters of semiconductor lasers is a prerequisite to obtaining transform-limited pulses and/or to compensate for group velocity dispersion in fiber. Here we report measurements of the sign and magnitude of chirp in high-repetition-rate mode-locked semiconductor lasers. The chirp of these monolithic lasers is measured in the frequency domain using filtering and cross-correlation techniques. For different injection currents, a range of different chirp values is measured, including strongly down-chirped pulses at higher injection currents and transform-limited pulses to slightly up-chirped pulses at lower injection currents. The pulse chirp and the resulting broadening are due to the algebraic addition of opposite-signed chirps from saturation of the absorption section and the gain section. These may cancel each other under some conditions leading to soliton-like transform-limited pulses.

Mode-locked semiconductor lasers have produced higher repetition rate pulses than all other types of lasers. Large material gain coefficients, fast recovery times, and the ability to make short monolithic cavities allow high-repetition-rate pulse trains (> 50 GHz) to be generated easily. Repetition rates of up to 240 GHz [9] in GaAs/AlGaAs and above 1.5 THz [10] in InGaAs/InGaAsP multisection structures have been reported. Although the carrier populations in both the gain and absorber sections are incapable of fully recovering during these < 20 ps periods, a sufficient modulation in each section is obtained to couple the modes [1]. The oscillation in the gain and absorber section populations are small enough to be accurately considered as linearized modulations which produce mode coupling [1,11]. As is known from studies in noise [12] or semiconductor laser amplifiers [13], changes in optical gain are accompanied by a material-generated phase shift due to amplitude-phase coupling characterized by the material parameter $\alpha = -\frac{d\chi_r}{dn}/\frac{d\chi_i}{dn}$.

Analysis shows that the phase modulation which results when a pulse saturates an absorbing medium has a sign opposite to that due to saturating a gain medium [14]. In general, the passively mode-locked semiconductor laser is not likely to be purely amplitude modulated. The accompanying phase modulation typically results in a nearly linear chirp on the pulses. To our knowledge, down-chirped pulses have never been obtained from electrically-pumped passively mode-locked semiconductor lasers [15]. It would be useful for one to develop a laser which can operate in all three dispersion regimes (i.e., down-chirped, chirp-free, and up-chirped) and to achieve control over its operation. In this section, we present experimental results from a regrown monolithic passively mode-locked laser. We find that both the magnitude and sign of chirp may be controlled. Dispersion is expected to result from SPM of both the saturable gain and absorption sections and from cavity dispersion. When using a relatively strong saturable absorber, opposite-signed contributions may cancel, causing a soliton-like pulse shaping to occur [16], creating a compensated net cavity dispersion. Chirp-free operation is obtained within the monolithic cavity, producing time-bandwidth-limited pulses without the need for any gratings or filters.

7.2.1 Experimental setup for monolithic chirp measurements

The two-section regrown monolithic GaAs/AlGaAs quadruple-quantum-well buried heterostructure laser is used in this experiment. The laser is 510 μm in length with a 390 μm long gain section, a 70 μm absorber section, and a 50 μm isolation region between sections. The threshold was 9.5 mA with the gain section pumped and absorber contact floating. All mode-locked measurements presented here were done with the absorber section grounded and the gain section driven by a DC current source. Both facets were coated for a reflection of 70%, and no additional feedback was added. Mode-locked measurements were obtained using light from the gain facet, however, results using the absorber facet were also measured with no noticeable difference, showing that the single pass effects from each section were relatively small.

The phase of the optical spectrum was measured as described previously [17,18] using a spatial filter in the Fourier plane of the dual-grating pulse compressor shown in Fig. 7.9. This filtered beam was temporally cross-correlated with an unfiltered, variable-delay beam from the same laser. The cross-correlation signal was obtained using a SHG setup and the relevant delay times versus filter center wavelengths were recorded to measure the mode-locked laser's chirp, $d\tau/d\omega$, as for the external cavity lasers in chapter 4. The sliding filter width was adjusted to pass 0.5 nm of the pulse train's optical spectrum.

7.2.2 Experimental results from monolithic chirp measurements

The laser was found to generate stable mode-locked pulse trains at 73 GHz with the absorber grounded over a range of gain currents from 18 mA to at least 40 mA. At the average power of 2.5 mW for a 30 mA gain current, the optical spectrum had 4 modes within its FWHM intensity as shown in Fig. 7.10. With the gratings placed at the focal points of the telescoped dual-grating pulse compressor, adding no additional chirp, the plot, Fig. 7.11, time delay of the filtered pulse versus filter center wavelength was obtained. The positive slope of the plot corresponds to a pulse in which the frequency decreases with time, i.e., a down-chirp. The magnitude of this down-chirp was found to be 1.7 ps/nm and appears essentially linear although the spectrum is not broad enough to allow one to convincingly rule out the presence of higher order chirp.

The same chirp measurement was also made by moving the second grating to

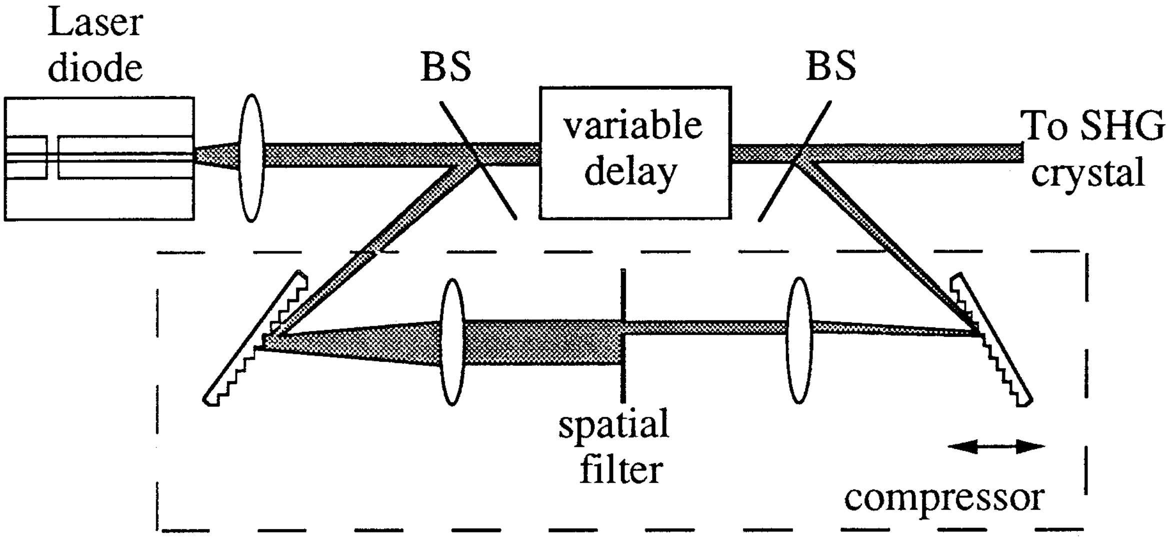

Figure 7.9: Two-section monolithic passively mode-locked laser in pulse measurement setup. The laser's back contact (left in the picture) is grounded to extract carriers from the saturable absorber section. The front contact is forward biased to inject carriers into the gain section. The laser is followed by a beam splitter. One of the beams is filtered and its pulse is cross-correlated with the original pulse to measure the time delay of its peak.

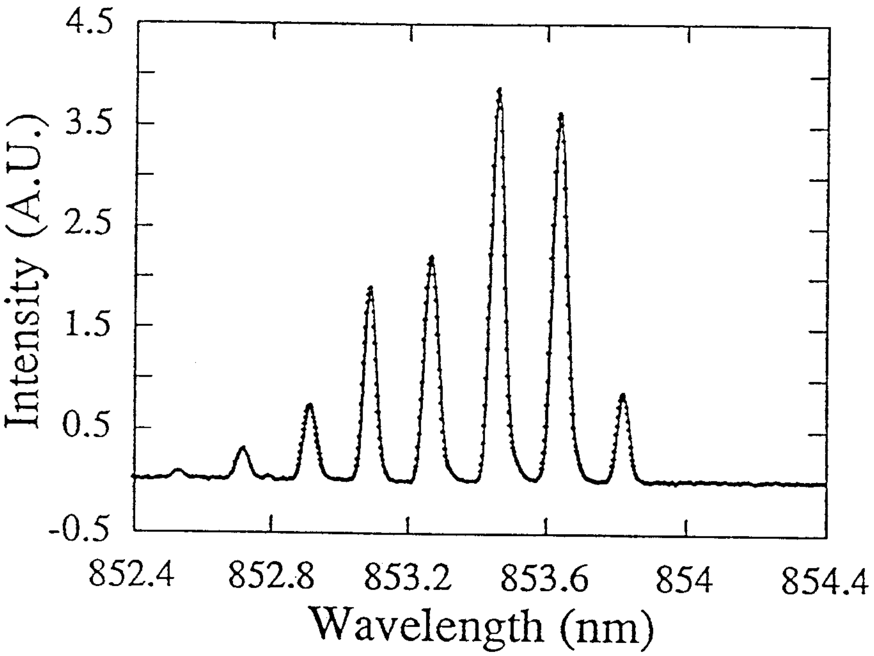

Figure 7.10: Optical spectrum of regrown two-section mode-locked laser with absorber section grounded and 30 mA into gain section.

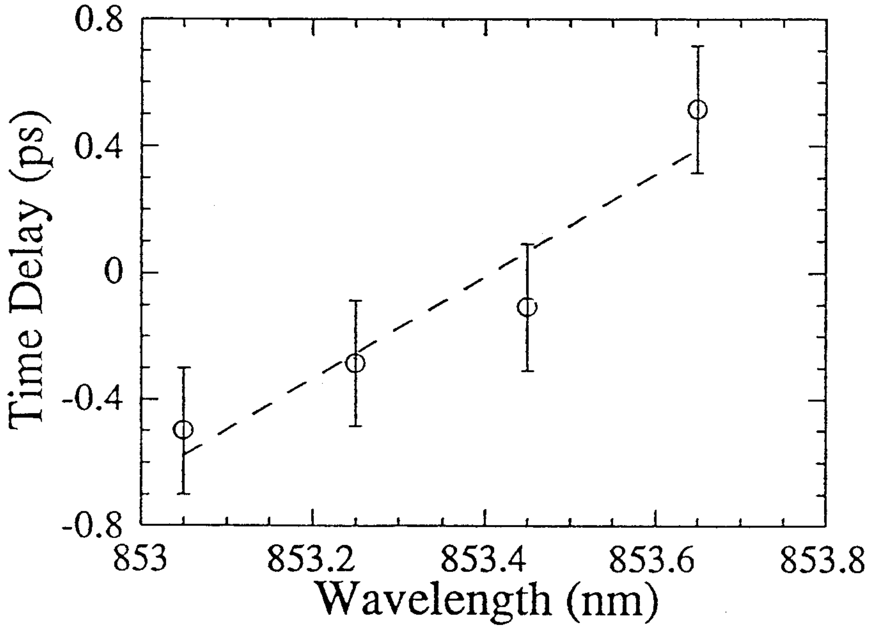

Figure 7.11: Chirp measured in frequency domain, displayed in terms of the time delay of the pulse's peak versus the center wavelength of a 0.5 nm rectangular spectral filter. The measurement is done with 30 mA into gain section and with absorber grounded. It shows an essentially linear down-chirp of 1.7 ps/nm.

a position where the net chirp was best eliminated (i.e., the time delay verses λ curve was made flat). This position for the second grating was found to be 5.8 cm inside the focal length for 2000 lines/mm gratings tilted with their normal 39.7° off the telescope's central axis, indicating a down-chirp of 1.62 ps/nm was produced by the monolithic mode-locked laser. These frequency domain chirp measurements are possible even though the measured pulses may have less than 10 fJ each. From these measurements, one would conclude that if the center mode's optical phase was taken to be 0, the phases of the modes on each side of this mode, progressively out from the center, would be 0.07, 0.28, and 0.62 rad, meaning that the standing waves for each of these modes would reach their peaks at earlier times corresponding to these optical phase shifts than the center mode would.

To verify these cross-correlation measurements, a set of standard autocorrelations was taken. Replacing the beams splitters in Fig. 7.9 with mirrors, the pulse width for a variety of positions of the telescoped compressor's second grating was measured. With all points plotted and fit with the expected function $\tau(1+ax^2)^{1/2}$, again the minimum chirp position is shown to be inside the focal length of the second lens by about 5.8 cm. The curve, confirming the measured down-chirp, is shown in Fig. 7.12. The down-chirp depends on the injection current. As the relative strength of the absorber and gain sections is changed, the relative amount of phase modulation from both the gain and absorber is expected to change, causing a different net chirp. In fact, the down-chirp was found to increase at larger injection currents. The results of the chirp measurement for injection currents of 18 mA, 20 mA, 30 mA, and 40 mA into the

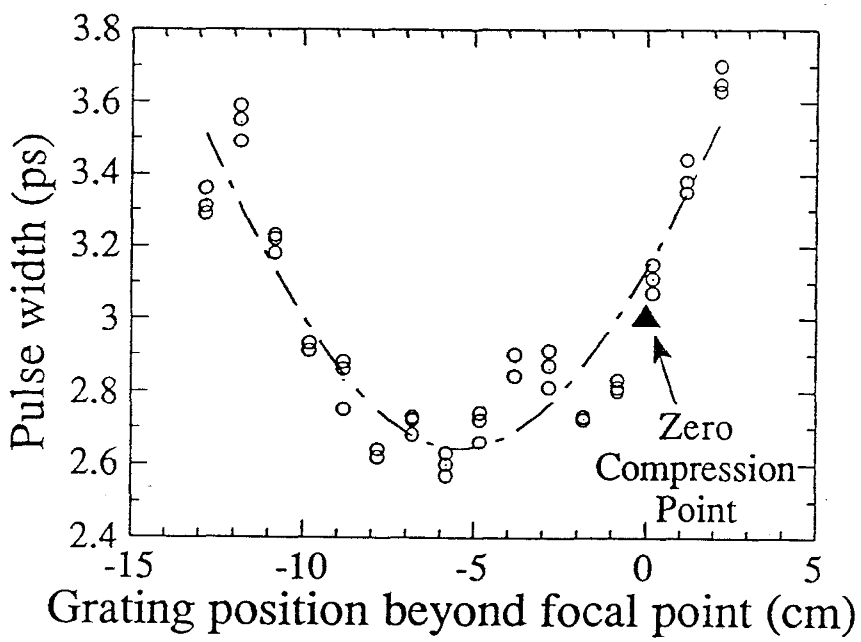

Figure 7.12: Pulse width versus position of second grating in dual-grating compressor is shown. A position of zero indicates the grating is at the focal point and no chirp is added. Negative positions indicate the grating is closer than the focal point of the second lens. A minimum pulse width occurs near -5.8 cm corresponding to a 1.62 ps/nm down-chirp from the laser.

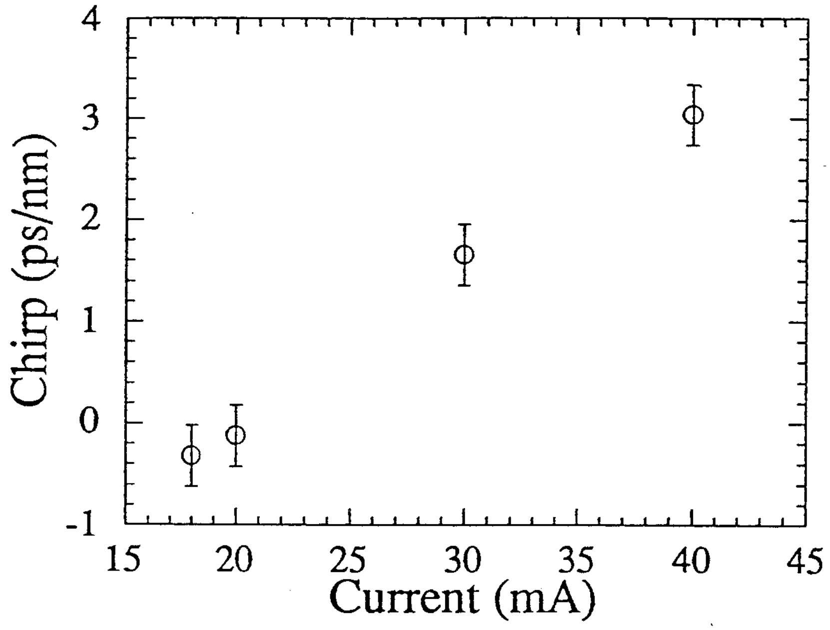

Figure 7.13: Measured values of chirp as a function of gain section current. An increasing down-chirp is seen as the gain current is increased.

gain section are shown in Fig. 7.13. The CPM effect which has been observed in dye lasers and suggested [5] and studied [19] in semiconductor lasers was not noticeable here. Two possible reasons for the absence of a transient grating are noted. The effectiveness of transient grating build-up is expected to be proportional to both the peak intensity and the diffusion time constant. This product is rather small for peak cavity intensities around 5 MW/cm^2 (about 1/100 of that from external cavity lasers) and a relatively short diffusion time. The ambipolar diffusion constant, $D^* = 15\ cm^2/sec$, for GaAs, results in a carrier diffusion time [20] of $t_d \approx L^2/16D^* = 0.6$ ps for a grating to smear out to a full width of $L = \lambda/2n$, where $n = 3.6$ is the material's index of refraction. This implies that the transient grating decays in a time shorter than the pulse width. Saturation effects, however, are a cumulative result from a number of pulses since the repetition rate is faster than the recovery time of either section. Thus, for high-repetition-rate lasers, the grating is expected to be blurred even while the saturation effects are significant. Secondly, the 70% reflection provides incomplete standing wave interference for building the saturation grating. Nevertheless, without significant saturation grating effects, chirp-free pulses were obtained at the lower injection currents.

7.3 Discussion of monolithic results

Experimental measurements of the spectrum, pulse chirp, and the variation of pulse chirp with injection current have just been reviewed. They show qualitatively the same characteristics as the calculation for 80 GHz in the previous chapter. A broader spectrum and larger pulses as found from streak camera results can typically be obtained at higher bias conditions. An optical spectrum for the laser operating at 30 mA had been shown in Fig. 7.10. The chirp of this spectrum has been measured through cross-correlation techniques [21], and integration of these results leads to phase values, $\phi(\lambda)$, of the optical spectrum plotted in Fig. 7.14. The figure is derived from an integration over Fig. 7.11 and shows a phase of the optical spectrum corresponding to a train of pulses with a 1.7 ps/nm down-chirp and a time-bandwidth product, $\Delta\tau_w\Delta\nu$, which is 19% larger than the compressed pulse time-bandwidth product achieved in

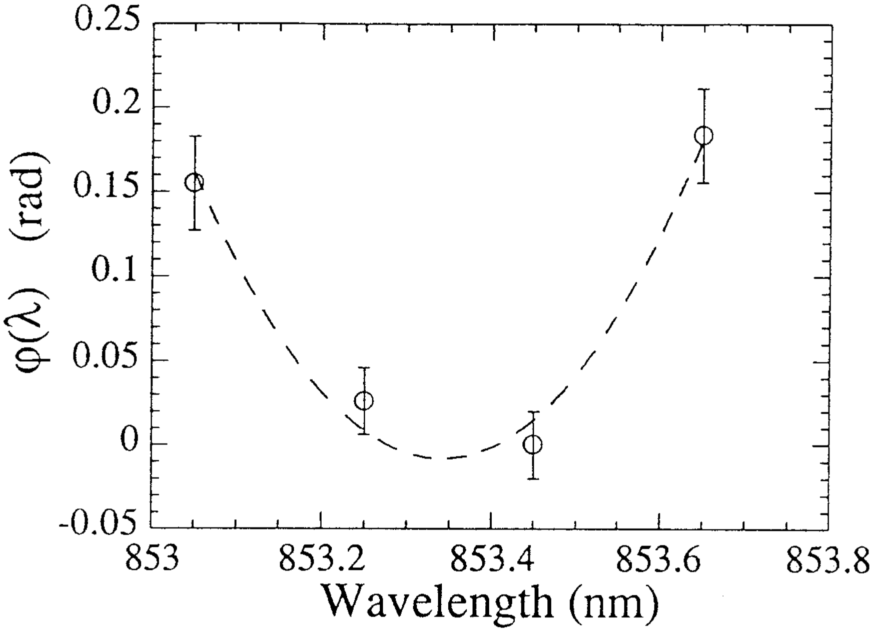

Figure 7.14: Chirp measured in frequency domain, displayed in terms of the phase of optical spectrum vs. the center wavelength of a 0.5 nm rectangular spectral filter. The measurement is done with 30 mA into gain section and with absorber grounded and shows an essentially linear down-chirp of 1.7 ps/nm.

the experiment. This regime of operation qualitatively corresponds to the calculated optical phase from chapter 6. Additionally, the experimental measurement of 1.7 ps/nm down-chirp for this laser is equivalent to $(\phi_1 + \phi_{-1} - 2\phi_0)/2 = 0.07$ rad, just as in Fig. 6.15. Furthermore, experimental results have demonstrated the effect of changes in the DC gain section injection current from the preceding case. The experimental results are shown in Fig. 7.13. While the laser is above threshold, the changes in DC injection current are nearly linearly related to the average photon intensity inside the cavity, $\tilde{s}_0$. Hence, we expect Fig. 7.13 to show agreement with the calculated pulse chirp in Fig. 6.17. Both show a sequence of up-chirped, chirp-free, and down-chirped operation as the photon intensity inside the cavity is increased. Not only is the magnitude of chirp in agreement at the point of $\tilde{s}_0 = 2.5$, but it remains in close agreement over the full experimentally measured range of pumping strengths. This is the first time amplitude-to-phase coupling has been able to explain the chirp in passively mode-locked lasers.

The theoretical model seems to provide an excellent indication of which parameter values will satisfy the necessary conditions for modelocking. Theoretical results for the CPM laser modelocked near 126 GHz have shown very good agreement with measurement also, and indicate that a larger ratio of absorber differential gain (or other parameter adjustments following the same trends) is required to satisfy the coupled mode equations at this repetition rate. Reasonable parameter values have not been able to satisfy the coupled mode equations for rates of over 500 GHz in any theoretical work on passive modelocking to date, since for lasers at these rates the minimum threshold solution has always been found (theoretically) to be the single-mode solution. Suspicions lead one to suspect that the amplitude-to-phase coupling could be responsible for introducing instabilities at the round-trip frequency and causing fluctuations to de-stabilize the single mode operation, however, no result demanding this has been derived yet.

Although good agreement between theory and experiment is obtained, we do not intend to imply that we have found the actual parameters of the mode-locked laser. However, we believe that the chosen parameters place the calculations in qualitatively the same regime of operation and that the calculated effects of the α parameter, the laser structure parameters, and the bias parameters will show a good correspondence with future experimental results.

Additionally, all results presented in this thesis are believed to be for the lowest-order supermode – the one which possesses a minimum threshold gain. We have found some relatively small regions in the parameter space in which a second supermode solution could be found as a self-consistent solution. For a set of reasonable parameters and an arbitrary $\tilde{s}_0$, the second supermode was always found to exist for a slightly different repetition rate detuning, δ, and a higher required gain, $\tilde{g}_0$. The supermode solutions were not orthogonal. This is contrary to some assumptions in a recent publication on passively mode-locked laser noise [23]. One would expect actively mode-locked supermode solutions to be orthogonal. However, passively mode-locked lasers are inherently nonlinear, i.e., mode coupling is a direct consequence of the saturation effects resulting from the beating of the Fabry-Perot laser modes. Only in a linear coupled mode problem would one expect the eigenvectors to be orthogonal. In passive modelocking, however, the presence of one supermode will modify the system (the laser) such that conditions will not permit a second supermode to exist simultaneously. Thus a superposition of supermodes is not a valid solution to the set of coupled nonlinear equations. The characteristic shape of the second supermode we have found has essentially the same shape for its supermode envelope but was offset by half of one mode spacing from the usual spectrum center. Two of the lasing modes in its supermode thus possessed nearly equal field strengths, the nearly quadratic phase was essentially centered about this offset point and the necessary gain was always found to be higher than that required for the supermode which was not offset.

7.4 Conclusion for high-repetition-rate lasers

In conclusion, a steady-state analysis for high-repetition-rate passively mode-locked semiconductor lasers was presented (chapter 6). We derived an equation for an arbitrary mode that exists in the supermode of the laser. The equation requires gain to balance loss and incorporates phase effects that result from amplitude-to-phase coupling in each section of the laser. Additionally, mode coupling enters through the nonlinearity of both the saturable gain and saturable absorption sections. A nonlinear eigenvalue problem approach was presented to numerically solve for the passively mode-locked laser's supermode. An approximation of nearest-neighbor-only coupling was used here. Next, an approximate 3-mode solution was analytically solved for the purpose of building intuition and theoretically explaining recent experimental results which show the possibility of obtaining up-chirped, chirp-free and down-chirped pulses all from a single laser under different gain section bias. Results of the full supermode calculation (with nearest-neighbor-only coupling) were presented. The supermode magnitude and phase were plotted in the case where no amplitude-to-phase coupling exists in either laser section. In this case, supermode solutions could be obtained over a broad range of cavity intensities. Other characteristics of the supermode solution were plotted as a function of cavity intensity also.

When reasonable amplitude-to-phase coupling factors were chosen for both laser sections, the supermode symmetry was severely changed. The phase was found to take on a predominantly quadratic shape in the region of the spectrum where the mode strengths are significant. This indicated the presence of essentially linearly chirped pulses. The presence of a non-zero α parameter was found to drastically limit the range (in terms the variation of cavity intensity) over which stable mode-locked solutions could be found owing to the added phase effects. The effect of the α parameters on the reduction in gain due to coupling were neither very advantageous nor very harmful. They typically led to a slight weakening in $Re(R)$, the reduction in threshold gain due to mode coupling. To facilitate understanding and optimization of high-repetition-rate passively mode-locked lasers, calculations of the reduction in gain provided through mode coupling and of the expected linear chirp were presented for variations in parameters of the laser structure and bias.

Finally, experimental results from a high-repetition-rate passively mode-locked laser at 73 GHz were compared to the supermode calculations in this paper. A good qualitative agreement for the spectral shape, chirp, and variation in chirp with changing injection current was found. Identical to the theoretical calculations, stable pulse trains of slightly up-chirped, chirp-free, and relatively strongly down-chirped pulses were obtained from high-repetition-rate passively mode-locked lasers. The sequence of different regimes of operation was obtained in the same order as pumping was increased experimentally and in the the model. Both gave similar magnitudes of chirp also. The changing SPM effects are attributed to a change in the ratio of absorber to gain section strengths. At strong pumping, strongly down-chirped pulses are demonstrated both theoretically and experimentally from these relatively-long-absorber-section lasers. These pulses would undergo compression in fiber propagation at this wavelength. The calculated supermodes analyzed were typically not as broad as the measured supermode. The reason for choosing rather narrow supermodes in the theoretical supermode analysis is that in this case the higher-order coupling effects (e.g. second nearest neighbor, third nearest neighbor coupling, etc.) are expected to be smaller. Thus, in this case, the nearest-neighbor-coupling approximation is expected to be more accurate. However, by including second-nearest-neighbor coupling and higher-order coupling in the matrix for the supermode solution, one may more accurately model lower repetition rate mode-locked lasers at repetition rates (≈ 5 GHz) which are viable for data rates in communication systems which are practical today.

References

[1] J. Paslaski and K. Y. Lau, *Appl. Phys. Lett.*, **59**, 7 (1991).

[2] K. Y. Lau and J. Paslaski, *IEEE Photon. Technol. Lett.*, **3**, 974 (1991).

[3] R. L. Fork and C. V. Shank, *Appl. Phys. Lett.*, **38**, 671 (1981).

[4] M. S. Stix and E. P. Ippen, *IEEE J. Quantum Electron.*, **19**, 520 (1983).

[5] Y. K. Chen and M. C. Wu, *IEEE J. Quantum Electron.*, **28**, 2176 (1992).

[6] R. L. Fork, C. H. B. Cruz, P. C. Becker, and C. V. Shank, *Opt. Lett.*, **12**, 483 (1987).

[7] P. P. Vasil'ev and A. B. Sergeev, *Electron. Lett.*, **25**, 1049 (1989).

[8] S. Sanders, L. Eng, J. Paslaski, and A. Yariv, *Appl. Phys. Lett.*, **56**, 310 (1990).

[9] J. F. Martins-Filho and C. N. Ironside, *Appl. Phys. Lett.*, **65**, 1894 (1994).

[10] S. Arahira, S. Oshiba, Y. Matsui, T. Kunii, and Y. Ogawa, *Optics Lett.*, **19**, 834 (1994).

[11] R. A. Salvatore, S. Sanders, T. Schrans, and A. Yariv, "Supermodes of high-repetition-rate passively mode-locked semiconductor lasers," submitted to *IEEE J. Quantum Electron.*

[12] K. Vahala and A. Yariv, *IEEE J. Quantum Electron.*, **19**, 1096 (1983).

[13] M. Y. Hong, Y. H. Chang, A. Dienes, J. P. Heritage, and P. J. Delfyett, *IEEE J. Quantum Electron.*, **30**, 1122 (1994).

[14] G. P. Agrawal and N. A. Olsson, *IEEE J. Quantum Electron.*, **25**, 2297 (1989).

[15] A. Azouz, N. Stelmakh, and J.-M. Lourtioz, *Electron. Lett.*, **29**, 1437 (1993).

[16] O. E. Martinez, R. L. Fork, and J. P. Gordon, *J. Opt. Soc. Am. B*, **2**, 753 (1985).

[17] J. L. A. Chilla, and O. E. Martinez, *IEEE J. Quantum Electron.*, **27**, 1228 (1991).

[18] R. A. Salvatore, T. Schrans, and A. Yariv, *Optics Lett.*, **20**, 737 (1995).

[19] D. J. Derickson, R. J. Helkey, A. Mar, J. R. Karin, J. G. Wasserbauer, and J. E. Bowers, *IEEE J. Quantum Electron.*, **28**, 2186 (1992).

[20] C. M. Wolfe, N. Holonyak, and G. E. Stillman, **Physical Properties of Semiconductors**, Prentice Hall, Englewood Cliffs, NJ (1989).

[21] R. A. Salvatore and A. Yariv, "Demonstration of down-chirped and chirp-free pulses from high-repetition-rate passively mode-locked lasers," accepted for publication in *IEEE Photon. Tech. Lett.*, Oct. 1995.

[22] S. Sanders, *Ph.D. Thesis*, California Institute of Technology (1991).

[23] I. Kim and K. Y. Lau, *IEEE J. Quantum Electron.*, **29**, 1081 (1993).